UNIVERSITEIT ANTWERPEN

FACULTEIT WETENSCHAPPEN

PB TMD Analysis of the Intrinsic-k_T Parameter q_s from DY p_T Data at Varying Energies

AUTEUR:
TIAS JANSSENS

PROMOTOR:
PROF. DR. FRANCESCO HAUTMANN

CO-PROMOTOR:
DR. ALEKSANDRA LELEK

Thesis ingediend ter verkrijging van
de graad "master in de fysica".

DEPARTEMENT FYSICA
ELEMENTAIRE-DEELTJESFYSICA

AUGUSTUS, 2024

Universiteit Antwerpen
Faculteit Wetenschappen

ACADEMIEJAAR 2023-2024

Abstract

The Drell-Yan (DY) process is crucial in high-energy physics, particularly for precision electroweak measurements and the study of Quantum Chromodynamics (QCD). It provides a clear production channel where quarks and antiquarks from colliding hadrons annihilate, forming a virtual photon or Z boson that decays into leptons. This process is instrumental in refining parton distribution functions (PDFs), which describe the momentum distribution of quarks within hadrons, and for probing parton dynamics at varying energy scales. Moreover, the DY process allows for the study of soft gluon emissions and particle evolution, offering insights into the behaviour of quarks and gluons under QCD. The Parton Branching (PB) framework, incorporating transverse momentum-dependent (TMD) PDFs, is used to model the evolution of these distributions, distinguishing between different types of parton branchings based on a soft gluon resolution scale (z_M) which is parametrised by q_0. These TMDs are first fitted on Deep Inelastic Scattering (DIS) data and are then matched with Next-to-Leading Order (NLO) matrix elements, created by a Monte Carlo generator, to create predictions of DY transverse momentum (p_T) distributions.

A key focus of this research is the interplay between the intrinsic transverse momentum (k_T) distribution, characterised by the parameter q_s, and the resolution scale z_M. A long-standing issue is the mismatch between PDFs, which are evolved without a z_M, and the parton shower evolution that include z_M. This thesis presents the first analysis of DY p_T distributions using the PB TMD method with a dynamical z_M. The behaviour of the intrinsic k_T distribution parameter q_s is studied across a range of centre-of-mass (COM) energies (62 GeV – 13 TeV) using data from the experiments CMS, ATLAS, CDF, D0, Phenix, and R209. The analysis showed a consistent fit for most datasets, except for some discrepancies and limited data. The key finding is that the parameter q_s remains independent of COM energy, contrary to previous studies that suggested q_s would depend on COM energy when using a dynamical treatment of soft gluons. This research found no such dependence, which either suggests that this result is a bridge between a fixed and a dynamical z_M, meaning that a fixed z_M can be seen as the limit of a dynamical z_M for small q_0, or it challenges earlier results by being the first instance of an approach using dynamical z_M to not show COM dependence for the parameter q_s.

This work showcases that it is possible to examine the behaviour of the intrinsic k_T parameter q_s with the PB TMD method using a dynamical resolution scale. This enhances our understanding of the intrinsic transverse momentum distribution but also underscores the importance of considering the resolution scale in such analyses. Additionally, this study proposes further investigations into the behaviour of the q_s parameter and its COM energy dependence, as this behaviour is not fully understood. Specifically, understanding the influence of the treatment of the strong coupling is necessary for understanding this new behaviour. Furthermore, current TMDs are assumed flavour-independent, future studies could take flavour into account.

Samenvatting (Dutch)

De persoonlijke motivatie om dit onderzoek te starten komt voort uit een diepe fascinatie voor de deeltjesfysica. Het laat op het meest fundamentele niveau zien hoe het universum werkt en hoe het leven ervan afhangt. Dit biedt de mogelijkheid om na te denken over de werkelijkheid waarin we leven en om diepgaande filosofische inzichten te verwerven. Daarom wil ik een uitgebreide kennis verwerven over de huidige stand van zaken van deze theorieën, en het onderwerp van deze scriptie was een perfecte aanleiding om een van de vier fundamentele krachten, de sterke interactie, te bestuderen. De theorie die deze interactie het beste beschrijft, wordt kwantumchromodynamica (QCD) genoemd. Dit is een kwantumveldentheorie gebaseerd op een niet-abelse Lie-groep. Het werkt bijzonder goed in hoog-energetische gebieden, waar de koppelingsconstante klein is vanwege de zogenaamde "running coupling" van QCD. Deze theorie wordt grondig uitgelegd in Hoofdstuk 2, het is grotendeels een samenvatting van de cursus die ik volgde over kwantumchromodynamica, gegeven door mijn begeleider Prof. Dr. Francesco Hautmann aan de Universiteit van Antwerpen. Daarom is het eerste hoofdstuk sterk geïnspireerd door de cursusnotities gemaakt door Thomas Van Laer. Het hoofdstuk legt de theoretische basis voor het begrijpen van proton-proton botsingen. Het hoofdstuk behandelt het eikprincipe, waarbij de nadruk ligt op het belang ervan voor het waarborgen van lokale eik-invariantie, en introduceert de QCD Lagrangiaan om de dynamica van quarks en gluonen te beschrijven. De kwantisering van eik-veldtheorieën wordt onderzocht, waarbij de verschillen tussen Abelse en niet-Abelse gevallen worden belicht. Belangrijke concepten zoals renormalisatie, de renormalisatiegroep en het lopen van de koppelingsconstante worden besproken, waarbij wordt geïllustreerd hoe de sterke interactie zich anders gedraagt op verschillende energieniveaus. Het hoofdstuk behandelt ook verstrooiingsprocessen, factorisatie, evolutievergelijkingen en het Drell-Yan (DY) proces, die allemaal cruciaal zijn voor het analyseren van hadronbotsingen en het begrijpen van de intrinsieke transversale impulsverdelingen van partonen binnen hadronen. Deze kennis is essentieel voor de focus van de thesis op het DY process. Het DY proces is van cruciaal belang in de hoge-energie fysica voor precisie metingen in de elektrozwakke sector en de studie van QCD. Het biedt een helder productiekanaal waarbij quarks en antiquarks van botsende hadronen annihileren en een virtueel foton of Z boson vormen dat vervalt in leptonen. Dit proces is essentieel voor het verfijnen van parton distributiefuncties (PDFs), die de momentumsverdeling van quarks binnen hadronen beschrijven, en voor het onderzoeken van parton dynamica bij verschillende energieniveaus. Bovendien stelt het DY-proces ons in staat om *soft gluon*-emissies en de evolutie van deeltjes te bestuderen, wat inzichten biedt in het gedrag van quarks en gluons onder QCD.

Het DY process kan worden onderzocht met behulp van de Parton Branching (PB) methode, deze methode wordt uitgelegd in Hoofdstuk 3. Het herformuleert de evolutievergelijkingen, geïntroduceerd in Hoofdstuk 2, met een unitariteitsbenadering. Hierbij wordt een onderscheid gemaakt tussen oplosbare en niet-oplosbare partonvertakkingen op basis van een zachte gluon-resolutieschaal (z_M), en Sudakov-vormfactoren worden gebruikt om de kans te modelleren dat er tussen energie-schalen geen vertakkingsgebeurtenissen plaatsvinden. De PB-methode wordt numeriek geïmplementeerd via iteratieve Monte Carlo-technieken, waardoor de evolutie van partonverdelingen binnen hadronen van lagere naar hogere energieniveaus mogelijk wordt. Een belangrijk aspect van dit hoofdstuk is de uitbreiding van de methode om *Transverse Momentum Dependent* distributies (TMDs) te omvatten, door een kinematische toewijzing (*angular ordering*) die de evolutieschaal verbindt met de transversale impuls van een uitgezonden parton. Deze TMDs zijn cruciaal voor een nauwkeurige beschrijving van processen zoals Drell-Yan-productie en voor het begrijpen van partondynamica. Bovendien introduceert het hoofdstuk ook de gefactoriseerde vorm van de TMD; het collineaire deel samen met een intrinsieke transversale momentumverdeling (k_T). Het hoofdstuk eindigt met de bespreking van de dynamische resolutie-schaal z_M, dit is een nieuwe aanpak voor het onderscheid tussen oplosbare en niet-oplosbare partonvertakking, gebaseerd op de angular ordering die geïntroduceerd is voor de transversale impulsen mee in rekening te houden binnen de PB methode. Deze uitgebreide benadering zorgt ervoor dat de complexiteit van TMDs effectief wordt beheerd binnen de PB methode.

In Hoofdstuk 4 wordt uitgelegd hoe de PB aanpak wordt toegepast op het Drell-Yan process. Het begint met het uitleggen van de procedure voor het verkrijgen van de initiële collineaire PDF voor de TMD in de intrinsieke transversale momentumverdeling. De PDF wordt gefit op diepe inelastische verstrooiings data van HERA, deze vormt dan samen met de k_T-distributie de TMD. Vervolgens wordt het gebruik van de PB TMD-methode voor botsingsvoorspellingen in detail besproken; er wordt uitgelegd hoe PB TMDs worden gecombineerd met Next-to-Leading Order (NLO) matrixelementen met behulp van de Cascade-generator om voorspellingen te doen over inclusieve DY transversale momentum (p_T) distributies. Deze benadering verhoogt de nauwkeurigheid van botsingsvoorspellingen door PB TMDs te integreren met standaard collineaire matrixelementgenerators. Daarnaast biedt het hoofdstuk een overzicht van belangrijke resultaten van vorige studies met betrekking tot de toepassing van de PB methode op inclusieve DY p_T data. Belangrijke bevindingen omvatten de effectiviteit van de methode in het beschrijven van DY transversale impulspectra over verschillende kinematische gebieden en energieniveaus. Het schetst een duidelijk beeld van de beschrijving die de PB TMD-methode kan bieden voor DY doorsnedes. Al de resultaten die worden aangehaald voor de effectiviteit aan te tonen maakten gebruik van een vaste resolutieschaal.

Het onderzoek van deze scriptie in Hoofdstuk 5 maakt gebruikt van dezelfde methode, maar het gebruikt de dynamische resolutieschaal van Hoofdstuk 3. Dit wordt voor het eerst gedaan in dit onderzoek omdat het gebruik van de dynamische resolutieschaal belangrijk is voor het begrijpen van de fysica van QCD coherentie en de *angular ordering* van gluonradiatie. Een ander belangrijk aandachtspunt van dit onderzoek is de wisselwerking tussen de intrinsieke transversale momentum (k_T) distributie, gekenmerkt door de parameter q_s, en de resolutieschaal z_M. Een lang bestaand probleem is de mismatch tussen PDFs, geëvolueerd zonder de resolutieschaal z_M, en de parton shower evolutie die wel de resolutieschaal z_M bevat. Deze scriptie presenteert de eerste analyse van DY p_T-distributies met behulp van de PB TMD-methode met een dynamische resolutieschaal z_M. Het gedrag van de intrinsieke transversale momentumdistributieparameter q_s wordt bestudeerd over een reeks van *centre-of-mass* (COM) energieën (62 GeV – 13 TeV) met behulp van data van de experimenten CMS, ATLAS, CDF, D0, Phenix en R209.

De volledige analyse wordt uitgebreid besproken in Hoofdstuk 5. Het toont aan dat, binnen de onzekerheden, de parameter q_s onafhankelijk is van de COM-energie. Dit toont een nieuw resultaat in de energieafhankelijkheid van q_s, wat verder onderzoek rechtvaardigt. Opmerkelijk is dat een vorige studie, met een vaste, niet-dynamische z_M, een bijna vlakke q_s-gedragslijn met energie vond uit fits op DY p_T-data. Daarentegen meldde andere studies met een dynamische aanpak een andere trend, namelijk een COM-afhankelijkheid van de parameter q_s. Deze thesis toont echter dat wanneer gewerkt wordt met een dynamische z_M die een kleine transversale impuls-schaal van $q_0 = 0.5$ GeV gebruikt, het gedrag van q_s met energie afvlakt, wat dichter aansluit bij de bevindingen van de studie met de vaste z_M. Het resultaat van deze thesis lijkt de eerste instantie te zijn waarbij een dynamische z_M-benadering, vergeleken met DY-gegevens, resulteert in een bijna vlakke q_s, wat de eerdere resultaten gerapporteerd in de studies met dynamische z_M uitdaagt. Daarnaast is het belangrijk om deze bevindingen te vergelijken met de vaste z_M-berekening en de minimum transversale impuls-schaal die in deze thesis wordt gebruikt te vergelijken met die in eerdere dynamische z_M-berekeningen. In de studies met dynamische z_M werd gerapporteerd dat de helling afnam met afnemende q_0. Dit zou kunnen suggereren dat het resultaat van deze studie de brug vormt tussen de twee situaties; het scenario met een vaste z_M kan worden gezien als de limiet van een dynamische z_M met een zeer kleine q_0—wat aanzienlijk meer zachte emissies toelaat dan berekeningen met q_0-waarden van 1 GeV of hoger.

Hoewel het onderzoek waardevolle inzichten heeft opgeleverd, is het essentieel om bepaalde beperkingen te erkennen. De belangrijkste beperking van deze studie is de onvolledige en beperkte data van bepaalde experimenten. Met name leverden de datapunten van de CDF- en D0-experimenten bij 1960 GeV geen bruikbare resultaten op. Respectievelijk, de systematische afwijkingen en het beperkte aantal datapunten beïnvloedden de robuustheid van de analyse. Dit benadrukt de noodzaak voor meer uitgebreide datasets om de bevindingen te valideren over alle energieschalen en experimentele opstellingen. Verdere onderzoeken zouden zich kunnen richten op het toepassen van de PB TMD-methodologie op experimentele gegevens in de 1960 GeV-regio, om de toepasbaarheid ervan te valideren.

Ter conclusie, dit werk toont aan dat het mogelijk is om het gedrag van de intrinsieke k_T-parameter q_s te onderzoeken met de PB TMD-methode met een dynamische resolutieschaal. Dit verbetert niet alleen ons begrip van de intrinsieke transversale momentumdistributie, maar onderstreept ook het belang van het overwegen van de resolutieschaal in dergelijke analyses. Bovendien stelt deze studie voor om verder onderzoek te doen naar het gedrag van de q_s-parameter en de afhankelijkheid daarvan van de COM-energie, aangezien dit gedrag nog niet volledig begrepen is.

Contents

Chapter 1

Introduction

The personal motivation of starting this research, comes from a deep fascination with elementary particle physics, it shows at the most fundamental level how the universe works and how life depends on it. This gives opportunity to think about the reality in which we live, and gain profound philosophical insights. Therefore, I wanted to gain an extensive understanding of the current knowledge of these theories, and the topic of this thesis was a perfect reason to study one of the four fundamental forces, the strong interaction. The theory that describes this interaction the best is called quantum chromodynamics (QCD), it is a quantum gauge field theory based on a nonabelian Lie group. It works particularly well in high energy regions, where the coupling is small due to the running coupling of QCD. This theory is thoroughly[1] explained in Chapter 2, starting from basic principles and going to advanced topics such as the factorisation of dynamics to describe hadron collisions. This chapter is mostly a summary of the course I took on quantum chromodynamics, taught by my supervisor Prof. Dr. Francesco Hautmann at the University of Antwerp. Therefore, the first chapter is heavily inspired by the lecture notes of this course taken by Thomas Van Laer [1].

The measurement of the vector boson transverse momentum (p_T) in Drell-Yan (DY) production [2] in proton-proton (pp) collisions provides a detailed investigation into various aspects of the strong interaction sector of the Standard Model, significantly impacting precision electroweak measurements. Higher-order perturbative QCD calculations are required for a precise description of DY production in pp collisions at the LHC (e.g. [3]). However, the very low p_T region of the DY cross section of Z-bosons ($p_T < \mathcal{O}(m_Z)$) is sensitive to the nonperturbative transverse motion of partons within hadrons and cannot be described by fixed-order calculations. Soft gluon resummation to all orders (e.g. [4]) is required. The precise description of the Z/γ boson has been explored since the 1980s through various analytical transverse momentum dependent (TMD) resummation methods (e.g. Collins-Soper-Sterman [5]) or in parton showers of multi-purpose Monte Carlo (MC) event generators, such as PYTHIA8 [6] and HERWIG7 [7], matched with higher-order matrix elements [8–10]. These had varying success. In this thesis, the parton branching (PB) TMD methodology in momentum space, introduced in [11, 12], is employed. This PB TMD method is thoroughly explained in Chapter 3. Chapter 4 explains how this method is applied to DY data, and it briefly summarises the results of previous studies.

Chapter 5 of this thesis delves into the behaviour of the intrinsic k_T parameter q_s in the

---

[1] In the context of this thesis, of course. There are lots of topics that are not discussed, as they would require entire books and that would be outside the scope of the research.

TMD distribution, examining its behaviour across different centre-of-mass (COM) energies, $\sqrt{s}$, of various experiments. The analysis is focused on the small-p_T region for a wide range of COM energies. Despite being initially fitted only on deep-inelastic scattering (DIS) data from HERA experiments, the PB-TMD methodology has demonstrated its capability to describe DY p_T spectra at both LHC [13] and lower energies [14] without parameter adjustment. This approach simultaneously considers soft gluon radiations and the transverse momentum recoils in the parton branchings along the QCD cascade, effectively addressing the multiple-scale problem [15] of the DY transverse momentum for $p_T \ll m_{DY}$. This confirms the universality of the TMDs in the PB TMD method, as they can describe both DIS and DY cross sections at all available center-of-mass energies.

This research aims to deepen the understanding of the intrinsic transverse momentum distributions and the question of their possible universal behaviour across different experimental conditions. This work not only provides insights into the strong interaction but also contributes to the broader field of high-energy particle physics by refining the theoretical tools needed for precise predictions in particle collisions.

Chapter 2

Basic Elements of Quantum Chromodynamics

To start the theoretical introduction of the thesis, it is valuable to first give a historical overview [16] of the evolution of Quantum Chromodynamics (QCD). It is the theory that explicates the strong force—one of nature's four cardinal forces[1]—it traces its roots back to the 1960s and 1970s. This period marked a scientific endeavour to unravel the mysteries of the strong force, which paradoxically binds protons within an atomic nucleus despite their similar positive charges that should cause mutual repulsion due to electromagnetic forces. The advancement of particle accelerators during this era led to the discovery of a plethora of subatomic particles, underscoring the need for a more fundamental theory.

A breakthrough was achieved in 1964 with Murray Gell-Mann and George Zweig's proposal of quarks as the elementary building blocks of hadrons (including protons and other particles), giving rise to the quark model. This model categorised hadrons based on their quark composition but left the mechanism of quark binding unexplained.

The early 1970s witnessed the introduction of the colour charge concept, a quantum property analogous to the electric charge in electromagnetism, yet more intricate with three varieties—red, green, and blue—and their corresponding anti-colours for anti-quarks. This innovative concept paved the way for Quantum Chromodynamics, which theorises that quarks are bound by the exchange of gluons, the mediators of the strong force. Unlike electromagnetism, whose force diminishes with distance, the quark-binding force intensifies as quarks separate, a phenomenon known as asymptotic freedom. This pivotal discovery, predicted by David Gross, Frank Wilczek, and David Politzer, earned them the Nobel Prize in Physics in 2004.

QCD swiftly ascended to become the definitive theory for strong interactions, elucidating not only the cohesion of quarks within hadrons but also phenomena such as jet formation during high-energy collisions. Decades of testing and validation, especially through experiments conducted in particle accelerators like the Large Hadron Collider, have firmly established QCD's place as a fundamental pillar of the Standard Model of particle physics. This theoretical framework has significantly advanced the understanding of the strong force.

---

[1] These are the electromagnetic, weak, strong and gravitational forces

2.1 The Gauge Principle

The gauge principle posits that the laws of physics should remain invariant under local gauge transformations, leading to the formulation of gauge theories that describe the fundamental interactions. In practical terms, gauge invariance refers to the idea that physical phenomena should not depend on arbitrary choices related to the phase of a field at local points in space-time. This invariance under local transformations is a type of symmetry that dictates the interactions between fields and particles.

The implementation of the gauge principle begins with the identification of symmetries associated with a field. For example, quantum electrodynamics (QED) can be derived from an abelian *U(1)* symmetry group. However, QCD must be derived from a nonabelian symmetry group, this means that the symmetry group involves operators that do not commute. More specifically, quantum chromodynamics is based on the *SU(3)* symmetry group. The choice of this Lie group is not arbitrary; it is strongly supported by experimental evidence. The dynamics of the quarks can only be explained with the introduction of an extra quantum number, called *colour*[2], and this colour quantum number has the characteristics that correspond to the *SU(3)* symmetry group. Properties of the strong force, such as quark confinement and the behaviour of the strong force at different energies, can only be explained using this colour quantum number.

2.1.1 Nonabelian Gauge Field

The Yang-Mills (YM) Lagrangian density is the most general nonabelian Lagrangian density using the gauge principle. From the YM, the QCD Lagrangian density can be constructed by choosing the specific Lie group and matter content.

Start with the Lagrangian density for a multiplet ψ of n fields,

$$\mathcal{L} = \bar{\psi}(i\not{\partial} - m)\psi = i\bar{\psi}\not{\partial}\psi - m\bar{\psi}\psi, \tag{2.1.1}$$

where $\not{\partial} = \gamma^\mu \partial_\mu$ denotes the Feynman slash notation. It is easily verified that this Lagrangian density exhibits an invariance to global phase transformations given by[3]

$$G = e^{i\alpha^a T^a}. \tag{2.1.2}$$

These symmetry transformations G[4], with generators T^a, represent the elements of a Lie group. The associated Lie algebra obeys the following commutation relations:

$$[T^a, T^b] = i f^{abc} T^c, \tag{2.1.3}$$

where f^{abc} is a constant and anti symmetric in all indices. Here, *generator* is synonymous with the ”charge” of the theory, associated with a particular Lie group. For example, in QED, there’s a single generator, so only one type of charge: the electric charge. This implies that the electromagnetic force is mediated by a single type of force carrier. In contrast, QCD is represented by eight generators. Consequently, there are eight distinct charges, each with its corresponding force carrier.

---

[2] This is where the name of the theory came from, *chromo* literally means colour in ancient Greek.

[3] In this thesis the Einstein summation notation will be used: $\alpha^a T^a = \sum_a \alpha^a T^a$.

[4] These are $n \times n$ dimensional, unitary operators, acting on ψ.

The gauge principle dictates a promotion from a global invariance to a local invariance. This transformation takes place by having the phase, α^a, depend on the space-time position:

$$G \to G(x) = e^{i\alpha^a(x)T^a}. \tag{2.1.4}$$

However, the initial Lagrangian density described in Eq. (2.1.1) does not retain its form under such local phase transformations, primarily because the partial derivative ∂_μ acts on the field ψ at distinct space-time coordinates. This discrepancy becomes apparent through the derivative's definition:

$$n^\mu \partial_\mu \psi(x) = \lim_{\epsilon \to 0} \frac{\psi(x+\epsilon n) - \psi(x)}{\epsilon}. \tag{2.1.5}$$

The process of making the Lagrangian invariant to local phase transformations can be found in Ref. [1] on pages 45-50. Here, gauge invariance of the Lagrangian requires the introduction of the covariant derivative:

$$D_\mu = \partial_\mu - igA^a_\mu T^a. \tag{2.1.6}$$

where g denotes a constant, and A^a_μ are vector fields associated with each generator. The meaning of the constant will become clear later in this section. The vector fields are called the gauge fields and they represent the gluons within the strong interaction. Furthermore, ensuring gauge invariance involves infinitesimally transforming the gauge fields as

$$A^a_\mu \to A^a_\mu + \frac{1}{g}\partial_\mu \alpha^a - f^{abc}\alpha^b A^c_\mu, \tag{2.1.7}$$

highlighting two key transformation components: the gradient term, responsible for translating the field, and the gauge-rotation term, which signifies an internal space rotation specific to the nonabelian nature of the gauge group.

With both these definitions, the following property holds true:

$$D_\mu \psi(x) \to D_\mu G(x)\psi(x) = G(x) D_\mu \psi(x), \tag{2.1.8}$$

signifying that the Lagrangian, $\mathcal{L} = i\bar{\psi}\not{D}\psi - m\bar{\psi}\psi$, is gauge invariant. Which means that requiring local gauge symmetry, implies the existence of the gauge fields A^a_μ. The expanded Lagrangian, using Eq. (2.1.6), is as follows:

$$\mathcal{L} = i\bar{\psi}\not{\partial}\psi + g\bar{\psi}\not{A}\psi - m\bar{\psi}\psi. \tag{2.1.9}$$

Within this Lagrangian, the initial term with the derivative of the matter fields ψ facilitates the fields' propagation. The second term[5], introduces an interaction between the matter fields ψ and the gauge fields A^a_μ, indicating an exchange process. Here, the constant g emerges as a coupling constant, analogous to the fine-structure constant in electromagnetism, defining the interaction strength. The third term imparts mass m to the matter fields, completing the dynamics of field propagation and interaction.

The Lagrangian, however, lacks a term to describe the propagation of the gauge fields themselves. Given that interactions are theorised to occur through the exchange of these fields, their ability to propagate is implied. To address this, a gauge invariant term is introduced for the

---

[5] With definitions: $\not{A} = \gamma^\mu A_\mu$, and $A_\mu = A^a_\mu T^a$.

propagation of the gauge fields A^a_μ. This is encapsulated by the kinetic term involving the field strength tensor $F_{\mu\nu}$, defined through the commutation of covariant derivatives:

$$[D_\mu, D_\nu]\psi(x) = -igF^a_{\mu\nu}T^a\psi(x), \tag{2.1.10}$$

and the nonabelian field tensor itself given by

$$F^a_{\mu\nu} = \partial_\mu A^a_\nu - \partial_\nu A^a_\mu + gf^{abc}A^b_\mu A^c_\nu, \tag{2.1.11}$$

the derivative acting on the gauge fields implies the gauge fields' capacity for propagation.

To maintain local symmetry in the Lagrangian with the inclusion of $F_{\mu\nu}$, the challenge that this tensor is not inherently Lorentz nor gauge invariant needs to be confronted. The gauge transformation modifies it according to

$$F^a_{\mu\nu}T^a \to G(x)F_{\mu\nu}G^{-1}(x), \tag{2.1.12}$$

The transformation law for the field strength tensor, along with the trace's cyclic property[6], confirm the gauge and Lorentz invariance of the kinetic term. This is demonstrated[7] through the trace of the Lorentz contracted field strength tensor with itself:

$$\mathcal{L}_{Kinetic} = -\frac{1}{2}\mathrm{Tr}[F_{\mu\nu}F^{\mu\nu}] = -\frac{1}{4}F^a_{\mu\nu}F^{a,\mu\nu}. \tag{2.1.13}$$

Thus creating a gauge invariant kinetic term, accounting for the propagation of gauge fields and leading to the formation of the *Yang-Mills* (YM) Lagrangian:

$$\mathcal{L}_{YM} = -\frac{1}{4}F^a_{\mu\nu}F^{a,\mu\nu} + \overline{\psi}(i\not{D} - m)\psi. \tag{2.1.14}$$

This Lagrangian represents the most general nonabelian gauge-invariant form, preserving renormalisability, parity conservation, and time-reversal invariance. Detailed discussions on the renormalisability will be presented in Section 2.3. These symmetries may be broken by introducing additional terms to the Lagrangian. The possibility of such terms for QCD is discussed on page 145-147 on Ref. [1]

2.1.2 QCD Lagrangian

The formulation of a specific Lagrangian in gauge field theory is contingent upon two choices: the matter content of the fields and the gauge group describing the local symmetry.

Quantum chromodynamics was created to treat matter that carries the so-called colour charge, and quarks are the only matter particles that carry colour charge. So, in this case, the quarks make up the matter content. Not only matter carries colour, but the gluon fields are also colour charged, but different from quarks. The effect of gluons are indirectly observed via mathematical deductions from hadron decays. It is observed that a change of colour content for quarks can occur, however the total colour charge is always conserved. This property is called colour confinement and is a fundamental principle of QCD. It states that quarks cannot exist in isolation but must always be found in colour-neutral combinations. The exchange of gluons

---

[6] The convention, $\mathrm{Tr}[T^aT^b] = \frac{1}{2}\delta_{ab}$, for hermitian, traceless matrices used is.

[7] In Ref. [1] on pages 47-50

between quarks changes their colour charge, ensuring that the overall colour charge of a hadron remains neutral. Gluons are viewed as having one colour and one *anti*-colour charge, which does not have to be the same colour. The matter fields in QCD, denoted by ψ_f, encompass six quark *flavours*[8] $f \in \{u, d, c, s, t, b\}$. The multiplet ψ will consist of these six quark fields that correspond to the different flavours. These six flavoured particles do not all have the mass m, they have different masses m_f. Like previously discussed, the colour interactions of these quarks necessitate adopting the *SU(3)* Lie group as the gauge group. The YM Lagrangian does not change significantly when taking this group into account. The group's dimension dictates the number of generators, and therefore also the number of gauge fields. For *SU(3)*, eight generators, give rise to eight corresponding gauge fields—the gluons governing the strong interaction.

The first term in the Lagrangian represents the kinetic energy of the gluons and their self-interactions. Gluons, unlike photons in QED, can interact with each other because of the nonabelian nature of the colour charge. This is captured by the non-linear terms in the field strength tensor, $g_s f^{abc} A_\mu^b A_\nu^c$. These self-interactions lead to rich phenomena such as asymptotic freedom, where the force between quarks becomes weaker at shorter distances or higher energies.

The second term describes the kinetic energy of the quarks and their interaction with the gluon field. The covariant derivative D_μ incorporates the interaction between quarks and gluons and ensures the gauge invariance of the theory. The quark fields ψ_f are spinor fields, reflecting the fact that quarks are fermions with spin $\frac{1}{2}$.

The theory's emphasis on colour might not be immediately apparent from the QCD Lagrangian's initial appearance. This is because each flavour matter field ψ_f comprises of three colour components.

$$\psi_f = \begin{bmatrix} \psi_f^r \\ \psi_f^g \\ \psi_f^b \end{bmatrix}. \tag{2.1.15}$$

It are these components that are acted on and rearranged by the *SU(3)* operators.

The interaction with the *SU(3)* group, however, affects quarks and gluons distinctly, as seen in their transformation properties under separate *SU(3)* representations, defined by the dimension d_R and generators T_R^a specific to each representation. Quarks transform under the fundamental representation associated with three-dimensional space, typically expressed using Gell-Mann matrices λ_a[9]. Antiquarks and gluons are represented by the conjugate and adjoint representations, respectively, with dimensions $d_{\overline{F}} = 3$ for antiquarks and $d_A = 8$ for gluons. Consequently, the form of an *SU(3)* generator or element varies based on the object it is applied to.

2.2 Quantisation of Gauge Field Theories

Central to QCD is the Lagrangian that governs the dynamics of quarks and gluons. The interaction vertices and Feynman rules can be calculated based on these QCD Lagrangian terms. However, this is not yet the complete picture. Everything conducted so far has been grounded

---

[8] The terms *flavour* and *colour* were historically coined by Murray Gell-Mann and his student Harald Fritzsch. They came up with the idea of quark colour and flavour in an ice cream store, because ice cream also has a colour and a flavour.

[9] The generators in this representation incorporate a factor $\frac{1}{2}$ in front of the Gell-Mann matrices, notated as $T_F^a = \frac{1}{2}\lambda_a$.

in classical physics, but due to the microscopic scale of hadrons and the need to observe their components at even finer resolutions, it becomes necessary to apply quantum theory. Additionally, the high velocities at which the particles collide necessitate the consideration of special relativity. These demands justify the *quantum field* theory treatment of the strong interaction; which begins by quantising the theory.

The quantisation of gauge theories like QCD introduces challenges due to *gauge redundancy*, which arises from the physically equivalent field configurations permissible by the theory. An illustration of this redundancy is the gauge field transformation in abelian theories[10],

$$A_\mu \to A_\mu + \frac{1}{g}\partial_\mu \alpha. \tag{2.2.1}$$

Considering the Fourier transformation

$$A(x) = \int \frac{d^4k}{(2\pi)^4} e^{ik\cdot x} \tilde{A}(k) \tag{2.2.2}$$

and the resulting longitudinal shift[11] in Fourier space,

$$\tilde{A}_\mu(k) \to \tilde{A}_\mu(k) + \frac{1}{g}k_\mu \alpha \tag{2.2.3}$$

it becomes evident that such shifts do not yield new physical configurations. Gauge fields thus exhibit only 'transverse' degrees of freedom. By parametrising A_μ using a polarisation 4-vector ε_μ,

$$\tilde{A}_\mu(k) = a(k)\varepsilon_\mu \tag{2.2.4}$$

where $a(k)$ is called the field amplitude. Physical phenomena remain invariant under

$$\varepsilon_\mu \to \varepsilon_\mu + \alpha k_\mu. \tag{2.2.5}$$

The photon, despite its spin-1 nature, exhibits only two *transverse* polarisation states, due to its role as a gauge field's quantum. In quantum mechanics, a spin-1 particle theoretically possesses three polarisation states. However, the uniqueness of photons stems from the necessity to account for gauge redundancy in quantisation, distinguishing physically relevant degrees of freedom. The intricacy of QCD quantisation emerges from the added layer of gauge rotation. Without addressing gauge redundancy, quantisation efforts risk including non-physical degrees of freedom. The strategy used in this thesis involves quantising all degrees initially, then isolating the physical ones. Functional integral quantisation, utilising Lagrangian formalism and path integrals, is particularly adept at handling the intricacies of gauge fields, albeit requiring advanced mathematical concepts to derive the QCD Lagrangian's quantum version.

2.2.1 The Abelian Case

It is, in fact, appealing to first take up the abelian case, recognise the problem within quantisation of gauge field theories, solve it, and then move over to the nonabelian case. Within

---

[10] This transformation corresponds to the first term added in the nonabelian transformation equation (2.1.7).

[11] A differential operator becomes a multiplicative operator in Fourier space.

the functional integral quantisation framework, the gauge theory's dynamics are encapsulated by the functional integral

$$\int \mathcal{D}A e^{iS[A]} \tag{2.2.6}$$

where A represents the gauge field and S denotes the action as a functional of A:

$$S[A] = \int d^4x \, \mathcal{L}. \tag{2.2.7}$$

The gauge redundancy comes solely from the gauge transformations, this means that only the bosonic part causes trouble. Therefore, the Lagrangian can be simplified to the kinetic term for the gauge boson:

$$S[A] = \int d^4x \left(-\frac{1}{4}F_{\mu\nu}F^{\mu\nu}\right) \tag{2.2.8}$$

where $F_{\mu\nu}$ is the field strength tensor defined by $F_{\mu\nu} = \partial_\mu A_\nu - \partial_\nu A_\mu$ and is inherently anti-symmetric: $F_{\mu\nu} = -F_{\nu\mu}$. Delving into the action's exponent and employing this anti-symmetry leads to

$$\begin{aligned}
-\frac{1}{4}\int d^4x \, F_{\mu\nu}F^{\mu\nu} &= \frac{1}{4}\int d^4x \, (\partial_\mu A_\nu - \partial_\nu A_\mu)(\partial^\nu A^\mu - \partial^\mu A^\nu) && (2.2.9)\\
&= \frac{1}{4}\int d^4x \, (2\partial_\nu A_\mu \partial^\mu A^\nu - 2\partial_\nu A_\mu \partial^\nu A^\mu) && (2.2.10)\\
&= \frac{1}{2}\int d^4x \, (\partial_\mu A_\nu - \partial_\nu A_\mu)(\partial^\nu A^\mu) && (2.2.11)\\
&= \frac{1}{2}\int d^4x \, (\partial^\nu A^\mu)(\partial_\mu A_\nu - \partial_\nu A_\mu). && (2.2.12)
\end{aligned}$$

Applying integration by parts yields

$$\begin{aligned}
-\frac{1}{4}\int d^4x \, F_{\mu\nu}F^{\mu\nu} &= -\frac{1}{2}\int d^4x \, A^\mu(\partial^\nu\partial_\mu A_\nu - \partial^\nu\partial_\nu A_\mu) && (2.2.13)\\
&= \frac{1}{2}\int d^4x \, A^\mu(\partial^2 g_{\mu\nu} - \partial_\mu\partial_\nu)A^\nu && (2.2.14)
\end{aligned}$$

where $g_{\mu\nu}$ signifies the metric's components. The operator $\partial^2 g_{\mu\nu}$ denotes the application of ∂^2 on A^ν after it has been contracted with $g_{\mu\nu}$, and it is important to note that the metric itself, being constant in Minkowski space, does not undergo differentiation.

Proceeding by applying a Fourier transformation to the gauge field $A^\mu(x)$:

$$A^\mu(x) = \int \frac{d^4k}{(2\pi)^4} \, e^{ik\cdot x} \tilde{A}^\mu(k). \tag{2.2.15}$$

Substituting this into the expression for the kinetic term:

$$\begin{aligned}
-\frac{1}{4}\int d^4x \, F_{\mu\nu}F^{\mu\nu} &= \frac{1}{2}\int \frac{d^4k}{(2\pi)^4} \tilde{A}^\mu(k) \left(-k^2 g_{\mu\nu} + k_\mu k_\nu\right) \tilde{A}^\nu(-k) && (2.2.16)\\
&= \frac{1}{2}\int \frac{d^4k}{(2\pi)^4} \tilde{A}^\mu(k) \left(-k^2 P^\perp_{\mu\nu}\right) \tilde{A}^\nu(-k) && (2.2.17)
\end{aligned}$$

where $P^{\perp}_{\mu\nu}$ denotes the transverse projection operator defined as

$$P^{\perp}_{\mu\nu} = g_{\mu\nu} - \frac{k_\mu k_\nu}{k^2}. \tag{2.2.18}$$

This operator ensures that the longitudinal components of a 4-vector field (i.e. A^μ) are nullified while preserving its transverse components. The transverse components are the sole non-vanishing contributions after the application of $P^{\perp}_{\mu\nu}$. Longitudinal vectors parallel to k^μ are eigenvalues of this operator with an eigenvalue of zero:

$$\tilde{A}^\mu(k) = \alpha k^\mu \tag{2.2.19}$$

where α is a scalar. Therefore, the transverse projection operator will project the infinite many longitudinal shifts – coming from the gauge redundancy – to zero. Consequently, this results in an infinite multiplicity of field configurations where the action is nullified, leading to:

$$\int \mathcal{D}A e^{iS[A]} = \int \mathcal{D}A \cdot 1 = \int \mathcal{D}A \to \infty, \tag{2.2.20}$$

The action is exclusively dependent on the field's transverse components due to the projection operator in the Lagrangian. Nonetheless, the path integral extends over both transverse and longitudinal components, which causes the divergence.

Overcoming the challenges presented by gauge redundancy in quantum field theories involves discerning and accounting for physically equivalent configurations. These equivalent configurations, such as k^μ and all multiples thereof, αk^μ, must be recognised as a single configuration in the functional integral to avoid infinite overcounting. The goal is to isolate and count only the physical configurations. A forthcoming section will introduce a method for integrating constraints into path integrals, it involves in fixing the gauge to eliminate the redundancy. Once a specific gauge is chosen, gauge invariance, and thereby gauge-equivalent configurations, ceases to exist.

The *Faddeev-Popov* (FP) method strategically incorporates gauge constraints into the path integral, using Dirac-delta distributions to filter out equivalent configurations. This method imposes a gauge condition on the transformed field by incorporating a function G of the field post-transformation into the Dirac-delta argument. For instance, employing the Lorenz gauge $\partial_\mu A^\mu = 0$, the Dirac-delta distribution in the path integral becomes $G(A^\alpha)$ for the transformed field A^α. The insertion of this distribution is not done arbitrarily, this would alter the integral, but it is justified by a functional identity:

$$1 = \int \mathcal{D}\alpha \, \det\left(\frac{\delta G(A^\alpha)}{\delta \alpha}\right) \delta(G(A^\alpha)) \quad \text{with} \quad A^\alpha_\mu = A_\mu + \partial_\mu \alpha, \tag{2.2.21}$$

where A^α_μ is the gauge-transformed of A_μ. This identity is analogous to

$$1 = \int dx \, \delta\left(\frac{\delta G}{\delta x}\right) \delta(G(x - x')) \tag{2.2.22}$$

which corresponds[12] to the *sifting*- or *sampling property*, $1 = \int dx \, \delta(x - f(x'))$. Applying this

---

[12] This becomes evident when the chain rule is used backwards.

functional identity to the path integral:

$$\int \mathcal{D}A \exp(iS[A]) = \int \mathcal{D}A \exp(iS[A]) \int \mathcal{D}\alpha \, \det\left(\frac{\delta G}{\delta\alpha}\right) \delta(G(A^\alpha)) \exp(iS[A]) \delta(G(A^\alpha)) \tag{2.2.23}$$

$$= \int \mathcal{D}\alpha \int \mathcal{D}A \, \det\left(\frac{\delta G(A^\alpha)}{\delta\alpha}\right) \delta(G(A^\alpha)) \exp(iS[A]), \tag{2.2.24}$$

where the gauge fixing condition is given by:

$$G(A^\alpha) = \partial_\mu A^{\mu\alpha} = 0, \tag{2.2.25}$$

$$A^{\mu\alpha} = A^\mu + \frac{1}{e}\partial^\mu \alpha. \tag{2.2.26}$$

Using the Lorenz gauge in the abelian case, results in the determinant factor $\det(\delta G(A^\alpha)/\delta\alpha)$ being independent of the field A:

$$\det\left(\frac{\delta G(A^\alpha)}{\delta\alpha}\right) = \frac{1}{e} \det \partial^2. \tag{2.2.27}$$

Adjusting the integration variable to $A \to A^\alpha$ and renaming the dummy variable A^α back to A, the integral (2.2.24) simplifies to

$$\int \mathcal{D}A \exp(iS[A]) = \int \mathcal{D}\alpha \, \det\left(\frac{\delta G(A)}{\delta\alpha}\right) \int \mathcal{D}A \delta(G(A)) \exp(iS[A]). \tag{2.2.28}$$

Since $\det(\delta G(A)/\delta\alpha)$ is shown to be independent of A, it can be extracted from the integral over A. This approach works for a specific gauge choice, but its applicability to a more general gauge selection will also be explored. A gauge is chosen where the determinant $\det(\delta G/\delta\alpha)$ remains unchanged, allowing use of the results derived for the Lorenz gauge $G(A) = \partial_\mu A^\mu$. Adopting the generalised Lorenz condition $\partial_\mu A^\mu(x) = \omega(x)$, instead of the specific $\omega(x) \equiv 0$, and functionally integrating over ω with a Gaussian weight $\exp(-\omega^2/2\xi)$, results in

$$\int \mathcal{D}A \exp(iS[A]) = C \int \mathcal{D}\omega e^{-\int \frac{\omega^2}{2\xi} d^4x} \int \mathcal{D}\alpha \, \det\left(\frac{\delta G(A)}{\delta\alpha}\right) \int \mathcal{D}A e^{iS[A]} \delta(\partial_\mu A^\mu - \omega) \tag{2.2.29}$$

$$= C \int \mathcal{D}\alpha \, \det\left(\frac{\delta G(A)}{\delta\alpha}\right) \int \mathcal{D}A e^{iS[A]} e^{-\int \frac{(\partial\cdot A)^2}{2\xi} d^4x} \tag{2.2.30}$$

$$= C \int \mathcal{D}\alpha \, \det\left(\frac{\delta G(A)}{\delta\alpha}\right) \int \mathcal{D}A e^{i\int d^4x \left(-\frac{1}{4}F_{\mu\nu}F^{\mu\nu} - \frac{1}{2\xi}(\partial\cdot A)^2\right)}, \tag{2.2.31}$$

Here are two integrals, the first one is an infinite gauge-volume factor, the second one is the gauge-field functional integral, which contains the gauge-fixed Lagrangian $\mathcal{L}_{GF}$,

$$\mathcal{L}_{GF} = -\frac{1}{4}F_{\mu\nu}F^{\mu\nu} - \frac{1}{2\xi}(\partial\cdot A)^2. \tag{2.2.32}$$

The resolving of gauge redundancy by factoring out the infinite gauge-volume factor comes at the cost of amending the action. This formulation paves the way to evaluate physical observables $\mathcal{O}$ through their vacuum expectation values:

$$\langle\mathcal{O}\rangle = \frac{\int \mathcal{D}A \mathcal{O} e^{iS[A]}}{\int \mathcal{D}A e^{iS[A]}} = \frac{\int \mathcal{D}A \mathcal{O} \exp\left(i\int d^4x \, \mathcal{L}_{GF}\right)}{\int \mathcal{D}A \exp\left(i\int d^4x \, \mathcal{L}_{GF}\right)}. \tag{2.2.33}$$

The operator $\mathcal{O}$ is purely physical, so it remains unaffected by the unphysical gauge-volume factor. Which means that it can be pulled out from the integral. Consequently, the integral divides into two segments: an infinite, non-physical part and a finite, physical part, the latter stabilised by the gauge-fixing modification (characterised with the parameter ξ). This division ensures that unphysical degrees of freedom, which could potentially lead to divergences, are canceled out in both the numerator and the denominator of the path integral.

This reveals that in the abelian framework, the Lagrangian necessitates an additional term for quantisation, ensuring physical outcomes. This transforms the previous choice of a specific gauge into a choice of the value of ξ. This same scenario occurs for the nonabelian scenario, but further modifications to the Lagrangian are needed.

2.2.2 The Nonabelian Case

Transitioning from the abelian to the more complex nonabelian gauge field theories introduces a distinct difference: the functional determinant $\det\left(\frac{\delta G(A^\alpha)}{\delta\alpha}\right)$ becomes dependent on the gauge field A due to

$$A^{\alpha\mu} = A^\mu + D^{\mu,ac}\alpha^c. \tag{2.2.34}$$

This results in the determinant being represented as

$$\det\left(\frac{\delta G}{\delta\alpha}\right) = \det\left(\frac{1}{g}\partial_\mu D^\mu\right), \tag{2.2.35}$$

where $D^{\mu,ac} = \partial^\mu\delta^{ac} + gf^{abc}A^{\mu,b}$ denotes the covariant derivative in the adjoint representation[13]. The inclusion of A in the covariant derivative introduces a dependence on A not present in the abelian scenario, where differentiation with respect to α did not involve A. Unlike the abelian case, where the functional determinant could be pulled out from the integral over A, the nonabelian case does not permit this due to the A-dependence. An additional mechanism is required to address the divergences.

Introducing the ghost c and anti-ghost $\bar{c}$ fields; which are adjoint, scalar and anti-commuting, a functional integral is employed[14] using Eq. (2.2.35)

$$\det\left(\frac{\delta G}{\delta\alpha}\right) = \int \mathcal{D}c\,\mathcal{D}\bar{c}\,\exp\left(-i\int d^4x\,\bar{c}\partial_\mu D^\mu c\right). \tag{2.2.36}$$

Mirroring the abelian procedure but with the determinant integrated with the gauge fields. The resultant functional integral for the nonabelian gauge field, starting from Eq. (2.2.29), is

$$\int \mathcal{D}A e^{iS[A]} = C\int\mathcal{D}\alpha\int\mathcal{D}c\int\mathcal{D}\bar{c}\int\mathcal{D}A\left[e^{i\int d^4x\mathcal{L}_Q}\right], \tag{2.2.37}$$

$$\text{with } \mathcal{L}_Q = -\frac{1}{4}F^a_{\mu\nu}F^{\mu\nu,a} - \frac{1}{2\xi}((\partial_\mu A^\mu)^a)^2 - \bar{c}^a\partial_\mu D^{\mu,ac}c^c. \tag{2.2.38}$$

These new fields c and $\bar{c}$ are associated, respectively, with 'ghost' and 'anti-ghost' particles. They are essential for the quantisation process and ensure that physical observables remain unaffected

---

[13] As previously mentioned, the adjoint representation is used for gluons and the quantisation problem occurs for the gluon kinetic term due to the transverse projection operator.

[14] The derivation, which is complex, can be found detailed across pages 299–301 and 513–514 in [17].

by ghost contributions. Ghost fields' physical interpretation is rooted in the nonabelian nature of QCD, particularly evident in small ($\alpha^a \ll 1$) transformations of the gauge field:

$$A^{\mu,a} \to A^{\mu,a} + \frac{1}{g}\partial^\mu \alpha^a + f^{abc} A^{\mu,b} \alpha^c. \tag{2.2.39}$$

This transformation showcases the longitudinal shift and the colour gauge rotation, underscoring the unique interaction dynamics in nonabelian theories where gauge charges are matrices. In the colour gauge rotation, the unphysical, longitudinal components reinteract with the physical gauge field A^μ. However, this would result in unphysical contributions. To cancel these contributions, it is precisely these unphysical ghost fields that need to be introduced. It is crucial to note that ghost fields are non-observable and are absent in physical final states.

The inclusion of ghost terms in the nonabelian gauge theory Lagrangian, as necessitated by Eq. (2.2.38), addresses the augmented gauge redundancy in QCD. This necessitates not only a gauge-fixing term but also a ghost term for accurate quantisation. The Lagrangian for the ghost fields specifically unfolds as:

$$\mathcal{L}_{\text{ghost}} = -\bar{c}^a \partial_\mu D^{\mu,ac} c^c = -\bar{c}^a \partial^2 c^a - g f^{abc} \bar{c}^a \partial^\mu (A^{\mu,b} c^c), \tag{2.2.40}$$

capturing both the ghost kinetic energy and the interaction between ghost and gauge fields. In the abelian scenario, where $f^{abc} \to 0$, ghost fields disengage from gauge-field interactions.

All these additional quantisation terms result in the complete QCD Lagrangian at the quantum level:

$$\mathcal{L}_{QCD} = -\sum_{a=1}^{8} \frac{1}{4} F^a_{\mu\nu} F^{a,\mu\nu} + \sum_f \overline{\psi}_f (i\not{D} - m_f)\psi_f - \frac{1}{2\xi}((\partial_\mu A^\mu)^a)^2 - \bar{c}^a \partial_\mu D^{\mu,ac} c^c \tag{2.2.41}$$

containing the quark segment from its classical counterpart, and the gauge invariant kinetic term for gluons — these two terms form the classical Yang-Mills Lagrangian. The gauge-fixing and ghost terms emerge distinctly in the quantum domain. In Appendix A.1, the Feynman rules of the QCD Lagrangian are shown.

2.3 Renormalisation

The QCD Lagrangian details all possible vertices and propagators for particles with a non-trivial colour quantum number, allowing for the construction of various diagrams representing fundamental particle interactions at the tree level. However, the tree-level only provides an approximation. The real complexity arises from interactions mediated by the exchange of a boson. At this level, it might seem as if particles somehow pre-emptively 'know' to exchange a boson, but this is not the case. Instead, particles continuously emit bosons as they traverse through spacetime; occasionally, these bosons are absorbed by other particles, constituting what is recognised as an interaction. These emitted particles, termed 'virtual particles,' are volatile and are governed by the Heisenberg uncertainty principle. This constant emergence of virtual particles leads to an infinite array of potential interaction diagrams, all contributing to a comprehensive description of particle interactions. The same initial and final states can be achieved through a myriad of intermediate processes involving the creation and annihilation of virtual particles. In QED, the likelihood of a process decreases with the increase in interaction vertices involving virtual particles, justifying the tree-level approximation within certain energy bounds where the coupling constant remains small, suitable for perturbative approaches. However, this series of interactions is inherently divergent. To render the results finite and physically interpretable, renormalisation is employed. This process involves redefining the theory parameters, like charges and wave functions, to remove divergences. Initially postulated theoretical constructs (from the Lagrangian) are thus not directly observable; renormalisation adjusts these to reflect measurable properties, turning 'constants' like coupling into variables dependent on the energy scale. These divergences, specifically ultraviolet (UV) divergences[15], arise from diagrams that incorporate loops, such as a transient particle-antiparticle pair. To account for all possible momenta in these loops—since arbitrarily high momenta lead to divergences—an integral over all possible momenta is necessary, culminating in the UV divergences.

To determine the renormalisability of a theory, a clear mathematical definition of what constitutes a *renormalisable* theory needs to be established. Renormalisation aims to refine theoretical predictions, ensuring that all physical observables are devoid of UV divergences. A mathematical framework for defining a renormalisable theory employs the method known as *ultraviolet power counting.* Consider a Feynman graph characterised by a loop, resulting in an integral of the form:

$$\int d^4k \frac{N(k)}{M(k)}, \tag{2.3.1}$$

where $N(k)$ and $M(k)$ are functions of the loop momentum k. To assess potential divergences, the *superficial degree of divergence* D is calculated,

$$D := 4 + \text{degree of } N \text{ in } k - \text{degree of } M \text{ in } k. \tag{2.3.2}$$

If $D \geq 0$, the integral is classified as UV divergent. A theory is deemed renormalisable if it contains only a finite number of such divergent amplitudes. Examples of such theories include QED and QCD, with respectively three and seven divergent amplitudes.

The term *divergent amplitude* specifically refers to the types of Feynman diagrams that inherently include UV divergences, not to the unbounded number of UV divergent Feynman graphs a theory might contain. The divergent amplitudes in QED are depicted in Figure 2.1 These configurations typically involve various combinations of incoming and outgoing particles with unspecified interactions between them.

Once a theory is identified as renormalisable, the actual renormalisation process is carried out in the following steps:

1. First, having identified all divergent amplitudes, such as those for QED in Figure 2.1, renormalisation is initiated by employing a *regularisation method.* This involves introducing additional parameters, termed *regulators*, into the amplitudes. These regulators allow a manipulation of the parameters instead of dealing directly with infinities. In a specific limit of these parameters, the original divergent integral re-emerges. It is crucial that the observables remain independent of these regulators. A divergent loop integral can be split into a finite part, where the momentum ranges from zero to a chosen mass scale parameter μ, called the *renormalisation scale*, and a divergent part that integrates all momenta from μ to infinity. Introducing a cut-off Λ in the high-momentum (divergent) region is one regularisation approach. Here, the upper bound of the integral's divergent part is

---

[15] The momentum corresponding to these divergences lies in the high energy region, explaining the terminology of ultraviolet

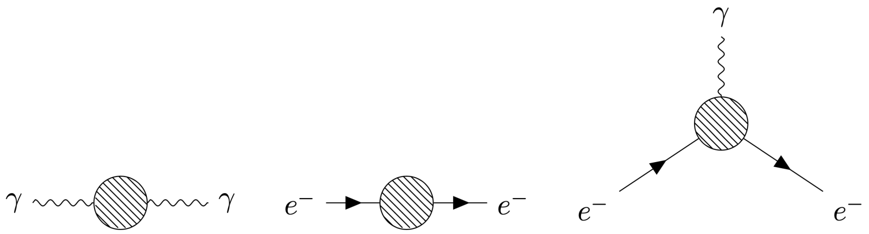

(a) Photon self-energy (b) Electron self-energy (c) Electron-photon vertex

Figure 2.1: UV divergent amplitudes in QED. The blobs indicate undetermined interactions that could involve any number of loops allowed by the theory.[1]

Λ, rather than infinity. The original divergent integral is returned when taking the limit $\Lambda \to \infty$. Another prevalent method in QFT is *dimensional regularisation*, which maintains the fundamental symmetries of the theory. This method involves reducing the spacetime dimension to below four (e.g., $4 - \epsilon$) to decrease the superficial degree of divergence, D.

2. The next step involves rescaling the parameters and wave functions within the theory. For any quantity ϕ, the rescaling takes the form $\phi \to \phi_0 = Z\phi,$. Here, ϕ becomes the renormalised quantity and ϕ_0 the unrenormalised quantity post-rescaling and Z is a calculable *renormalisation constant* that absorbs the divergence. All renormalisation constants are theoretically non-observable and potentially divergent, representing no physical quantity.

3. After completing the rescaling and expressing the theory entirely in terms of renormalised quantities, all derived predictions are non-divergent. Physical quantities are finite, calculable, and free from divergences.

Through this outlined programme, renormalisability can be redefined: a theory that yields finite results for all physical quantities post-renormalisation is renormalisable. Conversely, a non-renormalisable theory has excessive divergences that cannot be absorbed by a finite number of renormalisation constants. It is important to note that, while QED and QCD are gauge theories, this renormalisation programme applies to other types of theories. Furthermore, gauge theories require additional considerations. The renormalisation of gauge theories is intricately linked to gauge symmetry, necessitating further constraints on the renormalisation constants to ensure consistency within the theory.

2.3.1 Renormalisation Group

The process of renormalisation inherently introduces an arbitrary scale, the renormalisation scale μ, which should not influence the physical outcomes of the theory, as it is not a physical parameter, but merely a mathematical artefact. The Renormalisation Group (RG) formalism ensures this scale invariance through specific equations that maintain the consistency of physical predictions across different scales, providing deeper insights into the asymptotic behaviour of coupling constants at large energy scales or short distances. In QED, the coupling constant increases with energy (see Ref. [17] on p. 244-255), limiting the effectiveness of low-order perturbative calculations to low energies. In contrast, QCD exhibits a decrease in coupling strength at higher energies, this will be shown later in this chapter. This makes perturbative methods only viable above certain thresholds; below these thresholds, the theory becomes 'non-perturbative' due to inaccuracies in truncated series results.

To summarise the previous discussion on renormalisability: renormalisation aims to remove divergences in physical quantities. A theory is renormalisable if for every unrenormalised quantity ϕ_0, its divergent components can be isolated and absorbed into a renormalisation constant Z. Moreover, the renormalised quantity, denoted ϕ, should be expressed not just in terms of itself and its parameters, but explicitly in terms of the renormalisation scale and the renormalised coupling constants. This relationship can be captured by the following equation:

$$\phi(p_i, \alpha_0) \to \phi_0(p_i, \alpha_0) = Z\phi(p_i, \alpha, \mu). \tag{2.3.3}$$

To clarify, in the unrenormalised theory, the physical quantity is referred to as ϕ, a function of the momenta p_i and the bare coupling α_0. However, this version of ϕ contains divergences. Through renormalisation, this is transformed into ϕ_0, effectively removing the divergent parts and incorporating them into Z. The renormalised version, which is still denoted by ϕ, thus becomes a fundamentally different function, now dependent on an additional variable, μ. The relationship between the renormalised and unrenormalised quantities is therefore given by $\phi_0(p_i, \alpha_0) = Z\phi(p_i, \alpha, \mu)$, which highlights the transformation imposed by renormalisation.

The fundamental principle of the RG approach is to embed the invariance under changes in μ directly into the renormalisation process. This is achieved using the Renormalisation Group Equation (RGE). It is immediately evident from Eq. (2.3.3) that while the left-hand side explicitly shows no dependence on μ, the right-hand side includes terms that do depend on μ. This apparent contradiction implies that any dependence of ϕ on μ must be exactly offset by the renormalisation constant Z. To express this cancellation of μ dependence, the derivative of ϕ_0 is considered with respect to μ:

$$\frac{d\phi_0}{d\mu} = 0. \tag{2.3.4}$$

For convenience in subsequent calculations, the derivative with respect to $\ln \mu^2$ is taken instead:

$$\frac{d\phi_0}{d(\ln \mu^2)} = 0. \tag{2.3.5}$$

This equivalence is evident through the application of the chain rule

$$\frac{d\phi_0}{d(\ln \mu^2)} = \frac{d\phi_0}{d\mu}\frac{d\mu}{d(\ln \mu^2)}, \tag{2.3.6}$$

where $\frac{d\mu}{d(\ln \mu^2)}$ is nonzero, affirming that $\frac{d\phi_0}{d(\ln \mu^2)} = 0$ implies $\frac{d\phi_0}{d\mu} = 0$. Taking the right-hand side of Eq. (2.3.3), it follows that

$$\frac{d(Z\phi)}{d(\ln \mu^2)} = 0. \tag{2.3.7}$$

Applying the Leibniz rule and the chain rule, and noting that p_i does not depend on μ and Z

depends only on μ, yields:

$$\begin{aligned}\frac{d(Z\phi)}{d(\ln\mu^2)} &= Z\frac{d\phi}{d(\ln\mu^2)} + \phi\frac{dZ}{d(\ln\mu^2)} && (2.3.8)\\ &= Z\frac{\partial\phi}{\partial(\ln\mu^2)} + Z\frac{\partial\phi}{\partial\alpha}\frac{\partial\alpha}{\partial(\ln\mu^2)} + \phi\frac{dZ}{d(\ln Z)}\frac{d(\ln Z)}{d(\ln\mu^2)} && (2.3.9)\\ &= Z\frac{\partial\phi}{\partial(\ln\mu^2)} + Z\frac{\partial\phi}{\partial\alpha}\frac{\partial\alpha}{\partial(\ln\mu^2)} + \phi Z\frac{d\ln Z}{d(\ln\mu^2)} && (2.3.10)\\ &= Z\left[\frac{\partial\phi}{\partial(\ln\mu^2)} + \frac{\partial\phi}{\partial\alpha}\frac{\partial\alpha}{\partial(\ln\mu^2)} + \phi\frac{d\ln Z}{d(\ln\mu^2)}\right] = 0. && (2.3.11)\end{aligned}$$

This relationship simplifies to

$$\frac{\partial\phi}{\partial(\ln\mu^2)} + \frac{\partial\phi}{\partial\alpha}\frac{\partial\alpha}{\partial(\ln\mu^2)} + \phi\frac{d\ln Z}{d(\ln\mu^2)} = 0. \tag{2.3.12}$$

Alternatively, it can be expressed as

$$\left[\frac{\partial}{\partial(\ln\mu^2)} + \frac{\partial\alpha}{\partial(\ln\mu^2)}\frac{\partial}{\partial\alpha} + \frac{d\ln Z}{d(\ln\mu^2)}\right]\phi = 0. \tag{2.3.13}$$

By defining the beta function $\beta(\alpha)$ and the anomalous dimension $\gamma(\alpha)$ as:

$$\beta(\alpha) = \frac{\partial\alpha}{\partial\ln\mu^2}, \tag{2.3.14}$$

$$\gamma(\alpha) = \frac{\partial\ln Z}{\partial\ln\mu^2}, \tag{2.3.15}$$

Eq. (2.3.13) transforms into:

$$\left[\frac{\partial}{\partial(\ln\mu^2)} + \beta(\alpha)\frac{\partial}{\partial\alpha} + \gamma(\alpha)\right]\phi(p_i,\alpha,\mu) = 0. \tag{2.3.16}$$

Assuming that ϕ is measurable at a specific physical mass scale Q, ϕ can be determined as a function evaluated at $\mu = Q$. To facilitate this, the arguments (excluding the coupling) of ϕ are rescaled based on Q, leading to the definition of a new function F, which represents the same physical quantity as ϕ:

$$\phi(p_i,\alpha,\mu) = F(x_i,t,\alpha), \tag{2.3.17}$$

where

$$x_i := \frac{p_i}{Q}, \quad t := \ln\frac{Q^2}{\mu^2}. \tag{2.3.18}$$

This rescaling simplifies the model and when substituted into Eq. (2.3.16), results in:

$$\left[-\frac{\partial}{\partial t} + \beta(\alpha)\frac{\partial}{\partial\alpha} + \gamma(\alpha)\right]F(x_i,t,\alpha) = 0. \tag{2.3.19}$$

This equation is known as the *renormalisation group evolution equation*. The solution to this equation can be determined by setting a boundary condition such that at $t = 0$ ($\equiv \mu = Q$), F is known and denoted by $F(0, \alpha)$. The form of the solution is[16]:

$$F(t, \alpha) = F(0, \alpha(t)) \exp\left(\int_{\alpha}^{\alpha(t)} \frac{\gamma(\alpha')}{\beta(\alpha')} d\alpha'\right), \tag{2.3.20}$$

where $\alpha(t)$ is implicitly defined as:

$$t = \int_{\alpha}^{\alpha(t)} \frac{d\alpha'}{\beta(\alpha')}, \tag{2.3.21}$$

with $\alpha = \alpha(0)$. By applying a change of integration variable as per this definition, Eq. (2.3.20) is transformed into:

$$F(t, \alpha) = F(0, \alpha(t)) \exp\left(\int_{0}^{t} dt' \gamma(\alpha(t'))\right). \tag{2.3.22}$$

This solution reveals significant insights into the physics of the problem, illustrating that the coupling α varies with t, and consequently with μ, through the β function. The β function elucidates how the coupling changes with the energy scale, demonstrating the initial signs of breaking the scale invariance.

The exponential term further elucidates the role of the γ function, or the *anomalous dimension*, especially when $\gamma(\alpha)$ is approximated linearly as $\gamma(\alpha) = \gamma_1 \alpha$. Under this simplification, the solution becomes as follows:

$$\exp\left(\int_{0}^{t} dt' \gamma(\alpha)\right) = \exp\left(\int_{0}^{t} dt' \gamma_1 \alpha\right) = \exp\left(\gamma_1 \alpha t\right), \tag{2.3.23}$$

which, using the definition of t, translates to:

$$\exp\left(\int_{0}^{t} dt' \gamma(\alpha)\right) = \exp\left(\gamma_1 \alpha \ln \frac{Q^2}{\mu^2}\right) = \exp\left(\ln\left(\left(\frac{Q^2}{\mu^2}\right)^{\gamma_1 \alpha}\right)\right) = \left(\frac{Q^2}{\mu^2}\right)^{\gamma_1 \alpha}. \tag{2.3.24}$$

Substituting this back into the solution of the RGE (Eq. (2.3.22)) yields:

$$F(t, \alpha) = F(0, \alpha(t)) \left(\frac{Q^2}{\mu^2}\right)^{\gamma_1 \alpha} \sim F(0, \alpha(t)) Q^{2\gamma_1 \alpha} = F(0, \alpha(t)) Q^{2\gamma(\alpha)}. \tag{2.3.25}$$

Here, the function $F(t, \alpha)$ acquires dimensions in Q modified by the factor $Q^{2\gamma_1 \alpha} = Q^{2\gamma(\alpha)}$, indicating that γ confers additional dimensions in Q and thus is termed the '*anomalous dimension*'. This γ function introduces another mechanism for the breaking of scale invariance, alongside the β function. As the physical scale Q changes, so does the physical quantity F, altering what are known as the *engineering dimensions*[17] of F by incorporating dependencies based on $\gamma(\alpha)$.

2.3.2 Running of The Coupling

Incorporating loops within quantum field theory necessitates the use of renormalisation to manage quantum fluctuations at high-energy scales. This process introduces an unphysical

---

[16] The variable x_i is left out in F as it is not relevant to the analysis.

[17] The dimensions of Q in $F(0, \alpha)$ are the intuitive dimensions associated to the quantity F.

parameter, the renormalisation scale μ, which ultimately does not appear in the expressions for any physical quantities in the renormalised theory. However, the inclusion of loops does leave a physical imprint observable as the energy scale dependence of the coupling constants, manifesting as a violation of scale invariance. The RG approach is apt for describing this effect, particularly through the RGE that elucidate the behaviour of the strong coupling constant α_s. This property, known as asymptotic freedom, explains the nearly free behaviour of quarks at high energies or, equivalently, short distances and their confinement within hadrons at lower energies or longer distances. The universal functions β and γ govern the necessary adjustments to parameters and wave functions to compensate for changes in μ, applicable across all theories.

For QCD, limited to one loop, this method extends to calculate the one-loop β function. Three of the UV divergent amplitudes relevant to QCD are illustrated in Fig. 2.2, encompassing the total corrections to the quark-gluon vertex, the quark propagator (quark self-energy), and the gluon propagator (gluon self-energy). QCD contains seven such UV divergent amplitudes, depicted in Appendix A.1, where modifications at the vertices or within the propagators are marked by a blob.

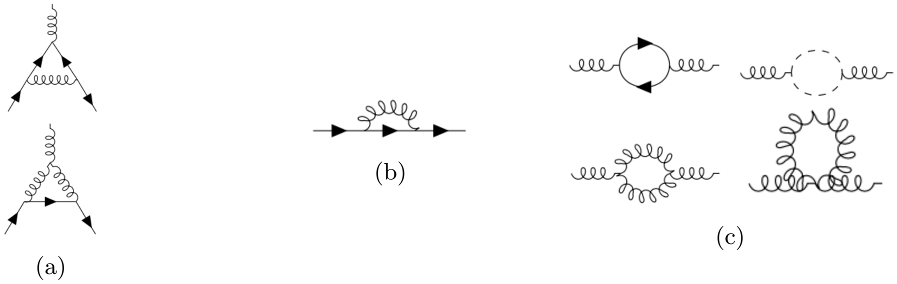

Figure 2.2: One-loop contributions to three of the UV divergent amplitudes in QCD: (a)The one-loop corrections to the quark-gluon vertex, (b) The one-loop correction to the quark self-energy, (c) The four one-loop corrections to the gluon self-energy.

The necessary renormalisation constants in QCD are defined to absorb these divergences, similar to (2.3.3):

$$A \to A_0 = \sqrt{Z_3}A, \tag{2.3.26}$$

$$\psi \to \psi_0 = \sqrt{Z_2}\psi, \tag{2.3.27}$$

$$c \to c_0 = \sqrt{\tilde{Z}_3}c, \tag{2.3.28}$$

$$m \to m_0 = \frac{Z_m}{Z_2}m. \tag{2.3.29}$$

Here, the first line adjusts the gluon wave function, followed by the fermion wave function, the ghost wave function, and the fermion mass renormalisation. Vertex renormalisation must also be addressed, and due to the gauge invariance, the coupling for each vertex is consistent. This results in four relationships for two couplings, g_0 (unrenormalised) and g_s (renormalised), as follows:

$$Z_2\sqrt{Z_3}g_0 = Z_1 g_s, \tag{2.3.30}$$

$$\tilde{Z}_3\sqrt{Z_3}g_0 = \tilde{Z}_1 g_s, \tag{2.3.31}$$

$$Z_3^{3/2} g_0 = Z_{1,3} g_s, \tag{2.3.32}$$

$$Z_3^2 g_0^2 = Z_{1,4} g_s^2. \tag{2.3.33}$$

The couplings for the quark-gluon vertex, the gluon-ghost vertex, the three-gluon vertex, and the four-gluon vertex are described respectively. By standardising these equations under a single form, the Slavnov-Taylor identities are established, $\tilde{Z}_1/\tilde{Z}_3 = Z_1/Z_2 = Z_{1,3}/Z_3 = \sqrt{Z_{1,4}/Z_3}$. Which is a nonabelian generalisation of the Ward identity $Z_1 = Z_2$ in QED. These identities reveal the fundamental interrelations among the renormalisation constants and further emphasise the underlying symmetry principles guiding their formulation.

To extract the renormalised coupling from the relationships described, dimensional regularisation[18] is employed. Specifically focusing on the quark-gluon vertex relation and adding the subscript 's' to denote the strong interaction coupling:

$$\alpha_s(\mu^2)^\epsilon = \frac{Z_2^2}{Z_1^2} Z_3 \alpha_{s,0}. \tag{2.3.34}$$

In dimensional regularisation, UV divergences manifest as poles at $\epsilon = 0$. Consequently, the Z_i coefficients are represented as:

$$Z_i = 1 + \alpha_s \frac{1}{\epsilon} c_i + \text{other finite terms}, \tag{2.3.35}$$

where c_i denotes the coefficients associated with the divergent terms. By substituting Eqs. (2.3.34) and (2.3.35) into Eq. (2.3.14), the β function at first order in α_s with $Z_i \approx 1 + \alpha_s c_i/\epsilon$ is expressed as:

$$\beta(\alpha_s) = \frac{\partial \alpha_s}{\partial \ln \mu^2} = -\epsilon \alpha_{s,0}(\mu^2)^{-\epsilon}\left[1 - 2(Z_1 - 1) + 2(Z_2 - 1) + (Z_3 - 1)\right] = 2\alpha_s^2(c_1 - c_2 + \frac{1}{2}c_3). \tag{2.3.36}$$

The Feynman graphs contributing to c_1, c_2, and c_3 are one-loop graphs depicted in Fig. 2.2. Detailed calculations of these graphs can be found in Section 7.1.1 of Ref. [1], pages 95-98, particularly focusing on the fermion loop contribution calculated using Feynman gauge ($\xi = 1$). The results for the renormalisation constants Z_i are given by:

$$Z_1 = 1 - \frac{\alpha_s}{4\pi}\left(C_F + C_A\right), \tag{2.3.37}$$

$$Z_2 = 1 - \left(\frac{\alpha_s}{4\pi}\right) C_F, \tag{2.3.38}$$

$$Z_3 = 1 + \frac{\alpha_s}{4\pi}\left(\frac{5}{3}C_A - \frac{4}{3}N_f T_F\right), \tag{2.3.39}$$

---

[18] In dimensional regularisation, the space-time dimensions d are reduced to $d = 4 - 2\epsilon$ to manage the UV divergences, as the divergences vanish when $\epsilon > 0$. This method introduces the factor $(\mu^2)^\epsilon$, allowing calculations to be performed before taking the limit as $\epsilon \to 0$.

where $C_A = N = 3$, $C_F = (N^2-1)/2N = 4/3$, and $T_F = 1/2$ denote the color factors, and N_f is the number of quark flavours. These constants in Eqs. (2.3.37)-(2.3.39) lead to the coefficients c_i needed in Eq. (2.3.36), resulting in:

$$\begin{aligned}\beta(\alpha_s) &= 2\frac{\alpha_s^2}{4\pi}\left(-C_F - C_A + C_F - \frac{1}{2}\frac{5}{3}C_A + \frac{1}{2}\frac{4}{3}N_f T_F\right)\\ &= -\frac{\alpha_s^2}{4\pi}\left(\frac{11}{3}C_A + \frac{4}{3}N_f T_F\right) = -\frac{\alpha_s^2}{12\pi}\left(11N - 2N_f\right). \end{aligned} \tag{2.3.40}$$

This equation demonstrates that for $N_f < 11N/2$, the β function in nonabelian cases like QCD is negative at small coupling, indicative of asymptotic freedom:

$$\beta(\alpha_s) = -\beta_0 \alpha_s^2 + \mathcal{O}(\alpha_s^3), \tag{2.3.41}$$

where

$$\beta_0 = \frac{1}{12\pi}(11N - 2N_f). \tag{2.3.42}$$

In the Standard Model, where $N = 3$ and $N_f = 6$, the coefficient β_0 is negative, contrasting with QED where the β function is positive at the lowest order. This difference illustrates that while the electromagnetic coupling increases with energy, the strong coupling decreases, demonstrating QCD's property of asymptotic freedom. This behaviour is described using the β function, which quantifies how the coupling changes with the energy scale. For QCD, the coupling weakens as the energy increases or the distance decreases, as expressed by:

$$\beta(\alpha_s) = \frac{\partial \alpha_s}{\partial \ln \mu^2} \Rightarrow \alpha_s(q^2) = \frac{\alpha_s(\mu^2)}{1 + \beta_0 \alpha_s(\mu^2) \ln \frac{q^2}{\mu^2}}, \tag{2.3.43}$$

which clearly shows the logarithmic decrease in coupling with increasing energy scale q^2. Conversely, this formula predicts a large coupling at low q^2, a condition known as *infrared slavery*. The energy scale Λ_{QCD} is defined as the energy scale where the coupling becomes infinite[19]:

$$1 + \beta_0 \alpha_s(\mu^2) \ln \frac{\Lambda_{\text{QCD}}^2}{\mu^2} = 0, \tag{2.3.44}$$

yielding

$$\Lambda_{\text{QCD}}^2 = \mu^2 \exp\left(-\frac{1}{\beta_0 \alpha_s(\mu^2)}\right). \tag{2.3.45}$$

This might suggest a dependence of Λ_{QCD} on μ, yet it remains a physical and constant scale because it is the energy at which the strong coupling grows unbounded. This scale is also known as the 'Landau pole', typically denoted by Λ. For QCD and QED, the Landau pole is illustrated in Figure 2.3.

Equation (2.3.43) loses validity at the QCD scale, indicating the need for theoretical adjustments near the Landau pole. It is important to demonstrate that Λ_{QCD} and the coupling are indeed physical quantities, invariant under changes in the renormalisation scale. Suppose the renormalisation scale is transformed from μ to μ':

$$\mu^2 \to (\mu')^2 := \mu^2 e^t, \tag{2.3.46}$$

---

[19] This is, of course, not physical. It just implies that around this energy scale the coupling will be very large. It signifies that this theory, and subsequently perturbation theory, is not applicable in this energy region.

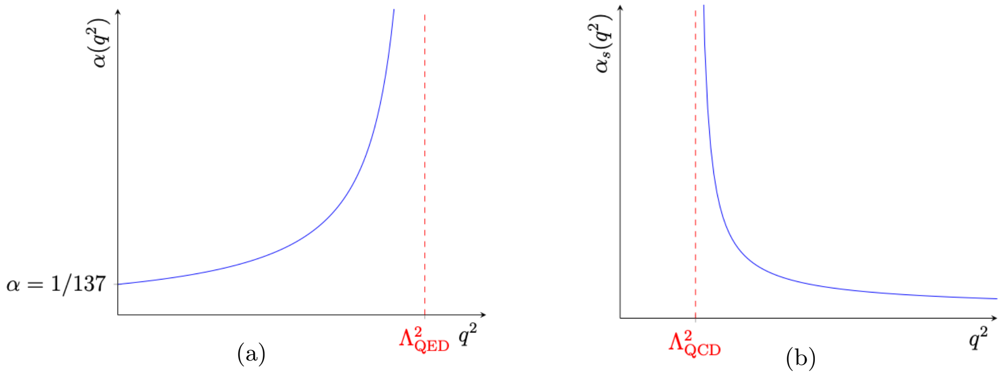

Figure 2.3: Illustration of the position of the Landau pole in (a) QED and (b) QCD.[1]

where t is a real number representing $\ln(\mu'^2/\mu^2)$. Under this transformation, the coupling changes scale but not form:

$$\alpha(\mu^2) \to \alpha(\mu'^2), \tag{2.3.47}$$

leading to

$$\alpha(\mu'^2) = \frac{\alpha_s(\mu^2)}{1 + \beta\alpha_s(\mu^2)t}, \tag{2.3.48}$$

and thus

$$\begin{aligned}
\Lambda^2_{\text{QCD}} = \mu^2 \exp\left(-\frac{1}{\beta_0\alpha_s(\mu^2)}\right) &\to \mu'^2 \exp\left(-\frac{1}{\beta_0\alpha_s(\mu'^2)}\right) && (2.3.49)\\
&= \mu^2 e^t \exp\left(-\frac{1+\beta_0\alpha_s(\mu^2)t}{\beta_0\alpha_s(\mu^2)}\right) && (2.3.50)\\
&= \mu^2 e^t \exp\left(-\frac{1}{\beta_0\alpha_s(\mu^2)} - t\right) && (2.3.51)\\
&= \mu^2 \exp\left(-\frac{1}{\beta_0\alpha_s(\mu^2)}\right) = \Lambda^2_{\text{QCD}}, && (2.3.52)
\end{aligned}$$

confirming that Λ_{QCD} is a genuine physical mass scale of QCD, independent of the chosen renormalisation scale μ. Experimentally, Λ_{QCD} is found to be approximately 200 MeV. The renormalisation-scale invariance of the strong coupling constant, α_s, can be demonstrated by expressing it in terms of Λ_{QCD} instead of μ, highlighting its independence from the renormalisation scale. Starting by rearranging Eq. (2.3.45) as:

$$\mu^2 = \Lambda^2_{\text{QCD}} \exp\left(\frac{1}{\beta_0\alpha_s(\mu^2)}\right). \tag{2.3.53}$$

This expression is substituted into the logarithmic term in Eq. (2.3.43),

$$\alpha_s(q^2) = \frac{\alpha_s(\mu^2)}{1 + \beta_0 \alpha_s(\mu^2) \left[\ln \frac{q^2}{\Lambda^2_{\text{QCD}}} - \ln \exp \left(\frac{1}{\beta_0 \alpha_s(\mu^2)} \right) \right]} \tag{2.3.54}$$

$$= \frac{\alpha_s(\mu^2)}{1 + \beta_0 \alpha_s(\mu^2) \ln \frac{q^2}{\Lambda^2_{\text{QCD}}}} = \frac{1}{\beta_0 \ln \frac{q^2}{\Lambda^2_{\text{QCD}}}}. \tag{2.3.55}$$

This formulation confirms that α_s is independent of the renormalisation scale, reinforcing the physicality of Λ_{QCD}. According to this model, the denominator becomes zero when q^2 equals Λ^2_{QCD}, indicating an undefined coupling at this scale.

The increasing coupling at decreasing energy scales presents challenges for this research. It includes simulations of high-energy experiments such as those conducted at the LHC, where protons collide at very high energies. In these simulations the strong interaction is adequately described at high energies by perturbation theory. However, as the energy decreases during the events, quarks produced in these collisions undergo hadronisation—they combine to form hadrons—occurring at much lower energy scales near Λ_{QCD}, where the current theoretical models become less precise. Understanding hadronisation, which typically occurs at energy scales comparable to the masses of resultant hadrons, remains an elusive goal due to its occurrence at these lower energies. As this process is crucial for interpreting collision outcomes, addressing these challenges is essential for advancing predictions in particle physics. This will be the central focus of the next chapter, with aim to develop methods to navigate these complexities effectively.

2.4 Hard Scattering Processes

In the introductory chapter, hadrons were viewed as composite particles bound by the strong interaction. In the context of QCD, these composites are specifically configurations of quarks. This perspective, established around the mid-20th century, categorises hadrons into two main types: mesons and baryons. Mesons consist of a quark and an antiquark pair, while baryons are made up of three quarks. This classification, though somewhat simplified, remains highly effective and is akin to Niels Bohr's atomic model: not entirely precise but sufficiently accurate for numerous practical applications. In this framework, quarks and antiquarks are bound together by the exchange of gluons.

However, a more detailed examination reveals a more complex picture than just a few quarks linked by gluons. This complexity is expected, especially considering what is understood about renormalisation and loop corrections in quantum field theories. Exchanged gluons can form loops before being absorbed by a quark or an antiquark, a process that can repeat multiple times. It is overly simplistic, though sometimes practically adequate, to view gluon exchange merely as one particle emitting and another absorbing. In reality, gluons are emitted spontaneously throughout the interaction space, forming loops incidentally absorbed by quarks or antiquarks. Consequently, hadrons are quite chaotic internally. Within a hadron, the constituent quarks, antiquarks, and gluons are collectively termed *partons*. Observing these partons at closer range, which corresponds to probing the hadron at higher energies or shorter distances, reveals the quantum effects more distinctly, and a greater number of partons become detectable. Thus, the simple model of a hadron containing just three quarks, or a quark-antiquark pair, is somewhat misleading. In reality, there are numerous transient quarks and antiquarks flying around; although they are temporary, their abundance means that, at any given moment, a hadron contains effectively more than three quarks for a baryon or a pair for a meson. These transient particles are distinguished from the more stable constituents: the permanent, structural partons are called *valence partons*, whereas the transient ones are referred to as *sea partons*. At lower energies, the influence of sea partons is negligible. However, in high-energy collisions, such as those studied in particle accelerators, both sea quarks and gluons significantly affect the outcomes, necessitating a description that accounts for all partons.

2.4.1 Factorisation

The method known as *factorisation* is pivotal in describing collision processes involving hadrons. It distinctly separates the long-distance (low-energy) dynamics from the short-distance (high-energy) dynamics. The initial high-energy interactions occur shortly after the collision, involving partons from one hadron and another particle, such as in electron-proton collisions, or partons from another hadron, as seen in proton-proton collisions. These short-distance dynamics are amenable to perturbative analysis due to the relatively weak QCD coupling at high energies. In contrast, the long-distance dynamics, which involve the hadronisation of the partons into observable hadrons, occur later and are not directly calculable using perturbation theory due to the strong QCD coupling at lower energies.

To illustrate factorisation, consider a less complex scenario than a proton-proton collision, such as deep inelastic scattering (DIS) of an electron on a proton, where the high-energy electron interacts with a proton's quark via the exchange of a photon or a weak boson. For simplicity, the exchange of a photon is assumed in subsequent explanation. The proton's initial momentum is denoted by p and the momentum of the exchanged photon by q.

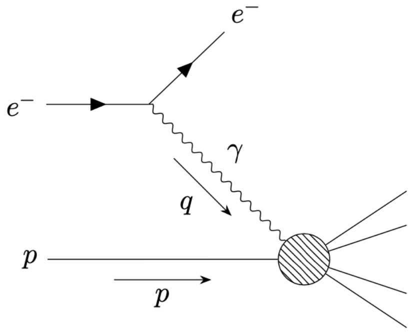

Figure 2.4: Feynman diagram for the DIS of an electron on a proton. The blob represents the proton as a complex composition of partons.[1]

The square of the momentum transfer is defined as:

$$-Q^2 := q^\mu q_\mu, \tag{2.4.1}$$

where $\sqrt{Q^2} \gg 1\text{fm}^{-1}$, indicating that Q^2 is significantly larger than Λ^2_{QCD}. This high momentum scale is referred to as the *hard scale*. Conversely, the term *soft* in high-energy physics often refers to lower energies or momenta. Furthermore, the variable x—also known as the Bjorken x—is defined as:

$$x = \frac{Q^2}{2p \cdot q}. \tag{2.4.2}$$

The interaction between the virtual photon and the quark occurs over a very short time scale, approximately $1/\sqrt{Q^2} \ll 1\text{fm}$. An important aspect to consider in hadronic processes is the continual interaction among quarks within the proton, which significantly influences their wave functions prior to their interaction with the incoming electron via the virtual photon. This sensitivity to longer-timescale interactions is a challenge unique to processes involving hadrons, as opposed to something like electron-positron scattering where long- and short-time interactions can be more easily separated using unitarity.

This complexity necessitates a nuanced approach to decouple the long-time dynamics from the short-time interactions, which is the essence of the factorisation method employed in QCD analyses. Factorisation not only enables the use of perturbation theory for calculating short-distance dynamics but also helps relate measurable hadronic quantities to calculable partonic interactions. The aim is to express the physical cross-section σ, as a function of both the hard momentum scales (denoted by Q) and the soft momentum scales (denoted by m[20]). This is achieved through a convolution formula:

$$\sigma(Q, m) = C(Q, \text{parton momenta} > \mu) \otimes f(\text{parton momenta} < \mu, m), \tag{2.4.3}$$

where C incorporates only the *hard* parton momenta, and f is dependent solely on *soft* parton momenta. Here, μ represents the *factorisation scale*, distinguishing between hard and soft momenta: momenta greater than μ are considered hard, while those less are deemed soft.

This representation offers significant advantages. Firstly, the dependence of σ on Q is confined to C, which is calculable using perturbative methods due to its reliance on high momenta. Secondly, since the overall physical cross-section σ must remain independent of the factorisation scale μ, any dependence of C on μ derived from f must precisely counteract that in f, ensuring that σ is invariant under changes in μ.

To facilitate these calculations, an appropriate reference frame needs to be selected. Due to the Lorentz invariance of the theory, the infinite-momentum frame can be chosen, where the proton's momentum along the z-axis is extremely large, and the electron's momentum is oriented oppositely in the negative z-direction. In this frame, the proton undergoes significant Lorentz contraction due to its high momentum:

The Lorentz contraction reduces the time $\Delta t_{scatter}$ it takes for the electron to traverse the proton. As the proton's momentum increases, this time diminishes further, while the internal parton interactions within the proton experience time dilation, extending their typical interaction time τ_{parton}. In the infinite-momentum frame, it holds that $\Delta t_{scatter} \ll \tau_{parton}$, indicating that during the electron's transit, it predominantly interacts with the valence quarks and any sea quarks or gluons that were already present. Resulting in the assumption that each parton will have a specific momentum during the interaction, characterised with a momentum fraction ξ of the total momentum of the proton.

Moreover, it needs to be considered that the parton-electron interaction mediated by a virtual photon assumes that Q^2 is large. There are primarily two interactions: the photon with one or more partons and the parton-parton interactions within the proton. Given that the interaction

---

[20] The m represents the hadronic mass scale

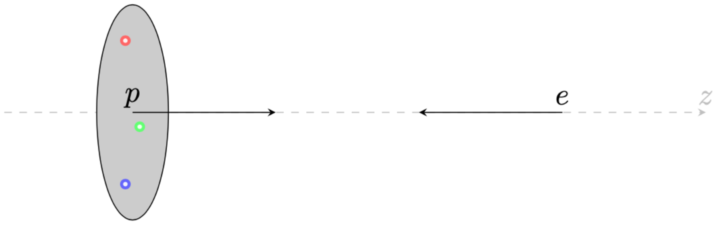

Figure 2.5: DIS electron-proton scattering in the infinite-momentum frame along the z axis. The elliptical shape represents the spatial distribution of the proton, highlighting the Lorentz contraction.[1]

time of the photon with a parton is brief compared to τ_{parton} and Q^2 is large, the distance Δl_γ that the photon traverses is minuscule:

$$\Delta l_\gamma \sim \frac{1}{\sqrt{Q^2}} \ll 1 \text{ fermi.} \tag{2.4.4}$$

In scenarios where the density of partons is sufficiently sparse, the photon typically interacts with just a single parton. Given that the photon-parton interaction occurs over a time scale $\Delta t_{scatter}$ that is much shorter than τ_{parton}, the typical timescale for interactions among partons, these processes are assumed to be temporally separable. This approximation enables the summation of probabilities rather than quantum mechanical amplitudes when calculating the total cross-section.

The cross-section for electron-proton DIS can therefore be expressed as a convolution of the probability (or cross-section) of electron (or photon) scattering off a parton, and the probability of finding that parton within the proton. The cross-section for electron scattering off a parton i is denoted as σ_{e-i}, where i indicates a specific parton type. This parton carries a fraction ξ of the total proton momentum, and σ_{e-i} encapsulates the hard component of the interaction.

The distribution of partons within the proton, representing the soft component, is characterised by parton distribution functions (PDFs), which describe the likelihood of finding a parton with a particular momentum fraction. The PDF for parton i is denoted by $f_{i/p}(\xi, \mu, m)$. The total cross-section for electron-proton DIS is as follows:

$$\sigma_{e-p}(x, Q, m) = \sum_i \int_x^1 d\xi \sigma_{e-i}\left(\frac{x}{\xi}, Q, \mu\right) f_{i/p}(\xi, \mu, m) + \mathcal{O}\left(\frac{\Lambda_{QCD}^2}{Q^2}\right). \tag{2.4.5}$$

This formula integrates over all possible momentum fractions, and sums over all partons that the electron can possibly interact with. m represents the typical interaction scale among partons within the proton. The auxiliary mass scale μ defines what scales are considered hard or soft, it only appears on the right-hand side. For notational simplicity, the interaction scale m will not be shown explicitly in further derivations.

To provide more detail, the differential cross-section is expressed in terms of dimensionless structure functions[21] F_L and F_T, respectively for longitudinally and transversely polarised

---

[21] A structure function is a probability density function that characterises an interaction without having to deal with all the underlying physics.

virtual photons:

$$\frac{d^2\sigma}{dx\,dQ^2} = \frac{4\pi\alpha^2}{xQ^4}\left(\left(1-y+\frac{y^2}{2}\right)F_2(x,Q^2) - \frac{y^2}{2}F_L(x,Q^2)\right), \tag{2.4.6}$$

where

$$F_2 = F_L + F_T \quad \text{and} \quad y = \frac{Q^2}{xs}, \tag{2.4.7}$$

with s being the square of the centre-of-mass energy. It's important to highlight that an expression akin to the one for the cross-section exists for any *fully inclusive*[22] hard-scattering observable reliant on a hard mass scale Q. For instance, the structure functions F_L and F_2 can be described as:

$$F_n(x,Q^2) = \sum_i \int_x^1 \frac{d\xi}{\xi} C_{ni}\left(\frac{x}{\xi}, \alpha_s(\mu^2), \frac{Q^2}{\mu^2}\right) f_i(\xi,\mu^2) + \mathcal{O}\left(\frac{\Lambda^2_{\mathrm{QCD}}}{Q^2}\right), \tag{2.4.8}$$

where the f_i are universal PDFs that are not perturbatively calculable, and C_{ni} are the coefficient functions computable in perturbation theory as power series in the strong coupling constant α_s as follows:

$$C_{ni}\left(\frac{x}{\xi}, \alpha_s(\mu^2), \frac{Q^2}{\mu^2}\right) = \sum_k C^{(k)}_{ni}\left(\frac{x}{\xi}, \frac{Q^2}{\mu^2}\right)\alpha_s^k(\mu^2), \tag{2.4.9}$$

Mellin transformations facilitate the conversion of convolution integrals into products, greatly simplifying the computation of structure functions like F_n in DIS. The Nth Mellin moment of a function G, represented by $G_N(\mu^2)$, is defined by:

$$G_N(\mu^2) = \int_0^1 d\zeta \zeta^{N-1} G(\zeta,\mu^2), \tag{2.4.10}$$

Applying this to the structure function F_n, its Mellin transformed counterpart is defined as $F_{n,N}$:

$$F_{n,N}(Q^2) = \sum_i C_{ni,N}\left(\alpha_s(\mu^2), \frac{Q^2}{\mu^2}\right) f_{i,N}(\mu^2), \tag{2.4.11}$$

where $C_{ni,N}$ and $f_{i,N}$ are the Mellin transforms of the coefficient functions and parton distribution functions, respectively. The transformation of F_n via Mellin moments proceeds as:

$$\begin{aligned} F_{n,N}(Q^2) &= \int_0^1 dx\, x^{N-1} F_n(x,Q^2) && (2.4.12)\\ &= \int_0^1 dx\, x^{N-1} \sum_i \int_x^1 d\xi C_{ni}\left(\frac{x}{\xi}, \alpha_s(\mu^2), \frac{Q^2}{\mu^2}\right) f_i(\xi,\mu^2) && (2.4.13)\\ &= \sum_i \int_0^1 dx \int_x^1 d\xi\, x^{N-1} C_{ni}\left(\frac{x}{\xi}, \alpha_s(\mu^2), \frac{Q^2}{\mu^2}\right) f_i(\xi,\mu^2). && (2.4.14) \end{aligned}$$

---

[22] This term will become more clear in the section about Drell-Yan. For now it is enough to understand that it means that you sum over all possible final states, without making distinctions.

which, after rearranging the integration order and performing a substitution $x' = x/\xi$, simplifies to:

$$\begin{aligned} F_{n,N}(Q^2) &= \sum_i \int_0^1 dx \int_x^1 d\xi \, x^{N-1} C_{ni}\left(\frac{x}{\xi}, \alpha_s(\mu^2), \frac{Q^2}{\mu^2}\right) f_i(\xi, \mu^2) && (2.4.15) \\ &= \sum_i \int_0^1 d\xi \int_0^\xi dx \, x^{N-1} C_{ni}\left(\frac{x}{\xi}, \alpha_s(\mu^2), \frac{Q^2}{\mu^2}\right) f_i(\xi, \mu^2) && (2.4.16) \\ &= \sum_i \int_0^1 d\xi \, \xi^{N-1} f_i(\xi, \mu^2) \int_0^1 dx' \, (x')^{N-1} C_{ni}\left(x', \alpha_s(\mu^2), \frac{Q^2}{\mu^2}\right) && (2.4.17) \\ &= \sum_i C_{ni,N}\left(\alpha_s(\mu^2), \frac{Q^2}{\mu^2}\right) f_{i,N}(\mu^2). && (2.4.18) \end{aligned}$$

Here, the dependence on ξ and x' in $C_{ni,N}$ and $f_{i,N}$ is removed by integrating over these variables.

This formalism allows expressing F_n, or any hard-scattering observable that depends on a hard momentum scale Q, in terms of simpler, product-based expressions suitable for computational analyses. Furthermore, it makes it possible to derive the Dokshitzer-Gribov-Lipatov-Altarelli-Parisi (DGLAP) evolution equations. These equations form the theoretical basis for Monte Carlo simulations used in predicting the outcomes of high-energy particle collisions.

2.4.2 Evolution Equations

The DGLAP equations are a specific set of RGEs where the dynamic variables are PDFs, as those discussed in Section 2.3.1. These equations model how PDFs evolve with changes in the mass scale, a critical aspect in describing parton dynamics up to the point of collision in high-energy interactions. Starting from a known PDF at a certain mass scale, DGLAP equations enable predictions of PDF behaviour at any other scale, where the internal complexity of hadrons becomes progressively detailed at higher energies.

DGLAP equations incorporate 'splitting functions', which quantify the likelihood that a parton observed at a lower energy scale will manifest as multiple partons at a higher energy scale. These functions are key to understanding both the emergence of new partons due to energy input and the decay of a parton into multiple lower-energy partons.

To derive the DGLAP equations, the approach used for deriving the RGEs is extended. Given that Eq. (2.4.8) remains invariant with respect to the scale μ, it is inferred that

$$\frac{d}{d\ln\mu^2} F_{n,N}(Q^2) = 0. \qquad (2.4.19)$$

For simplicity[23], the utilisation of the Mellin transform version of this equation from Eq. (2.4.11) results in:

$$\frac{dC_{n,N}}{d(\ln\mu^2)} f_N + C_{n,N} \frac{df_N}{d(\ln\mu^2)} = 0. \qquad (2.4.20)$$

Dividing through by the product $f_N C_{n,N}$ and applying the chain rule:

$$\frac{d(\ln C_{n,N})}{d(\ln\mu^2)} + \frac{d(\ln f_N)}{d(\ln\mu^2)} = 0. \qquad (2.4.21)$$

---

[23] The flavour index is also left out for simplicity.

By solving via separation of variables, the components are found to sum to zero independently:

$$\frac{d(\ln f_N)}{d(\ln \mu^2)} = \gamma_N = -\frac{d(\ln C_{n,N})}{d(\ln \mu^2)}, \tag{2.4.22}$$

where γ_N is a function computable via perturbation theory in terms of the strong coupling constant α_s:

$$\gamma_N(\alpha_s(\mu^2)) = \sum_{k=1}^{\infty} b_N^{(k)} \alpha_s^k(\mu^2). \tag{2.4.23}$$

Equation (2.4.22) enables a perturbative determination of the scale dependence of the PDFs, f_N, despite these functions not being directly computable through perturbation theory. The evolution equation for f_N are resolved from an initial scale μ_0^2 to any scale μ^2, giving:

$$f_N(\mu^2) = f_N(\mu_0^2) \exp\left(\int_{\ln \mu_0^2}^{\ln \mu^2} \gamma_N(\alpha_s(\mu'^2)) d(\ln \mu'^2)\right) \tag{2.4.24}$$

$$= f_N(\mu_0^2) \exp\left(\int_{\mu_0^2}^{\mu^2} \frac{\gamma_N(\alpha_s(\mu'^2))}{\mu'^2} d\mu'^2\right). \tag{2.4.25}$$

This approach, analogously to Eq. (2.3.22), demonstrates the violation of scaling in PDFs. The naming of this gamma function is not random, it is analogous to the anomalous dimension from Section 2.3.1.

Transitioning back from Mellin-moment space to Bjorken-x space involves performing an inverse Mellin transformation. The evolution equations then appear as follows[24]:

$$\frac{df_i(x,\mu^2)}{d(\ln \mu^2)} = \sum_j \int_x^1 \frac{d\xi}{\xi} P_{ij}\left(\frac{x}{\xi}, \alpha_s(\mu^2)\right) f_j(\xi, \mu^2), \tag{2.4.26}$$

where P_{ij} are the DGLAP splitting functions derived from the generalised anomalous dimensions $\gamma_{ij,N}$:

$$\gamma_{ij,N}(\alpha_s(\mu'^2)) = \int_0^1 dz\, z^{N-1} P_{ij}\left(z, \alpha_s(\mu^2)\right), \tag{2.4.27}$$

implying that P_{ij} corresponds to the inverse Mellin transform of $\gamma_{ij,N}$. To simplify the notation and calculations, PDFs are often presented in a momentum-weighted form, $\tilde{f}_i(x,\mu^2) = x f_i(x,\mu^2)$. Using this definition, the evolution equations for these functions are expressed as:

$$\frac{d\tilde{f}_i(x,\mu^2)}{d(\ln \mu^2)} = \sum_j \int_x^1 dz P_{ij}(z, \alpha_s(\mu^2)) \tilde{f}_j\left(\frac{x}{z}, \mu^2\right). \tag{2.4.28}$$

The evolution equations (2.4.26) or (2.4.28) are referred to as DGLAP evolution equations. Note that the energy scale μ in the strong coupling $\alpha_s(\mu^2)$ does not need to be the same as the factorisation scale μ in the PDF, in principle these can be different scales. In the section about the Drell-Yan process this will be written explicitly. These equations are powerful because the

---

[24] Here, the dependence on parton flavours is reintroduced.

splitting functions P_{ij} can be deduced using QCD perturbation theory and expressed as power series expansions in α_s:

$$P_{ij}(\alpha_s, z) = \sum_{n=1}^{\infty} \left(\frac{\alpha_s}{2\pi}\right)^n P_{ij}^{(n-1)}(z). \tag{2.4.29}$$

The leading-order (LO) splitting functions $P_{ij}^{(0)}$ illustrate the probability of a parton of type j with momentum fraction x_j emitting another parton and continuing as a parton of type i with momentum fraction x_i. The momentum fraction if the emitted parton is $x_j - x_i = x_j(1-z)$, or $z = x_i/x_j$. These splitting functions embody fundamental interactions between partons, where the specific parton type can be a gluon, quark, or antiquark. Charge conservation rules out transitions, namely: $P_{\bar{q}q}^{(0)}(z) = P_{q\bar{q}}^{(0)}(z) = 0$. This indicates that certain processes, such as a quark turning into an antiquark (or vice versa) does not occur through gluon emission, due to the conservation of electric charge and flavour (as can be seen Appendix A.1). It is important to note this only counts for LO splitting functions[25].

For other LO splitting functions, there is a symmetry between quarks and antiquarks, since gluons interact identically with both. Thus:

$$P_{gq_j}^{(0)}(z) = P_{g\bar{q}_j}^{(0)}(z), \tag{2.4.30}$$

$$P_{q_i g}^{(0)}(z) = P_{\bar{q}_i g}^{(0)}(z), \tag{2.4.31}$$

$$P_{q_i q_j}^{(0)}(z) = P_{\bar{q}_i \bar{q}_j}^{(0)}(z). \tag{2.4.32}$$

The graphical representations for these splitting processes are schematically depicted in Fig. 2.6. In this figure, p is the momentum of the hadron composed of the partons.

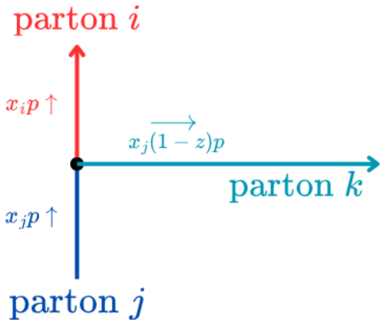

Figure 2.6: Schematic representation of a parton splitting process.

2.4.3 Drell-Yan Process

This thesis delves into the theory of proton-proton collisions, see Fig. 2.7 for an illustration of such a process. Consider two colliding hadrons A and B at a centre-of-mass energy $\sqrt{s}$, a parton from each hadron participates in the hard scattering process. The momentum-weighted

---

[25] Only higher-order processes can lead to flavour transitions. Diagrams representing these splittings are detailed in Appendix A.2, each correlating to a specific nonzero lowest order splitting function.

PDF for parton a from hadron A is represented by $\tilde{f}_{a/A}$, and similarly, $\tilde{f}_{b/B}$ for parton b from hadron B. The hard-scattering function H_{ab} models the interaction between these partons, resulting in various possible final states, such as hadronic jets or lepton pairs. If this process leads to the production of a Z-boson or a virtual photon, which subsequently decays into a lepton-antilepton pair, this is called the Drell-Yan process. The rest of this thesis will delve into this process.

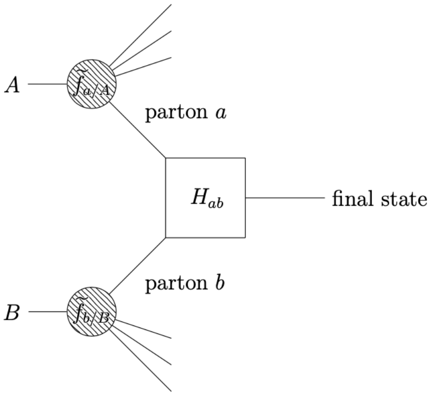

Figure 2.7: Illustration of the Drell-Yan process in a hadron-hadron collision.

Due to the involvement of two hadrons, the factorisation formula for this process is more complex than that for DIS, it now involves two PDFs, one for each hadron. If the hard scale is denoted by Q, the total cross-section for this process can be expressed as:

$$\sigma(s,Q^2)=\sum_{a,b}\int d\xi_1\int d\xi_2\tilde{f}_{a/A}(\xi_1,\mu_F^2)\tilde{f}_{b/B}(\xi_2,\mu_F^2)H_{ab}(\xi_1\xi_2 s,Q^2,\alpha_s(\mu_R^2),\mu_F^2)+\mathcal{O}\left(\frac{\Lambda_{\text{QCD}}^2}{Q^2}\right). \tag{2.4.33}$$

This equation introduces μ_F as the factorisation scale and μ_R as the renormalisation scale. They are by definition not the same, however, they are often assumed to be equal in practice. The PDFs are universal and can be determined from simpler processes like DIS, facilitating their use in these hadron-hadron collisions. The cross-section that was just described refers to an *inclusive* Drell-Yan cross-section, this is where the process of parton a + parton b goes to $l\bar{l}+all\ final\ states$. So *inclusive* means that all final states are taken into account in the calculation. On the other hand, *exclusive* Drell-Yan cross-sections are more restrictive and specify certain characteristics of the final states. For example, $l\bar{l}+2\ jets$, here $+all\ final\ states$ is left behind, signifying the restrictive nature of an exclusive cross section. The inclusive approach depends solely on the parton distributions in the hadrons and the hard interaction between the partons a and b, independent of the specific final states or the interactions the partons a and b may have had inside their respective hadrons before the collision. While exclusive cross-sections require detailed descriptions of the final states and the partons' pre-collision evolution, inclusive cross-sections, such as those described by Eq. (2.4.33), do not. The latter simplifies the theoretical analysis and computational modelling of high-energy particle collisions, focusing on the essential dynamics of the interactions.

Summary

Chapter 2, titled "Basic Elements of Quantum Chromodynamics," lays the theoretical groundwork for understanding proton-proton collisions. It starts with an overview of Quantum Chromodynamics (QCD), explaining it as a non-Abelian gauge theory based on the $SU(3)$ symmetry group, which describes the strong interactions between quarks and gluons. The chapter details the gauge principle, emphasising its role in ensuring local gauge invariance, and introduces the QCD Lagrangian to describe the dynamics of quarks and gluons. The quantisation of gauge field theories is explored, highlighting differences between Abelian and non-Abelian cases. Key concepts such as renormalisation, the renormalisation group, and the running of the coupling constant are discussed, illustrating how the strong force behaves differently at various energy scales. The chapter also covers hard scattering processes, factorisation, evolution equations, and the Drell-Yan process, all of which are crucial for analysing hadron collisions and understanding the intrinsic transverse momentum distributions of partons within hadrons. This knowledge is essential for the thesis's focus on the inclusive Drell-Yan differential cross sections in the transverse momentum of the lepton pair and their behaviour across different center-of-mass energies in proton-proton collisions.

Next Chapter

The next chapter builds on the foundational concepts introduced in this chapter by applying the theoretical framework of Quantum Chromodynamics to a practical computational method, called Parton Branching. It starts with the reformulation of the renormalisation group evolution equations, specifically the DGLAP equations for PDFs, and allows to, both recast them as an iterative Monte Carlo problem, and to treat by analogous methods the evolution of transverse momentum dependent (TMD) parton distributions that take transverse momentum into account.

Chapter 3

Parton Branching Method

The Parton Branching (PB) method allows the description of the QCD evolution of parton distribution functions (PDFs) and transverse momentum dependent (TMD) distributions. The method will be introduced by first reformulating the renormalisation group evolution equations for PDFs. These are the DGLAP equations and they are explored in Section 2.4.2. Using the unitarity formulation approach, the numerical solutions of the DGLAP equations are enabled through an iterative Monte Carlo process by categorising branchings as resolvable and non-resolvable and utilising Sudakov form factors. These form factors are crucial for modelling the evolution between scales without a resolvable branching. In this context, 'branching' refers to the division of one parton into two, as governed by the splitting functions discussed in Section 2.4.2 (detailed in Appendix A.2). A *resolvable branching* is simply a parton splitting that becomes observable when moving to a higher energy scale. Conversely, a *non-resolvable branching* is a parton splitting that can't be observed. In other words, it's a branching event that does not significantly alter the measurable characteristics of the partons beyond the resolution limits of the theory.

The first three sections of the chapter are devoted to the case of PDFs. The last two sections of the chapter are devoted to TMDs. We follow closely the approach in [11].

3.1 Unitarity Approach to the DGLAP Equations

The DGLAP equations, with momentum-weighted PDFs are:

$$\frac{\partial \tilde{f}_a(x,\mu^2)}{\partial \ln \mu^2} = \sum_b \int_x^1 dz P_{ab}(\alpha_s, z) \tilde{f}_b\left(\frac{x}{z}, \mu^2\right). \tag{3.1.1}$$

The unitarity approach moves from the observation that, if a finite resolution is applied in the transverse distance between partons, by energy and momentum conservation, the ability to resolve partons with momentum fractions z very close to $z = 1$ is restricted. Therefore, a cutoff z_M is introduced such that $z > z_M$ and $1 - z_M \approx \mathcal{O}(\Lambda_{\mathrm{QCD}}/\mu)$, where μ relates to the hard-scattering scale. Omitting these non-resolvable emissions can lead to unitarity violations, which the parton branching method addresses by incorporating no-branching probabilities (Sudakov form factors) and real-emission probabilities into the evolution equations. The introduction of the resolution scale z_M is formalised in Section 3.2.

The framework is established by beginning with decomposing the splitting functions $P_{ab}(\alpha_s, z)$:

$$P_{ab}(\alpha_s, z) = D_{ab}(\alpha_s)\delta(1-z) + K_{ab}(\alpha_s)\frac{1}{(1-z)_+} + R_{ab}(\alpha_s, z), \tag{3.1.2}$$

where the plus-distribution $1/(1-z)_+$ is defined through its action on any test function ϕ:

$$\int_0^1 \frac{1}{(1-z)_+}\phi(z)\, dz = \int_0^1 \frac{\phi(z) - \phi(1)}{1-z}\, dz. \tag{3.1.3}$$

Equation (3.1.2) delineates the singular behaviour of the splitting functions $P_{ab}(\alpha_s, z)$ as z approaches 1, categorising them into three distinct types: the $\delta(1-z)$ distribution, the $1/(1-z)_+$ distribution, and the remaining terms in $R_{ab}(\alpha_s, z)$, which include logarithmic contributions in $\ln(1-z)$ and analytic terms as $z \to 1$. The components $\delta(1-z)$ and $1/(1-z)_+$ in the splitting functions are flavour-diagonal,

$$D_{ab}(\alpha_s) = \delta_{ab} d_a(\alpha_s), \quad K_{ab}(\alpha_s) = \delta_{ab} k_a(\alpha_s), \tag{3.1.4}$$

assuming no summation over repeated indices. The functions d_a and k_a, along with the functions R_{ab} in Eq. (3.1.2) can be expanded in perturbation series:

$$d_a(\alpha_s) = \sum_{n=1}^{\infty} \left(\frac{\alpha_s}{2\pi}\right)^n d_a^{(n-1)}, \tag{3.1.5}$$

$$k_a(\alpha_s) = \sum_{n=1}^{\infty} \left(\frac{\alpha_s}{2\pi}\right)^n k_a^{(n-1)}, \tag{3.1.6}$$

$$R_{ab}(\alpha_s, z) = \sum_{n=1}^{\infty} \left(\frac{\alpha_s}{2\pi}\right)^n R_{ab}^{(n-1)}(z). \tag{3.1.7}$$

The analytical approach of this section is solely based on the decomposition of Eq. (3.1.2) and remains valid on all orders of α_s. In practical scenarios, a specific truncation from Eqs. (3.1.5–3.1.7) is employed, with numerical analyses in this thesis relying on this expansion up to next-to-leading order (NLO), or $n = 2$.

The symmetries of charge conjugation and $SU(N_f)$ flavour enforce that the splitting functions P_{ab} adhere to certain relationships at all orders:

$$P_{q_i g} = P_{\bar{q}_i g} \equiv P_{qg}, \quad P_{g q_i} = P_{g \bar{q}_i} \equiv P_{gq}, \tag{3.1.8}$$

$$P_{q_i q_j} = P_{\bar{q}_i \bar{q}_j} \equiv P_{qq}^{NS}\delta_{ij} + P_{qq}^{S}, \quad P_{q_i \bar{q}_j} = P_{\bar{q}_i q_j} \equiv P_{q\bar{q}}^{NS}\delta_{ij} + P_{q\bar{q}}^{S}, \tag{3.1.9}$$

where the notations NS and S represent non-singlet and singlet, respectively. Consequently, P_{ab} features three independent quark-gluon or gluon-gluon components: P_{qg}, P_{gq} and P_{gg}, and four quark-quark components: the non-singlet components P_{qq}^{NS} and $P_{q\bar{q}}^{NS}$, alongside the singlet components P_{qq}^{S} and $P_{q\bar{q}}^{S}$. Alternatively, the quark-quark components can be viewed as the three combinations that diagonalise the evolution of non-singlet distributions, plus one governing the evolution of the singlet quark distribution in conjunction with gluons.

At the one-loop level, it is observed that $P_{qq}^{NS} = P_{qq}^{S} = P_{q\bar{q}}^{S} = 0$, signifying that all quark-quark components are equivalent at this order. The coefficients for the perturbative expansions outlined in Eqs. (3.1.5–3.1.7) (d_a, k_a, and R_{ab}) are detailed in [18–20] and are provided as follows:

$$d_q^{(0)} = \frac{3}{2}C_F, \quad d_g^{(0)} = \frac{11}{6}C_A - \frac{2}{3}T_R N_f, \tag{3.1.10}$$

$$k_q^{(0)} = 2C_F, \quad k_g^{(0)} = 2C_A, \tag{3.1.11}$$

$$R_{gg}^{(0)}(z) = 2C_A\left[\frac{1-z}{z} + z(1-z) - 1\right], \tag{3.1.12}$$

$$R_{gq_i}^{(0)}(z) = R_{g\bar{q}_i}^{(0)}(z) = C_F\frac{1+(1-z)^2}{z}, \tag{3.1.13}$$

$$R_{q_ig}^{(0)}(z) = R_{\bar{q}_ig}^{(0)}(z) = T_R\left[z^2 + (1-z)^2\right], \tag{3.1.14}$$

$$R_{q_iq_j}^{(0)}(z) = R_{\bar{q}_i\bar{q}_j}^{(0)}(z) = -C_F(1+z)\delta_{ij}, \tag{3.1.15}$$

$$R_{q_i\bar{q}_j}^{(0)}(z) = R_{\bar{q}_iq_j}^{(0)}(z) = 0, \tag{3.1.16}$$

where the $SU(N_c = 3)$ colour factors are specified as (for colour algebra, see Ref. [1] on p 65-68)

$$C_A = N_c, \quad C_F = \frac{N_c^2 - 1}{2N_c}, \quad \mathrm{Tr}(t^k t^m) = \delta^{km} T_R = \frac{1}{2}\delta^{km}. \tag{3.1.17}$$

At the two-loop level, the coefficients d_a, k_a, and R_{ab} begin to exhibit dependencies on the chosen renormalisation scheme. Following Ref. [11], the $\overline{\text{MS}}$ scheme[1] is adopted. The detailed coefficients can be found in [21, 22]. At this level, P_{qq}^{NS}, P_{qq}^{S}, and $P_{q\bar{q}}^{S}$ become non-zero, thus lifting the previous degeneracy, although $P_{qq}^{S} = P_{q\bar{q}}^{S}$ still holds. The two-loop coefficients for d_a and k_a are provided by

$$d_q^{(1)} = C_F^2\left(\frac{3}{8} - \frac{\pi^2}{2} + 6\zeta(3)\right) + C_F C_A\left(\frac{17}{24} + \frac{11\pi^2}{18} - 3\zeta(3)\right) - C_F T_R N_f\left(\frac{1}{6} + \frac{2\pi^2}{9}\right), \tag{3.1.18}$$

$$d_g^{(1)} = C_A^2\left(\frac{8}{3} + 3\zeta(3)\right) - \frac{4}{3}C_A T_R N_f - C_F T_R N_f, \tag{3.1.19}$$

where ζ denotes the Riemann zeta function, and

$$k_q^{(1)} = 2C_F\Gamma, \quad k_g^{(1)} = 2C_A\Gamma, \tag{3.1.20}$$

$$\text{with } \Gamma = C_A\left(\frac{67}{18} - \frac{\pi^2}{6}\right) - T_R N_f\frac{10}{9}.$$

The detailed expressions for the two-loop R_{ab} coefficients are more extensive and are provided in Appendix A.3. As previously mentioned, these formulations through two loops will be used for the NLO numerical calculations in this thesis.

3.2 Nonresolvable and Resolvable Branchings

This section introduces the soft-gluon resolution parameter [12] into the evolution equations (3.1.1), this parameter is denoted by z_M. This is achieved by dividing the integration on the

---

[1] This is the modified minimal subtraction scheme, which incorporates both the divergent parts and a universal constant that appear in Feynman diagram evaluations into the counter-terms.

right-hand side into two regions: the resolvable region ($z < z_M$) and the non-resolvable region ($z_M < z$), where $1 - z_M \sim \mathcal{O}(\Lambda_{\text{QCD}}/\mu)$. Then the decomposition (3.1.2) is applied within each region, including terms to $(1 - z_M)^0$ while the contributions of order $\mathcal{O}(1 - z_M)^n$ for $n \geq 1$ are omitted.

The contribution from the K_{ab} term as z approaches 1, utilising the plus-distribution from Eq. (3.1.3), is given by:

$$\begin{aligned}\sum_b \int_x^1 dz \frac{K_{ab}(\alpha_s)}{(1-z)_+} \tilde{f}_b\left(\frac{x}{z}, \mu^2\right) &= \sum_b \int_x^1 dz \frac{K_{ab}(\alpha_s)}{1-z} \tilde{f}_b\left(\frac{x}{z}, \mu^2\right) \\ &- \sum_b \int_0^1 dz \frac{K_{ab}(\alpha_s)}{1-z} \tilde{f}_b(x, \mu^2).\end{aligned} \tag{3.2.1}$$

For the non-resolvable region $z \in]z_M, 1[$ the momentum-weighted PDF is expanded as:

$$\tilde{f}_b\left(\frac{x}{z}, \mu^2\right) = \tilde{f}_b(x, \mu^2) + (1-z) \frac{\partial \tilde{f}_b}{\partial \ln x}(x, \mu^2) + \mathcal{O}(1-z)^2. \tag{3.2.2}$$

Using Eq. (3.2.2), the Eq. (3.2.1) can be rewritten as:

$$\begin{aligned}\sum_b \int_x^1 dz \frac{K_{ab}(\alpha_s)}{(1-z)_+} \tilde{f}_b\left(\frac{x}{z}, \mu^2\right) &= \sum_b \int_x^{z_M} dz \frac{K_{ab}(\alpha_s)}{1-z} \tilde{f}_b\left(\frac{x}{z}, \mu^2\right) \\ &- \sum_b \int_0^{z_M} dz \frac{K_{ab}(\alpha_s)}{1-z} \tilde{f}_b(x, \mu^2).\end{aligned} \tag{3.2.3}$$

Next, the contributions from the other terms in Eq. (3.1.2), D_{ab} and R_{ab}, are considered. The contribution from R_{ab} is combined with the first term on the right-hand side of Eq. (3.2.3) to add a factor proportional to $\tilde{f}_b(x/z, \mu^2)$ to the evolution. The contribution from D_{ab}, using the $\delta(1-z)$, is combined with the second term on the right-hand side of Eq. (3.2.3) to yield a factor proportional to $\tilde{f}_b(x, \mu^2)$.

Notably, R_{ab} has no power divergences of the form $(1-z)^{-n}$ and is at most logarithmic as z approaches 1, meaning integration over R_{ab} for $z > z_M$ results in $\mathcal{O}(1 - z_M)$ contributions:

$$\begin{aligned}\frac{\partial \tilde{f}_a(x, \mu^2)}{\partial \ln \mu^2} &= \sum_b \int_x^{z_M} dz \left(\frac{K_{ab}(\alpha_s)}{1-z} + R_{ab}(\alpha_s, z)\right) \tilde{f}_b\left(\frac{x}{z}, \mu^2\right) \\ &+ \sum_b \left(\int_x^1 D_{ab}(\alpha_s)\delta(1-z)dz - \int_0^{z_M} \frac{K_{ab}(\alpha_s)}{1-z} dz\right) \tilde{f}_b(x, \mu^2).\end{aligned} \tag{3.2.4}$$

The first line of this equation includes contributions from real parton emissions, while the second line includes contributions from virtual corrections. The kernels in the bracket of the first line are defined as real-emission branching probabilities $P^{(R)}_{ab}(\alpha_s, z)$:

$$P^{(R)}_{ab}(\alpha_s, z) = \frac{K_{ab}(\alpha_s)}{1-z} + R_{ab}(\alpha_s, z). \tag{3.2.5}$$

These real-emission branching probabilities $P^{(R)}_{ab}(\alpha_s, z)$ are derived from the splitting functions $P_{ab}(\alpha_s, z)$ in Eq. (3.1.2) by excluding the $\delta(1-z)$ terms and substituting the plus-distribution

$1/(1-z)_+$ with $1/(1-z)$. Thus, it can be reformulated as:

$$\frac{\partial \tilde{f}_a(x,\mu^2)}{\partial \ln \mu^2} = \sum_b \int_x^{z_M} dz P_{ab}^{(R)}(\alpha_s, z)\tilde{f}_b\left(\frac{x}{z},\mu^2\right) + \sum_b \left(\int_x^1 D_{ab}(\alpha_s)\delta(1-z)dz - \int_0^{z_M} \frac{K_{ab}(\alpha_s)}{1-z}dz\right)\tilde{f}_b(x,\mu^2). \tag{3.2.6}$$

The virtual terms in the second line of this equation are addressed by applying the momentum sum rule,

$$\sum_c \int_0^1 zP_{ca}(\alpha_s,z)\,dz = 0 \quad \text{(for any } a\text{)}. \tag{3.2.7}$$

Specifically, this rule is integrated into the evolution equations by subtracting the integral of the momentum sum from the expression in the curly brackets of the second line in Eq. (3.2.6). This rule allows a systematic replacement of the D-terms in Eq. (3.1.2) within the evolution equations with K-terms and R-terms.

Given the diagonal nature of D_{ab} and K_{ab} terms as outlined in Eq. (3.1.4), indices are rearranged and from Eq. (3.2.6) it is derived that:

$$\frac{\partial \tilde{f}_a(x,\mu^2)}{\partial \ln \mu^2} = \sum_b \int_x^{z_M} dz P_{ab}^{(R)}(\alpha_s, z)\tilde{f}_b\left(\frac{x}{z},\mu^2\right) + \sum_c \left(\int_x^1 D_{ca}(\alpha_s)\delta(1-z)\,dz - \int_0^{z_M} \frac{K_{ca}(\alpha_s)}{1-z}\,dz - \int_0^1 zP_{ca}(\alpha_s,z)\,dz\right)\tilde{f}_a(x,\mu^2). \tag{3.2.8}$$

Implementing the decomposition (3.1.2) for $P_{ca}(\alpha_s, z)$ in the last term of Eq. (3.2.8) reveals that the D_{ca} term cancels the first term in the curly brackets, whereas the R_{ca} term remains valid within $z < z_M$, up to order $\mathcal{O}(1-z_M)$. The K_{ca} term combines with the second term in the brackets to simplify the evolution equation:

$$\frac{\partial \tilde{f}_a(x,\mu^2)}{\partial \ln \mu^2} = \sum_b \int_x^{z_M} dz\, P_{ab}^{(R)}(\alpha_s, z)\tilde{f}_b\left(\frac{x}{z},\mu^2\right) - \sum_c \left(\int_0^{z_M} dz\, z\frac{K_{ca}(\alpha_s)}{1-z} + \int_0^{z_M} dz\, zR_{ca}(\alpha_s,z)\right)\tilde{f}_a(x,\mu^2). \tag{3.2.9}$$

By applying Eq. (3.2.5), the evolution equations (3.2.6) are expressed as:

$$\frac{\partial \tilde{f}_a(x,\mu^2)}{\partial \ln \mu^2} = \sum_b \left\{\int_x^{z_M} dz\, P_{ab}^{(R)}(\alpha_s, z)\tilde{f}_b\left(\frac{x}{z},\mu^2\right) - \int_0^{z_M} dz\, zP_{ba}^{(R)}(\alpha_s,z)\tilde{f}_a(x,\mu^2)\right\}. \tag{3.2.10}$$

Eq. (3.2.10) redefines the evolution dynamics of each parton a via the real-emission probabilities $P_{ab}^{(R)}$ and $P_{ba}^{(R)}$, and the resolution parameter z_M.

The Sudakov form factor $\Delta_a(z_M,\mu^2,\mu_0^2)$ is introduced because it is computationally advantageous as it can be used in a Monte Carlo procedure. This form factor represents the probability that parton a does not undergo branching between scales μ_0 and μ, given the resolution parameter z_M and it is defined as:

$$\Delta_a(z_M,\mu^2,\mu_0^2) = \exp\left(-\sum_b \int_{\mu_0^2}^{\mu^2} \frac{d\mu'^2}{\mu'^2} \int_0^{z_M} dz\, z P_{ba}^{(R)}(\alpha_s,z)\right). \tag{3.2.11}$$

Using this Sudakov factor and noting that:

$$\frac{\partial \Delta_a(z_M,\mu^2,\mu_0^2)}{\partial \ln \mu^2} = -\Delta_a(z_M,\mu^2,\mu_0^2) \sum_b \int_0^{z_M} dz\, z P_{ba}^{(R)}(\alpha_s,z). \tag{3.2.12}$$

Eq. (3.2.10) results in[2]

$$\frac{\partial \tilde{f}_a(x,\mu^2)}{\partial \ln \mu^2} = \sum_b \int_x^{z_M} dz\, P_{ab}^{(R)}(\alpha_s,z) \tilde{f}_b\left(\frac{x}{z},\mu^2\right) + \frac{1}{\Delta_a(\mu^2)} \frac{\partial \Delta_a(\mu^2)}{\partial \ln \mu^2} \tilde{f}_a(x,\mu^2). \tag{3.2.13}$$

Reformulating the evolution equation using real-emission probabilities $P_{ab}^{(R)}$ and Sudakov form factors, results in a similar the structure as in Eq. (3.1.1):

$$\frac{\partial}{\partial \ln \mu^2}\left(\frac{\tilde{f}_a(x,\mu^2)}{\Delta_a(\mu^2)}\right) = \sum_b \int_x^{z_M} dz\, P_{ab}^{(R)}(\alpha_s,z) \frac{\tilde{f}_b(x/z,\mu^2)}{\Delta_a(\mu^2)}. \tag{3.2.14}$$

The integration of this equation, while assuming $\Delta_a(\mu_0^2) = 1$, gives the following:

$$\begin{aligned} \tilde{f}_a(x,\mu^2) &= \Delta_a(\mu^2,\mu_0^2)\tilde{f}_a(x,\mu_0^2) \\ &+ \sum_b \int_{\mu_0^2}^{\mu^2} \frac{d\mu'^2}{\mu'^2} \frac{\Delta_a(\mu^2,\mu_0^2)}{\Delta_a(\mu'^2,\mu_0^2)} \int_x^{z_M} dz P_{ab}^{(R)}(\alpha_s(\mu'^2),z) \tilde{f}_b\left(\frac{x}{z},\mu'^2\right), \end{aligned} \tag{3.2.15}$$

where the energy scale arguments are explicitly stated for α_s and the Sudakov factor Δ_a. The argument z_M is not restored in the Sudakov factor, since it will not vary when going to higher steps in the iteration.

The introduction of the Sudakov form factor transforms the evolution equation into a type of integral equation reminiscent of the Fredholm equation:

$$f(t) = f_0(t) + \lambda \int_a^b K(t,y) f(y)\, dy, \tag{3.2.16}$$

which can be iteratively solved as an infinite series:

$$f(t) = \lim_{n\to\infty} \sum_{i=0}^{n} \lambda^i u_i(t), \tag{3.2.17}$$

---

[2] Where z_M and μ_0^2 are removed from the argument list for better readability

where the sequence is defined as follows:

$$u_0(t) = f_0(t), \tag{3.2.18}$$

$$u_1(t) = \int_a^b K(t,y) f_0(y)\, dy, \tag{3.2.19}$$

$$u_2(t) = \int_a^b \int_a^b K(t,y_1)K(y_1,y_2) f_0(y_2)\, dy_2\, dy_1, \tag{3.2.20}$$

$$\vdots$$

$$u_n(t) = \int_a^b \dots \int_a^b \int_a^b K(t,y_1)\cdots K(y_{n-1},y_n) f_0(y_n)\, dy_n \dots dy_2\, dy_1. \tag{3.2.21}$$

The splitting functions are positive definite for LO in α_s; however, this is does not hold at NLO. Despite the integrands potentially being negative at NLO, the integrals of the splitting functions, which contribute to the evolution kernels and Sudakov form factors, remain positive. This enables the application of a Monte Carlo method for solving the evolution equations, which will be used in the computer code for the simulations in this thesis. The next section will detail this iterative procedure.

3.3 The Iterative Procedure

The parton branching method, clarified by Equation (3.2.15), offers a systematic approach for evolving parton distributions from an initial scale μ_0 to a final scale μ. The first term in (3.2.15) can be intuitively understood. It involves the PDF at the initial scale μ_0, modulated by the Sudakov form factor up to scale μ. This term captures the scenario where a parton of type a evolves from μ_0 to μ without any intermediate emissions. This is given in the schematic **(a)** in Figure 3.1 and represents the first iteration in the evolution process.

The Fredholm nature of the equations result in the full PDF, denoted $\tilde{f}_a(x,\mu^2)$, being expressible as a convergent series comprising of contributions from each iterative step of the evolution:

$$\tilde{f}_a(x,\mu^2) = \sum_{i=0}^{\infty} \tilde{f}_a^{(i)}(x,\mu^2). \tag{3.3.1}$$

Here, the term $\tilde{f}_a^{(0)}(x,\mu^2)$ coming from Eq. (3.2.15), given by

$$\tilde{f}_a^{(0)}(x,\mu^2) = \Delta_a(\mu^2,\mu_0^2)\tilde{f}_a(x,\mu_0^2), \tag{3.3.2}$$

serves as an initial approximation of $\tilde{f}_a(x,\mu^2)$, approximating the PDF after the first step of the branching without any emissions. Subsequent terms can be derived by incorporating this result back into the iterative integral in Eq. (3.2.15), yielding the contribution from the next step:

$$\tilde{f}_a^{(1)}(x,\mu^2) = \sum_b \int_{\mu_0^2}^{\mu^2} \frac{d\mu'^2}{\mu'^2} \frac{\Delta_a(\mu'^2,\mu_0^2)}{\Delta_a(\mu^2,\mu_0^2)} \int_x^{z_M} dz P_{ab}^{(R)}(\alpha_s,z)\tilde{f}_b^{(0)}\left(\frac{x}{z},\mu'^2\right) \tag{3.3.3}$$

$$= \sum_b \int_{\mu_0^2}^{\mu^2} \frac{d\mu'^2}{\mu'^2} \frac{\Delta_a(\mu'^2,\mu_0^2)}{\Delta_a(\mu^2,\mu_0^2)} \int_x^{z_M} dz P_{ab}^{(R)}(\alpha_s,z)\Delta_b(\mu'^2,\mu_0^2)\tilde{f}_b\left(\frac{x}{z},\mu_0^2\right). \tag{3.3.4}$$

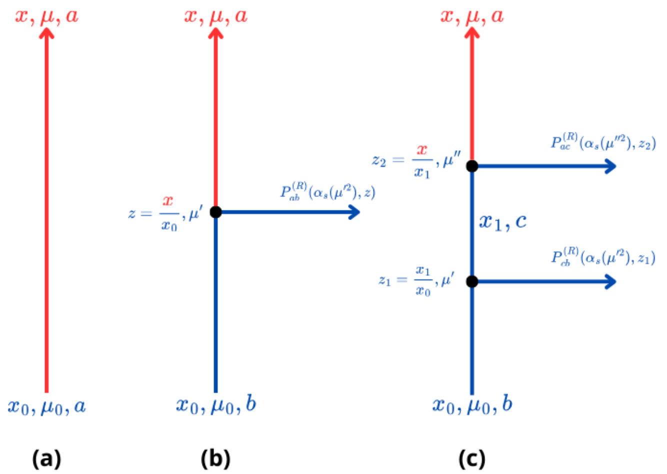

Figure 3.1: Illustration of the iteration process: a parton can evolve from scale μ_0 to scale μ without any branching (a), having one branching (b), or two branchings (c). It goes further on like this, also the relevant variables are indicated.

In this expression, $\tilde{f}_a^{(1)}(x, \mu^2)$ corresponds to the evolution of a parton type b into a parton type a, incorporating a branching at scale μ'. This represents an evolution involving an emission, as illustrated in schematic **(b)** in Fig. 3.1. The momentum fraction of the emitted parton is derived from $x_0 - x = (1 - z)x_0$, yielding $z = x/x_0$. The probability for the parton with flavour b to evolve from μ_0 to μ' without any resolvable branching is given by the Sudakov form factor $\Delta_b(\mu'^2)$, which results in an updated approximation to the full PDF:

$$\begin{aligned}\tilde{f}_a(x, \mu^2) &\approx \Delta_a(\mu^2, \mu_0^2)\tilde{f}_a(x, \mu_0^2) \\ &+ \sum_b \int_{\mu_0^2}^{\mu^2} \frac{d\mu'^2}{\mu'^2} \frac{\Delta_a(\mu^2, \mu_0^2)}{\Delta_a(\mu'^2, \mu_0^2)} \int_x^{z_M} dz P_{ab}^{(R)}(\alpha_s, z)\Delta_b(\mu'^2, \mu_0^2)\tilde{f}_b\left(\frac{x}{z}, \mu_0^2\right). \qquad (3.3.5)\end{aligned}$$

To incorporate the effects of a second branching, the previous needs to be repeated. The evolution model starts with a parton of flavour b and momentum fraction x_0 at scale μ_0. This parton evolves into a parton of flavour a with a reduced momentum fraction x at scale μ, undergoing two branchings in the process. Initially, at scale μ', the parton transitions to flavour c with momentum fraction x_1. The momentum fraction ratio $z_1 = x_1/x_0$ quantifies the momentum fraction carried by parton c relative to parton b. A subsequent branching at scale μ'' further modifies the parton c to flavour a. The corresponding momentum fraction ratio $z_2 = x/x_1$ delineates the transition. This detailed evolution is illustrated in schematic **(c)** of Fig. (3.1).

Considering the iterative nature of the branching, the second branching represents an additional modification to the initial branching. The function $\tilde{f}_a^{(1)}$ quantifies the PDF post-first branching. To compute $\tilde{f}_a^{(2)}$, appropriate energy scales and momentum fractions must be used. Specifically, the function arguments for $\tilde{f}_a^{(1)}$ are set as μ''^2 for the energy scale and $x_1 = x/z_2$

for the momentum fraction, reflecting the conditions post-second branching, illustrated as:

$$\tilde{f}_a^{(2)}(x,\mu^2) = \sum_c \int_{\mu_0^2}^{\mu^2} \frac{d\mu''^2}{\mu''^2} \frac{\Delta_a(\mu^2,\mu_0^2)}{\Delta_a(\mu''^2,\mu_0^2)} \int_x^{z_M} dz_2 P_{ac}^{(R)}(\alpha_s(\mu''^2),z_2)\tilde{f}_c^{(1)}\left(\frac{x}{z_2},\mu''^2\right). \tag{3.3.6}$$

To further clarify this expression, $\tilde{f}_c^{(1)}(x/z_2,\mu''^2)$ is substituted in[3]

$$\begin{aligned}\tilde{f}_a^{(2)}(x,\mu^2) = &\sum_c \int_{\mu_0^2}^{\mu^2} \frac{d\mu''^2}{\mu''^2} \frac{\Delta_a(\mu^2,\mu_0^2)}{\Delta_a(\mu''^2,\mu_0^2)} \int_x^{z_M} dz_2 P_{ac}^{(R)}(\alpha_s(\mu''^2),z_2) \\ &\times \sum_b \int_{\mu_0^2}^{\mu''^2} \frac{d\mu'^2}{\mu'^2} \frac{\Delta_c(\mu''^2,\mu_0^2)}{\Delta_c(\mu'^2,\mu_0^2)} \int_{x/z_2}^{z_M} dz_1 P_{cb}^{(R)}(\alpha_s(\mu'^2),z_1)\Delta_b(\mu'^2,\mu_0^2)\tilde{f}_b\left(\frac{x}{z_1 z_2},\mu_0^2\right).\end{aligned} \tag{3.3.7}$$

Starting from a parton b at scale μ_0 and momentum fraction $x_0 = \frac{x}{z_1 z_2}$, with $\tilde{f}_b\left(\frac{x}{z_1 z_2},\mu_0^2\right)$ depicting the parton's distribution. The evolution from μ_0 to μ' without resolvable emission is characterised by $\Delta_b(\mu'^2,\mu_0^2)$. The branching into parton c at μ' with the associated momentum fraction $(1-z_1)x_0$ occurs with probability $P_{cb}^{(R)}(\alpha_s(\mu'^2),z_1)$. Subsequently, parton c evolves to μ'' without resolvable emissions, managed by the ratios of the Sudakov form factors $\Delta_c(\mu''^2,\mu_0^2)/\Delta_c(\mu'^2,\mu_0^2)$. The final branching at μ'' results in a parton of flavour a with probability $P_{ac}^{(R)}(\alpha_s(\mu''^2),z_2)$ for the momentum fraction $(1-z_2)x_1$, completing the series of transformations before evolving from μ'' to μ represented by $\Delta_a(\mu^2,\mu_0^2)/\Delta_a(\mu''^2,\mu_0^2)$.

This methodology underscores the necessity for a Monte Carlo scheme in order to simulate these iterative processes, where the iterations will be limited by reaching the scale μ. Furthermore, the iterative model naturally generates transverse momenta at each branching, this occurs when a parton is emitted. However, these are not yet incorporated in this model, which focusses solely on collinear distributions. To extend towards transverse momentum dependent parton distribution functions (TMD PDFs or TMDs), an adaptation of the equations in (3.2.15) is required. This adjustment allows for the integration of transverse momenta in branchings, enhancing the model's complexity and realism.

The transition from collinear to transverse momentum considerations involves a connection between the evolution scale μ and the kinematic variables, this is called kinematic mapping. This will be further explained in subsequent section.

3.4 TMDs and Ordering Variables

The transverse momentum dependent parton distribution (TMD) $\mathcal{A}_a(x,k_\perp,\mu^2)$ characterises a parton of type a with longitudinal momentum fraction x and transverse momentum $k_\perp$[4] at the scale μ. This TMD is more susceptible to infrared effects compared to the collinear counterpart $\tilde{f}_a(x,\mu^2)$. Infrared sensitivity implies a dependency on low-energy or long-distance physics, complicating perturbative calculations (see Ref. [23], p193). Without going into detail, to address this issue in the PB TMD framework, a specific conditions is required. Like those

---

[3] The variables which are used, align with the previous definition of a two-branching process.

[4] The notation that is used follows $k = (k^0,\ k^1,\ k^2,\ k^2) = (E_k,\ \mathbf{k}_\perp,\ k^2)$ and $\mathbf{k}_\perp = (k^1,\ k^2)$ with $k_\perp = |\mathbf{k}_\perp|$.

provided by angular ordering, which is detailed in references such as [23] and further discussed in [24] regarding its necessity for TMDs.

Referring to schematic **(b)** in Fig. 3.1, consider a branching event involving an emitted parton of flavour c. The longitudinal direction is denoted as the z-axis, with the transverse plane defined by two perpendicular directions. The transverse momenta for partons a, b, and the emitted parton c are represented by the vectors $\vec{k}_{a,\perp}$, $\vec{k}_{b,\perp}$, and $\vec{k}_{c,\perp}$, respectively.

The kinematic mapping for angular ordering [25] is given by:

$$\mu' = \frac{|\boldsymbol{k}_{c,\perp}|}{1-z} = \frac{q_\perp}{1-z} \tag{3.4.1}$$

The transverse momentum of the emitted parton receives its own symbol $q_\perp$, because it has computational significance. This will become clear in the subsequent sections. During hard scattering, the transverse momentum of the interacting parton is the vector sum of the transverse momenta from all emitted partons plus the original parton's momentum. Momentum conservation in each branching dictates that the transverse momenta of the resulting partons a and c are equal and opposite. Thus, the total[5] transverse momentum of the parton entering the hard scattering is:

$$\boldsymbol{k}_\perp = \boldsymbol{k}_{b,\perp} - \sum_c \boldsymbol{k}_{c,\perp}. \tag{3.4.2}$$

The relationship between the TMD $\mathcal{A}_a(x, \boldsymbol{k}_\perp, \mu^2)$ and the collinear PDF $\tilde{f}_a(x, \mu^2)$ is established by integrating the TMD over the transverse momentum and weighting by the longitudinal momentum fraction:

$$\int x\mathcal{A}_a(x, \boldsymbol{k}_\perp, \mu^2)\frac{d^2\boldsymbol{k}_\perp}{\pi} = \tilde{f}_a(x, \mu^2). \tag{3.4.3}$$

Further, from the angular ordering in (3.4.1) and the parton branching equation (3.2.15), the evolution equation for TMDs can be derived as:

$$\begin{aligned}\tilde{\mathcal{A}}_a(x, \boldsymbol{k}_\perp, \mu^2) = \Delta_a(\mu^2, \mu_0^2)\tilde{\mathcal{A}}_a(x, \boldsymbol{k}_\perp, \mu_0^2) + \sum_b \int \frac{d^2\mu'}{\pi\mu'^2}\frac{\Delta_a(\mu^2, \mu_0^2)}{\Delta_a(\mu'^2, \mu_0^2)}\Theta(\mu^2 - \mu'^2)\Theta(\mu'^2 - \mu_0^2) \\ \times \int_x^{z_M} dz P_{ab}^{(R)}(\alpha_s, z)\tilde{\mathcal{A}}_b\left(\frac{x}{z}, \boldsymbol{k}_\perp + (1-z)\mu', \mu'^2\right),\end{aligned} \tag{3.4.4}$$

where $\tilde{\mathcal{A}}_a$ denotes the momentum-weighted distribution defined by $\tilde{\mathcal{A}}_a := x\mathcal{A}_a$. The iterative approach applied to $\tilde{f}_a(x, \mu^2)$ is similarly employed here, following the series

$$\tilde{\mathcal{A}}_a(x, \boldsymbol{k}_\perp, \mu^2) = \sum_{i=0}^{\infty} \tilde{\mathcal{A}}_a^{(i)}(x, \boldsymbol{k}, \mu^2), \tag{3.4.5}$$

with

$$\tilde{\mathcal{A}}_a^{(0)}(x, \boldsymbol{k}_\perp, \mu^2) = \Delta_a(\mu^2)\tilde{\mathcal{A}}_a(x, \boldsymbol{k}_\perp, \mu_0^2), \tag{3.4.6}$$

$$\begin{aligned}\tilde{\mathcal{A}}_a^{(1)}(x, \boldsymbol{k}_\perp, \mu^2) = \sum_b \int \frac{d^2\mu'}{\pi\mu'^2}\frac{\Delta_a(\mu^2)}{\Delta_a(\mu'^2)}\Theta(\mu^2 - \mu'^2)\Theta(\mu'^2 - \mu_0^2) \\ \times \int_x^{z_M} dz P_{ab}^{(R)}(\alpha_s, z)\Delta_b(\mu'^2)\tilde{\mathcal{A}}_b\left(\frac{x}{z}, \boldsymbol{k}_\perp + (1-z)\mu', \mu_0^2\right).\end{aligned} \tag{3.4.7}$$

---

[5] Instead of the process that occurs in schematic **(b)** in Fig. 3.1, now there can be multiple emitted partons. Which necessitates the summation over all emitted partons.

and continuing accordingly. This includes the angular ordering successfully in the PB TMD model. This model is integral to simulations of proton-proton collisions within the software this thesis employs, describing the evolution of partons that participate in the hard interaction and enabling predictions of parton emissions prior to the hard process.

Analogously to the case of ordinary, collinear PDFs, the distribution $\tilde{\mathcal{A}}_a(x, \boldsymbol{k}_\perp, \mu_0^2)$ at the starting scale μ_0 of the evolution is a nonperturbative boundary condition to the evolution equation, and is to be determined from experimental data (as in Ref. [11]). In general, the nonperturbative starting distribution $\tilde{\mathcal{A}}_a(x, \boldsymbol{k}_\perp, \mu_0^2)$ can be flavour- and x-dependent; however, for simplicity a factorised form is used:

$$\tilde{\mathcal{A}}_a(x, \boldsymbol{k}_\perp, \mu_0^2) = \tilde{f}_a(x, \mu_0^2) \cdot \frac{\exp\left(-|\boldsymbol{k}_\perp|^2/\sigma^2\right)}{2\pi\sigma^2}, \tag{3.4.8}$$

in which the intrinsic $\boldsymbol{k}_\perp$-distribution is given by a Gaussian distribution with width $\sigma = q_s/\sqrt{2}$, and it is independent of parton flavour and x. The parameter q_s is called the intrinsic-k_T parameter.

A remark can be made that the structure of the TMD distribution is not the same for quarks and gluons in the PB method: both the evolution kernels $P^{(R)}$ and the intrinsic distributions $\mathcal{A}_0$ are in general different for different parton species. Taking a simple flavour-independent (and x-independent) Gaussian in the starting distribution is not a feature of the PB method, but rather it is motivated by the finding in Ref. [26] that the precision DIS data from HERA used for the fits are not sensitive to the flavour structure of the intrinsic distribution.

3.5 Dynamical Resolution Scale

The previously discussed PB formalism formulates the QCD evolution of TMD distribution functions by considering soft-gluon coherence effects. This formalism introduces a soft-gluon resolution scale, which distinguishes resolvable from non-resolvable branchings, exploiting the relationship between transverse-momentum recoils and branching scales. An important point in obtaining TMD distributions from the PB method concerns the ordering variables used to perform the branching evolution. Because the transverse momentum generated radiatively in the branching is sensitive to the treatment of the non-resolvable region [27], a supplementary condition is needed to relate the transverse momentum recoil and the scale of the branching. This relation embodies the well-known property of angular ordering, and it implies that the soft-gluon resolution scale can be dynamical, i.e. dependent on the branching scale. This dynamic approach contrasts with fixed resolution scales and accounts for the angular ordering property of soft-gluon emissions.

The implementation of a dynamical resolution scale starts by introducing the parameter q_0, it is the minimum transverse momentum for an emitted parton that can be resolved. In other words:

$$q_\perp > q_0. \tag{3.5.1}$$

Using the angular ordering relation of Eq. 3.4.1 in this inequality, the condition for resolving soft gluons becomes:

$$z < z_M(\mu') = 1 - q_0/\mu' \tag{3.5.2}$$

where $q_0 \gtrsim \Lambda_{\mathrm{QCD}}$.

This means that the full kernels[6] of Eqs. (3.2.15) and (3.4.4) are supported in the resolvable emission region $x < z < z_M$. To understand this in detail, several key components of the evolution equations need to be considered. Although some of it has been previously explained, it is important to reiterate certain things in this context.

Evolution equation (3.4.4) describes how the transverse momentum dependent distributions evolve with respect to the energy scale. This equation involves probabilities of parton branchings or emissions. The kernels are functions that describe the probability density of parton b splitting into parton a and c with a specific fraction of momentum z at a specific scale μ.

The resolvable emission region is defined by the constraints on the variable z:

- $x < z$: Ensures that the momentum fraction z transferred during the branching is greater than the longitudinal momentum fraction x of the parton in the hadron.
- $z < z_M$: Ensures that the branching is within the resolvable range, meaning the emission can be resolved (detected or distinguished) given the resolution scale z_M.

The kernels are designed to be active only within the range where $x < z < z_M$. This means that only emissions resulting in a parton carrying a fraction of momentum z within this range are considered in the evolution process. Emissions outside this range are considered non-resolvable and do not contribute to the evolution described by these kernels. This constraint ensures that the evolution equations account only for emissions that can be physically resolved, given the resolution scale. This aligns with the practical limitations of detecting very soft or very collinear emissions in high-energy experiments. By focusing on the resolvable emission region, the evolution equations effectively models the realistic scenario in high-energy collider experiments where only emissions above a certain threshold can be detected and analysed.

The support of the evolution kernels in the resolvable emission region can be further understood by considering two distinct cases based on the value of x relative to $1 - q_0/\mu_0$:

- **Case 1:** $x \geq 1 - q_0/\mu_0$
- **Case 2:** $x < 1 - q_0/\mu_0$

These can be seen in Figure 3.2 [24]. By considering these two cases, it can be better understood how the evolution kernels are supported in different regions depending on the value of x. This distinction is crucial for accurately modelling the evolution of TMD distributions and ensuring that only physically detectable emissions are considered in theoretical predictions.

Summary

Chapter 3, titled "Parton Branching Method," builds on the principles of QCD introduced in Chapter 2 by presenting the Parton Branching (PB) method to describe the QCD evolution of both PDFs and TMDs. This method reformulates these evolution equations using a unitarity approach, distinguishing between resolvable and non-resolvable parton branchings and employing Sudakov form factors to model the probability of no branching events between scales. The PB method is implemented numerically through iterative Monte Carlo techniques, enabling the evolution of parton distributions within hadrons from lower to higher energy scales. A significant aspect of this chapter is the extension of the PB method to include Transverse Momentum

---

[6] These full kernels are real splitting functions, $P^{(R)}$, together with the theta-functions, Θ, added by the angular ordering.

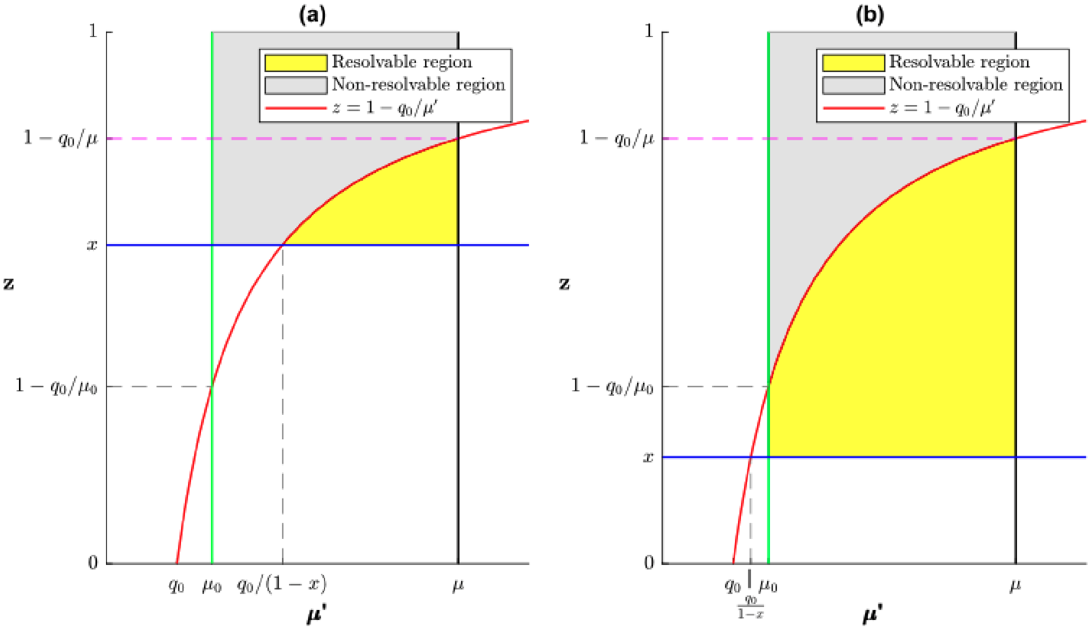

Figure 3.2: Resolvable and non-resolvable emission regions in the (z, μ') plane for evolution in the cases (a) $1 > x \geq 1 - q_0/\mu_0$ and (b) $1 - q_0/\mu_0 > x > 0$.[24]

Dependent parton distributions (TMDs), by explaining that the PB TMD method incorporates a kinematic mapping that connects the evolution scale with the transverse momentum of the emitted parton. Which is crucial for accurately describing the TMDs in processes like Drell-Yan production and for understanding parton dynamics. Furthermore, it also introduces the factorised form of the TMD; the collinear part together with an intrinsic transverse (k_T) distribution. The chapter ends with the introduction of the dynamical resolution scale z_M, this is a new approach to the treatment of soft gluons and the resolvable and non-resolvable parton emissions. It is based on the kinematic mapping that was done in order to take the transverse momentum into account in the PB TMD method. This comprehensive approach ensures that the complexities of TMDs are effectively managed within the PB framework.

Next Chapter

The PB TMD approach introduced in this chapter can be used to analyse the DY lepton pair hadroproduction process, which is introduced in section 2.4.3. The next chapter will establish the inclusive DY differential cross section in the transverse momentum of the lepton pair, carried by the exchanged vector boson. It will also show literature results to validate it's application to DY.

Chapter 4

Application of PB TMD Method to Drell-Yan

The Drell-Yan (DY) process is crucial in high-energy physics for several reasons. It's a key tool in precision electroweak measurements because it provides a clean and well-understood production channel. DY data are also essential for determining parton distribution functions (PDFs), and at low masses and energies, they help us study the internal motion of partons. Additionally, DY is important for understanding how QCD works, especially in terms of how particles evolve and how soft gluons behave. When jets are added to DY processes, they become even more significant because these scenarios are often involved in key precision measurements and searches for new physics beyond the Standard Model. DY + jets also form an important background in many experiments, making them a critical part of high-energy physics research.

To study the DY process, consider the collinear factorisation formula for the inclusive DY cross section given in Eq. (2.4.33). This formula effectively describes the total cross section by integrating over all possible transverse momenta of the produced lepton pair. However, when the transverse momentum (p_T) distribution of the DY process is of interest, the situation becomes more complex.

The formula in Eq. (2.4.33) relies on collinear factorisation, where PDFs $f(x, \mu^2)$ depend only on the longitudinal momentum fraction x and a factorisation scale μ. This approach works well for the total cross section but is not sufficient when considering the p_T-differential cross section, where the effects of transverse momenta $k_\perp$ emitted during parton branching become significant. To accurately describe the p_T distribution, it must go beyond collinear factorisation and incorporate Transverse Momentum Dependent (TMD) parton distributions, $\tilde{\mathcal{A}}(x, k_\perp, \mu^2)$, as defined in Eqs. (3.4.4) and (3.4.5).

In this generalisation, the collinear PDFs $f(x, \mu^2)$ in Eq. (2.4.33) are replaced by the full TMD distributions $\mathcal{A}(x, k_\perp, \mu^2)$, which depend on both the longitudinal momentum fraction x and the transverse momentum $k_\perp$ of the incoming partons. The TMD distributions are then convoluted with hard scattering functions H, which describe the short-distance interactions and are computed using perturbative QCD at next-to-leading order (NLO) in the strong coupling constant α_s.

It is important to note that while the inclusive cross section (integrated over p_T) remains unchanged, the differential cross section with respect to p_T requires this more detailed treatment. The Monte Carlo event generator MadGraph5_aMC@NLO [28] (referred to as MC-at-NLO hereafter) is employed to construct the hard scattering events, and when combined with the TMD parton distributions, it enables predictions for the DY transverse momentum distribution. Specifically, MC-at-NLO normalises the p_T-differential cross section to ensure that its integral matches the known next-to-next-to-leading order (NNLO) total cross section.

The precise procedure to combine the results from MC-at-NLO with the TMD evolution provided by the CASCADE generator [29, 30] has been developed in Refs. [13, 14], and will be briefly summarised in this chapter. This combination allows for accurate predictions of the DY p_T spectrum while maintaining consistency with the total cross section calculated at NNLO.

4.1 Determination of TMD Distributions

The initial parton distributions at the starting evolution scale, μ_0, need to be determined through fits to experimental data. To achieve this, the PB approach employs the `xFitter` platform [31, 32] to perform fits for the collinear part of the starting distribution. This collinear part is the $\tilde{f}(x, \mu_0^2)$ in Equation (3.4.8). In a previous study [26], the most commonly used PB parton distributions were derived from fits to precision Deep Inelastic Scattering (DIS) data from HERA [33] at Next-to-Leading Order (NLO). Specifically, these PDFs were obtained using NLO evolution convoluted with NLO DIS matrix elements.

The scale at which the strong coupling α_s should be evaluated in Eqs. (3.4.4) and (3.2.11) depends on the branching variables. Two specific cases have been investigated in Refs. [11, 24, 26]:

$$\text{i)} \quad \alpha_s = \alpha_s(\mu'^2) \tag{4.1.1}$$

$$\text{ii)} \quad \alpha_s = \alpha(\mu'^2(1-z)^2) = \alpha_s(q_\perp^2) \tag{4.1.2}$$

For scenario i), it has been demonstrated in [11] that Eq. (3.4.4) accurately reproduces the DGLAP evolution (2.4.28) of parton densities when integrated over all transverse momenta, representing the collinear scenario. Ref. [24] discusses how for scenario ii), after integrating over transverse momenta and properly handling the resolution scale, Eq. (3.4.4) yields the angular-ordered CMW-type evolution [34]. Consequently, PB-NLO-HERAI+II-2018 set 1 (abbreviated as PB-NLO-2018 Set1), which uses the DGLAP-type $\alpha_s(\mu'^2)$, and PB-NLO-HERAI+II-2018 set 2 (abbreviated as PB-NLO-2018 Set2), which uses the angular-ordered CMW-type $\alpha_s(q_\perp^2)$, are obtained. Both sets of distributions assume a fixed resolution scale $z_M \to 1$, and the intrinsic-k_T parameter q_s as 0.5 GeV. The detailed investigation of q_s will be a subject of Chapter 5.

It has been found that both scenarios yield fits to the precise DIS HERA data [33] with satisfactory χ^2 values. These results confirm the accuracy of the PB evolution in reproducing either DGLAP or CMW evolution when integrated over the relevant variables. Both PB-NLO-2018 Set1 and Set2 are available in the `TMDlib` [35, 36] and can be accessed through the graphical interface `TMDplotter`.

The significance of the angular-ordered coupling $\alpha_s(q_\perp^2)$ in regions dominated by soft-gluon emissions is evidenced by the improved performance of PB-NLO-2018 Set2 compared to PB-NLO-2018 Set1. This is specifically true for the description of the measured Z/γ transverse momentum spectra at the LHC [3], as well as in low-energy experiments [14]. It is also true for the description of di-jet azimuthal correlations [37, 38] measured at the LHC [39]. Based on this insight, the second scenario, the approach[1] used in PB-NLO-2018 Set2, will be utilised in Chapter 5, with the aim of examining the sensitivity of these measurements to the nonperturbative TMD intrinsic-k_T parameter q_s, and determining its value.

However, as highlighted in Refs. [13, 26], to fully define scenario *ii*), the handling of the strong coupling in the region of small transverse momenta $q_\perp \lesssim q_{\text{cut}}$, where $q_{\text{cut}} \sim \mathcal{O}(1\text{ GeV})$[2] is a semi-hard scale, needs to be specified:

$$\alpha_s = \alpha_s(\max(q_{\text{cut}}^2, q_\perp^2)). \tag{4.1.3}$$

This is needed to avoid the nonperturbative region, since with large z the scale $q_\perp$ in the angular ordering equation (3.4.1) can become very small. The research of this thesis in Chapter 5 will use fits that use this treatment, which were done in Refs. [40, 41].

4.2 Semi-hard Parton Emissions

Ref. [42] discusses the treatment of nonperturbative contributions and the handling of the small p_T region in the PB TMD approach, aiming to clarify the underlying physical picture. The PB TMD method incorporates Sudakov evolution by integrating appropriate kernels over the phase space within the resolvable region, i.e. over momentum fractions z up to the soft-gluon resolution scale z_M. For each branching evolution scale μ'^2, it is useful to distinguish between parton emissions with transverse momenta above the semi-hard scale q_0 ($q_\perp > q_0$) and those below q_0 ($\Lambda_{\text{QCD}} < q_\perp \lesssim q_0$).

Using the angular ordering relation (3.4.1), these emissions correspond to the following regions:

$$(a) \quad z < z_{\text{dyn}} = 1 - q_0/\mu', \tag{4.2.1}$$

$$(b) \quad z_{\text{dyn}} \lesssim z < z_M, \tag{4.2.2}$$

where z_{dyn} is the dynamical resolution scale discussed previously in Section 3.5. Region (a) covers the perturbative regime, where the strong coupling $\alpha_s(q_\perp^2)$ is evaluated at the scale of the emitted transverse momentum. The contribution from region (a) to the evolution equations (3.4.4) and (3.2.11) corresponds to the perturbative Sudakov resummation, as discussed in [43]. Region (b) covers the nonperturbative regime, where the strong coupling is effectively frozen at the semi-hard scale, $\alpha_s(q_0^2)$, if $q_{cut} \sim q_0$[3]. The contribution from region (b) to the evolution constitutes the nonperturbative Sudakov form factor within the PB TMD approach.

Notably, PB-NLO-2018 Set2 is designed to accurately describe both regions (a) and (b), as they used the fixed resolution scale $z_M \to 1$. In contrast, standard Monte Carlo generators typically employ a dynamical resolution scale setting, $z_M = z_{\text{dyn}}$, which effectively bypasses the nonperturbative Sudakov in the evolution. Chapter 5 explores scenarios that mimic the behaviour of standard Monte Carlo generators by focusing on configurations with a dynamic z_M, thereby covering only region (a).

---

[1] Only the fact that this set uses scenario *ii)* is meant here. The research will use a dynamical, instead of a fixed, resolution scale.

[2] It is often assumed that the value of q_{cut} does not have a significant impact on the treatment of the strong coupling, as long as it stays around the order of 1 GeV.

[3] Although not necessary, most studies take these semi-hard scales to be equal: $q_{\text{cut}} = q_0$.

4.3 Calculation of Drell-Yan Cross Sections

Now the technicalities of generating collider predictions within the PB approach are described, focusing on matching NLO matrix elements with PB TMDs, as introduced in Refs. [13, 14].

The DY p_T cross section in proton-proton collisions at the LHC is computed at NLO using MC-at-NLO. In the standard collinear MC-at-NLO approach, the NLO cross section's collinear and soft contributions are subtracted, as these will be included later when applying the parton shower. When combining MC-at-NLO with TMDs, the TMDs play a similar role as the parton shower, so subtraction has to be involved as well. HERWIG6 subtraction terms are used within the MC-at-NLO framework, as this parton shower generator operates under the same angular ordering conditions as the PB TMD parton distribution set PB-NLO-2018 Set2, described in a previous section. The consistency and validity of using HERWIG6 subtraction terms together with PB TMD distributions in MC-at-NLO have been examined in Ref. [44]. Since MC-at-NLO is a collinear matrix element generator, an integrated TMD (iTMD) has to be used to generate cross sections. MC-at-NLO generates weighted events, stored in a format compatible with parton shower event generators (LHE format [45]).

The factorisation scale μ_F for the hard process calculation is set to $\mu_F = \frac{1}{2}\sum_i \sqrt{m_i^2 + p_{t,i}^2}$, summing over all final state particles i. For DY and Z production, this includes all decay leptons and the final jet. The factorisation scale μ for generating transverse momentum according to the PB-TMD distributions is set to $\mu = m_{DY}$ for the Born configuration[4] and $\mu = \frac{1}{2}\sum_i \sqrt{m_i^2 + p_{t,i}^2}$ for real emission contributions. The generated transverse momentum is constrained by the matching scale $\mu_m =$ SCALUP [29], which prevents double counting between the matrix element calculation's real emission contribution and the PB-TMD contribution. This scale, determined by the NLO calculation, is passed to the user via the SCALUP parameter (included in the LHE file).

In the next step, transverse momentum $k_\perp$ is introduced to the subtracted collinear matrix element using an algorithm within `CASCADE` [29, 30]. This momentum is incorporated into the event record following the distribution prescribed by the TMD function. The TMD applied in `CASCADE` corresponds to the same iTMD used during the initial generation of the matrix element. To ensure energy-momentum conservation and preserve the Drell-Yan system's invariant mass, the longitudinal momentum fractions of the incoming partons must be recalibrated. `CASCADE` also provides the option to include a parton shower (PS), it is the only Monte Carlo generator that implements an initial-state TMD PS. However, a TMD final-state PS is not yet available, so `PYTHIA` is used to handle the final-state showering. For inclusive Drell-Yan (DY) predictions, the initial-state parton shower is not required since the complete kinematic information is already embedded within the TMDs. Furthermore, CASCADE3 allows the Les Houches Event (LHE) files to be read and output files to be generated for analysis with Rivet [46].

The p_T spectrum of Z-bosons coming from the MC-at-NLO calculation at a purely partonic level (LHE level) is presented in Fig. 4.1 (left). This figure illustrates the distributions obtained using HERWIG6 and HERWIG++ subtraction terms. In Fig. 4.1 (right), the distribution is shown after incorporating transverse momenta based on the PB TMDs. The differences between the calculations using different subtraction terms are minimal, as evidenced by the ratios in the

---

[4] This terminology is used to describe a reaction that occurs in *one step*; in other words, a reaction between two particles in the classic sense.

lower panels. The PB TMDs contribute to the p_T spectrum of the Z-boson up to the hard process scale, not only in the non-perturbative region, since the TMDs extend to large k_t [13].

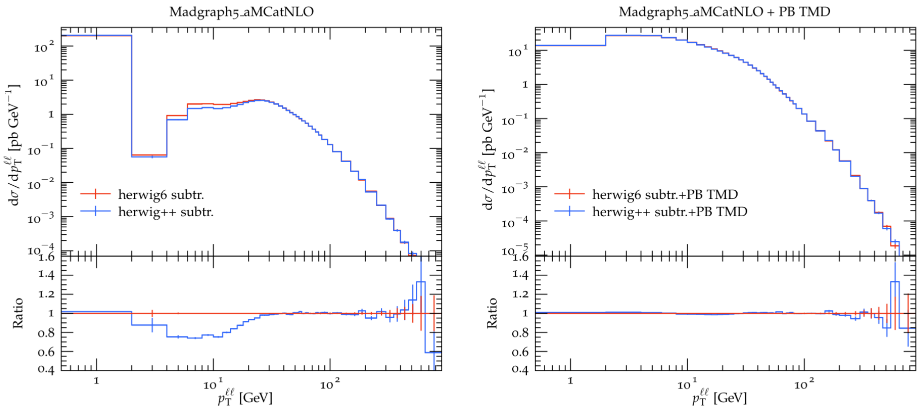

Figure 4.1: Transverse momentum spectrum of Z obtained for different subtraction terms: (left) at parton level (LHE level), (right) after inclusion of PB-TMDs. [13]

4.4 Results on Drell-Yan from PB TMD

This section will demonstrate how good the PB TMD approach works for predicting the inclusive DY p_T data.

Ref. [13] combined the PB TMD method with NLO collinear matrix element calculations for the first time and compared it to ATLAS data at $\sqrt{s} = 8$ TeV. This can be seen in the figure they obtained, here Figure 4.2. A very good agreement with the ATLAS measurements for the

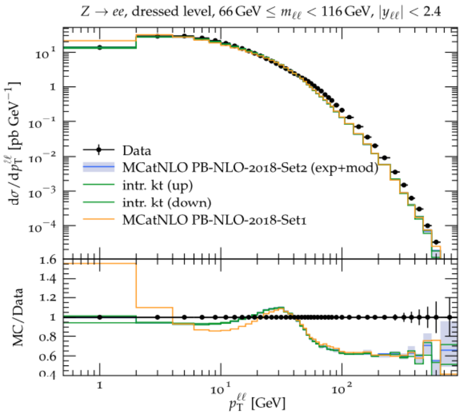

Figure 4.2: Transverse momentum p_T spectrum of Z-bosons as measured by ATLAS at $\sqrt{s} = 8$ TeV compared to the prediction from MC-at-NLO with PB-TMD NLO 2018 [26][13].

low transverse momentum cross sections of Z-boson production is observed. This agreement goes well until approximately 40 GeV, higher order contributions are needed to obtain good agreement for higher p_T. Such higher order contributions can be efficiently taken into account by TMD multi-jet merging [47–49] technique as can be seen in Fig. 4.3 [47]. The description of the Z-boson spectrum is good throughout the range in p_T.

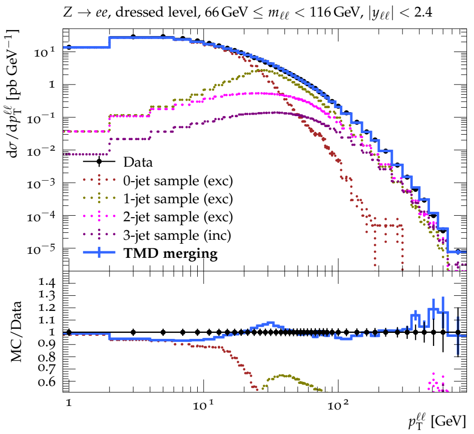

Figure 4.3: Transverse momentum p_T spectrum of Z-bosons as measured by ATLAS at $\sqrt{s} = 8$ TeV compared to the prediction from TMD multi-jet merging [47].

In reference [14], the PB TMD approach was employed to analyse the DY p_T spectrum across a broad kinematic range, encompassing various center-of-mass (COM) energies ($\sqrt{s}$) and DY masses. This approach was validated using data from multiple experiments: R209, Phenix, NUSEA, and CMS. In Fig. 4.4, the DY p_T cross sections are shown for various COM energies. A significant finding was that the PB approach effectively described all these kinematic regions with a consistent set of parameters, PB-NLO-2018 Set2. This consistency was crucial because, unlike standard Monte Carlo generators, which often require parameter tuning—particularly for the intrinsic k_T—the PB TMD approach utilised fixed parameters throughout the analysis. Furthermore, these results addressed an issue known as the *low* q_T *crisis*, noticed in the literature by Bacchetta *et al.* [50]. This issue pertains to the inadequacy of perturbative fixed-order calculations within collinear factorisation for describing DY p_T spectra at fixed target experiments, particularly in the $p_T \sim Q$ region where perturbation theory was expected to be effective. Reference [14] confirmed this observation and clarified the underlying problem using a subtraction method. Specifically, at higher DY masses and LHC energies, the soft gluon contribution in the region $p_T/m_{DY} \sim 1$ is minimal, with the spectrum being predominantly influenced by hard real emission. Conversely, at lower DY masses and energies, even in the region $p_T/m_{DY} \sim 1$, the contribution from soft gluon emissions is significant and is encapsulated in TMDs.

Summary

Chapter 4 begun with explaining the procedure of obtaining the initial collinear PDFs for the TMD in Eq. 3.4.8. Afterwards, it detailed the use of the PB TMD method of Chapter 3 for collider predictions. It explained how PB TMDs are matched with Next-to-Leading Order (NLO) matrix elements using the Cascade generator [29, 30]. This approach increases the accuracy of collider predictions by integrating PB TMDs with standard collinear matrix element generators. Additionally, the chapter provides an overview of significant results related

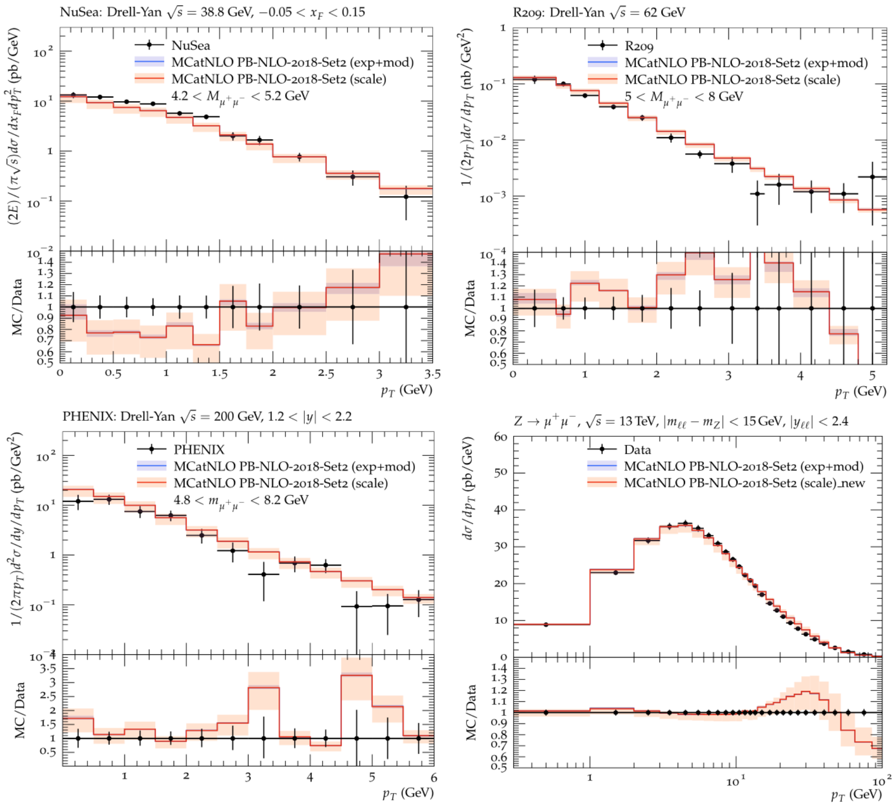

Figure 4.4: Transverse momentum spectrum of Drell-Yan production measured by NuSea, R209, PHENIX and CMS, compared to predictions at NLO using PB-TMDs [14].

to inclusive DY transverse momentum (p_T) data. Key findings include the effectiveness of the method in describing DY transverse momentum spectra across various kinematic ranges and energy scales. It creates a clear picture of the description that the PB TMD method is able to provide for inclusive DY p_T cross sections.

Next Chapter

Instead of the fixed resolution scale that was used for the results summarised in this chapter, the dynamical resolution scale of section 3.5 can also be used in the PB TMD method. This will be done for the first time on Drell-Yan data in the next chapter.

Chapter 5

Analysis of Drell-Yan Data for Varying COM Energies

5.1 Background

As discussed in Chapter 4, the PB TMD approach has been applied to the study of the Drell-Yan (DY) transverse momentum distributions in Refs. [13, 14, 42, 47], where theoretical predictions have been successfully compared with experimental measurements at the LHC as well as at lower energies. In all these works, the PB TMD scenario with a fixed soft-gluon resolution scale z_M has been employed. On the other hand, as discussed in Section 3.5, PB TMD scenarios with dynamical resolution scales z_M are important for understanding aspects of the physics of QCD coherence and the angular ordering of gluon radiation. The purpose of the research reported in this chapter is to analyse, for the first time, inclusive DY transverse momentum distributions across a wide range of energies using PB TMD with a dynamical resolution scale.

The study with dynamical z_M also influences the general area of Monte Carlo parton-shower event generators. A long-standing question in this area has been the mismatch between the PDFs, which are evolved without any z_M, and the parton shower whose evolution does include the resolution scale. This is exemplified in the cases of Herwig [7] and Pythia [6] parton showers. This question has recently been revisited in studies such as Refs. [51, 52]. This issue is further affected by the transverse momentum recoils in the initial state shower [53, 54], and the corresponding longitudinal momentum shifts. Indeed, it is observed in Refs. [42, 55] that the treatment of soft gluons in the non-resolvable region, identified according to the dynamical resolution scale, can strongly influence the determination of the intrinsic k_T parameter q_s in TMD distributions and in parton showers. With the analysis of DY data using PB TMD with dynamical z_M in the present chapter, it will be shown that it is possible to investigate the behaviour of the parameter q_s with varying COM energies, and compare it with the results from Refs. [42, 55] and from parton showers, e.g., [56, 57]. It is worth noting that analogous correlations between the intrinsic k_T distribution and nonperturbative Sudakov effects are also studied, in the context of the CSS approach [5], in Ref. [58].

The research work reported in this chapter follows the same methodology as in Ref. [42], but with a dynamical resolution scale z_M, such that the collinear distributions are fitted to Deep

Inelastic Scattering (DIS) data which are determined in Refs. [40, 41]. The nonperturbative parameter q_0 in the dynamical z_M is set to 0.5 GeV. The same value is used for the cut in α_s, q_{cut}, as explained in Sec. 4.1.

5.2 Methodology

The chapter will investigate the inclusive DY p_T spectrum from the data of experiments across a large COM energy range, namely R209 (62 GeV), Phenix (200 GeV), CDF (1.96 TeV), D0 (1.96 TeV), ATLAS (8 TeV) and CMS (13 TeV).

First, the Transverse Momentum Dependent distributions (TMDs) are obtained from Refs. [40, 41]. These TMDs serve as the basis for further analysis. For each experiment, multiple replicas of the TMD distribution are generated, with each replica differing in the intrinsic transverse momentum parameter, q_s. It is important to note that all these replicas, when integrated over the transverse momentum k_T, yield the same collinear distribution. This consistency is due to q_s being generated from a normalised Gaussian distribution.

Subsequently, predictions are made for the DY p_T spectrum for each experiment based on these replicas. Les Houches Event (LHE) files are generated using the intrinsic TMDs from Refs. [40, 41], combined with the Next-to-Leading Order (NLO) matrix element from MC-at-NLO. The matrix element is enhanced by incorporating transverse momentum through the combination of the MC-at-NLO matrix element with the corresponding TMD replica within the Cascade generator, following the procedure described in Chapter 4.

The results are then plotted using Rivet [46]. Rivet includes a built-in chi-squared (χ^2) function, which is used to assess the quality of each prediction against the experimental data.

For each experiment, the value of the χ^2 function is evaluated across the replicas, i.e., for varying values of q_s; by minimising χ^2, the optimal q_s value is determined. Finally, the optimal q_s values from each experiment are compiled and plotted against the corresponding center-of-mass energy ($\sqrt{s}$). This plot provides a comprehensive overview of the behaviour of q_s as a function of the center-of-mass energy.

5.3 Initial Studies

A calculation for the DY p_T cross section with $q_s = 0.7$ GeV for ATLAS data is plotted in Figure 5.1 across the entire p_T range. Such a plot is created 15 times (for each q_s value) for each experiment. Two preliminary tests can be done in order to make sure the calculations are not influenced by statistical factors and that the optimal p_T range is studied.

The first test that was performed was to determine the number of LHE files required to produce results independent of statistical fluctuations. Every LHE file has 500000 events. This process is summarised in Figure 5.2 (right). Initially 2000 LHE files were used to determine if this number was sufficient to mitigate statistical influences. The results were compared against those obtained with 1000 and 500 LHE files. While the results for 500 LHE files showed some statistical variations (notably small outliers in the red curve), the results between 1000 and 2000 LHE files were largely consistent. Thus, it was concluded that 2000 LHE files are adequate to produce results without significant statistical uncertainties.

Furthermore, in Figure 5.1, it is evident that beyond approximately 40 GeV, the MC approach significantly underestimates the experimental data at the LHC (as was explained in

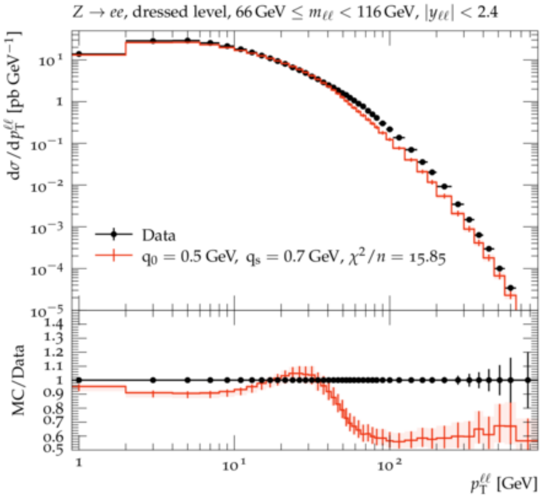

Figure 5.1: The differential cross section in function of the transverse momentum, calculated with a TMD using $q_0 = 0.5$ GeV and $q_s = 0.7$ GeV. The experimental data comes from ATLAS. The χ^2/n value gives the overall goodness of the fit. On the bottom is the ratio of Monte Carlo with data, showcasing the correctness of the TMD fit in a certain p_T^{ll} area.

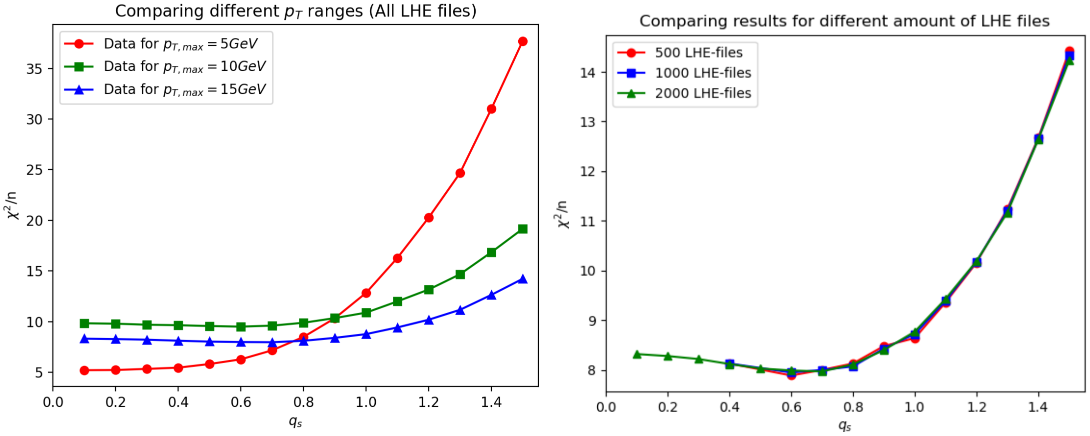

Figure 5.2: (Left) The χ^2/n vs q_s plot for different ranges of transverse momentum in the calculation of the differential cross section, all LHE files are used (2000). (Right) The χ^2/n vs q_s plot for different amount of LHE files used, $p_{T,\max} = 15$ GeV is used.

Chapter 4). This is because the TMD dynamics is expected to be relevant for $p_T/M \ll 1$, consequently, analysing the small p_T range becomes crucial. For this research, the value $p_{T,\max} = 15$ GeV was chosen. It was identified as the optimal value within the range $p_{T,\max} = [5, 10, 15]$ GeV, as demonstrated in Figure 5.2 (left). This figure shows that $p_{T,\max} = 5$ GeV does not produce a clear minimum, rendering it unsuitable for the ATLAS experiment. This observation holds true across all experiments examined. Conversely, both $p_{T,\max} = 10$ GeV and $p_{T,\max} = 15$ GeV yield good results, with $p_{T,\max} = 15$ GeV providing a superior overall fit (lower χ^2/n values). However, for some experiments, the transverse momentum range of the experimental data does not extend to $p_{T,\max} = 15$ GeV; specifically, Phenix has $p_{T,\max} = 6$ GeV and R209 has $p_{T,\max} = 5$ GeV. For these experiments, their respective maxima were chosen.

5.4 PB TMD Analysis for Different DY Datasets

A calculation for each experiment, with $q_s = 0.7$ GeV, is presented in Figures 5.3 (a)–(f). Among other things, they illustrate the number of data points per experiment for the given p_T region. These data points are listed in Table 5.1 and represent the degrees of freedom (n) in the χ^2/n value. These are remarkable plots, most plots have a satisfactory prediction of the DY data, which indicates that the PB TMD method is a valid approach. There are two exceptions: CDF and D0, Figure 5.3 (c) and (d), respectively, for CDF it can be seen that the prediction is less satisfactory as it fails to accurately describe the entire data set. The implications of this will be discussed in further detail later. Additionally, the D0 experiment exhibits a a limited number of data points, which leads to a predictable low sensitivity to the q_s value, as many TMDs could potentially fit these sparse data points. This issue will be shown in a subsequent section.

Experiment	**# of Data Points**
CMS	15
ATLAS	8
CDF	30
D0	4
Phenix	12
R209	13

Table 5.1: Experiments and their amount of data points in their respective p_T range.

For each q_s value within the range of 0.1—1.5 GeV, calculations were performed and the χ^2/n values were recorded. These results can be condensed into a single plot of q_s versus χ^2/n for each experiment. The goal is to identify the q_s value that minimises the χ^2/n value for each experiment. To quantify the uncertainty associated with this minimum, a one-sigma confidence region is constructed. This involves creating an uncertainty interval for q_s where $\chi^2(q_s) < \min(\chi^2) + 1$. The boundary values of this interval are then used to define the uncertainty.

For the CMS experiment, the covariance matrix of the measurements is available, providing a more precise error analysis. However, this is not the case for the other experiments. Due to the lack of comprehensive error breakdowns for most measurements, all uncertainties are treated as uncorrelated and do not account for systematic uncertainties arising from scale variations in the theoretical calculations. This methodology is applied consistently across all experiments

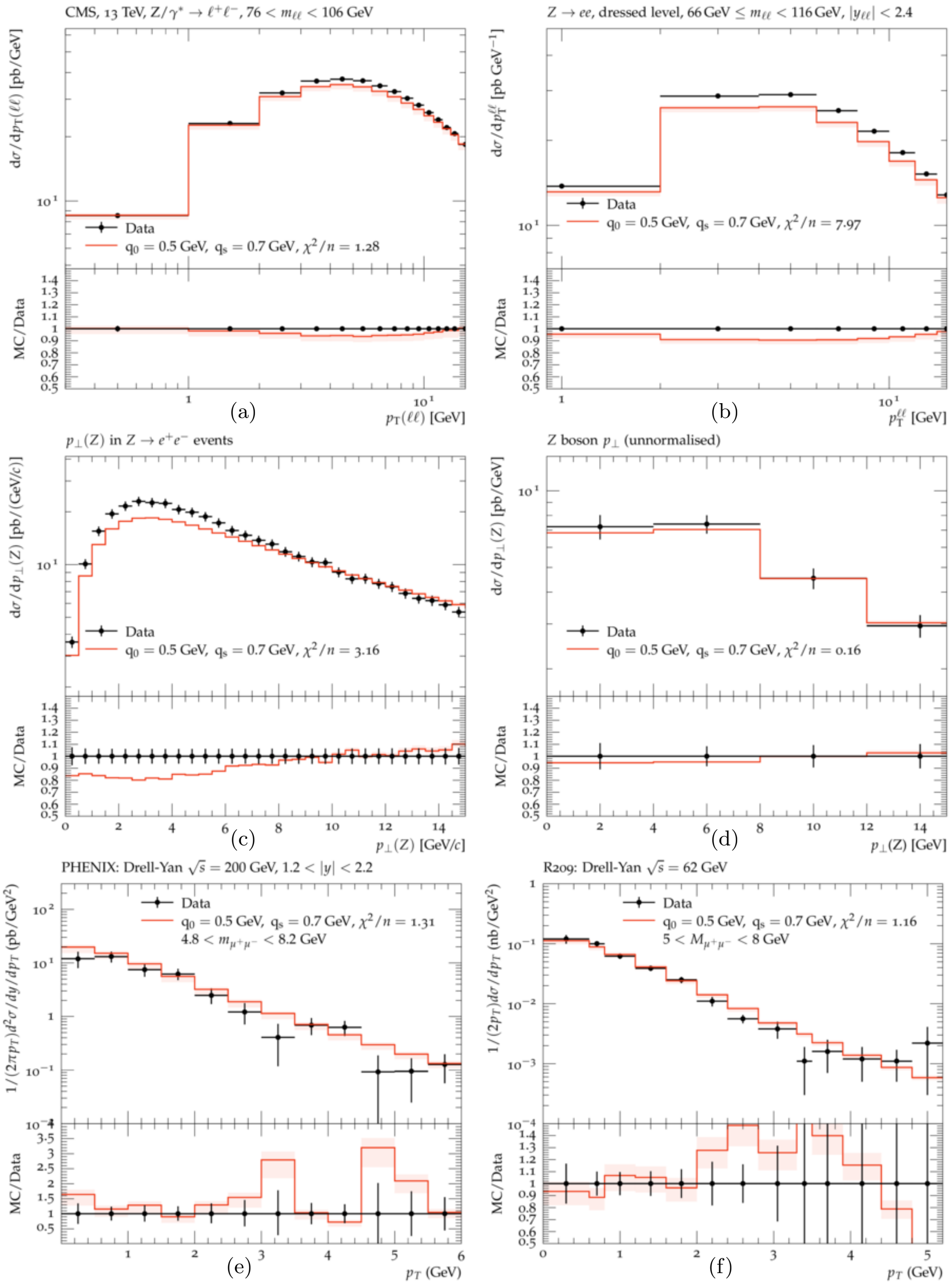

(a) (b) (c) (d) (e) (f)

Figure 5.3: Differential cross section in function of p_T for: (a) CMS, (b) ATLAS, (c) CDF, (d) D0, (e) Phenix, and (f) R209.

discussed in the following sections. The precise correlated uncertainties for the CMS experiment were taken into account in Ref. [42], but within the fixed resolution scale framework. It is important to perform a comparable analysis for the dynamical resolution scale framework, but due to time constraints this is left to future work.

CMS

As can be seen on Figure 5.3 (a), the CMS data is very well described by the PB TMD method. Therefore, the best fit will have a meaningful result. In Figure 5.4, a clear minimum can be seen at $q_s = 0.73$ GeV. This minimum was determined by a polynomial fit of the χ^2/n vs q_s data and the local minimum was computationally found. The uncertainty is shown as the blue shaded area above the minimum, this corresponds to the one-sigma confidence region, which is determined by the $\chi^2 + 1$ technique. Therefore a q_s value of 0.73 GeV is found with a one-sigma confidence interval ranging from 0.55 GeV to 0.88 GeV. In Appendix A.4 all the calculations for the varying q_s predictions are shown.

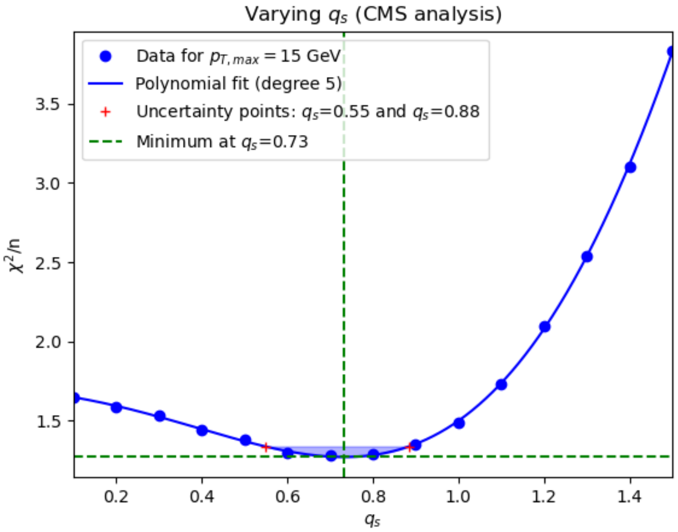

Figure 5.4: The reduced χ^2/n distribution as a function of q_s for the CMS experiment at $\sqrt{s} = 13$ TeV. The shaded area corresponds to the one-sigma confidence region around the local minimum of the distribution, which is found to be $q_s = 0.73$ GeV.

ATLAS

As can be seen on Figure 5.3 (b), the ATLAS data is also well described by the PB TMD method. However, the χ^2/n value is higher compared to the other experiments, this does not pose any problem. Only the minimum in the reduced χ^2/n distribution is needed. It does not have to be a small χ^2/n value. The reduced χ^2/n distribution can be seen in Figure 5.5. Analogous to the CMS section, a q_s value of 0.62 GeV is found with a one-sigma confidence interval ranging from 0.42 GeV to 0.78 GeV. In Appendix A.5 all the calculations for the varying q_s predictions are shown.

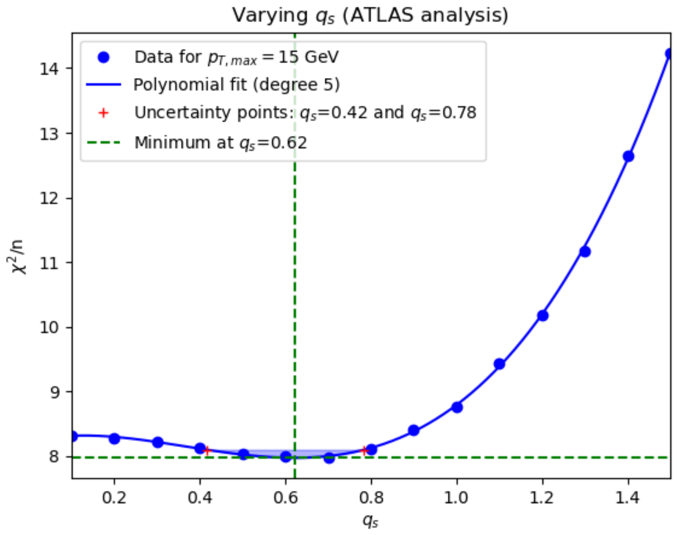

Figure 5.5: The reduced χ^2/n distribution as a function of q_s for the ATLAS experiment at $\sqrt{s} = 8$ TeV. The shaded area corresponds to the one-sigma confidence region around the local minimum of the distribution, which is found to be $q_s = 0.73$ GeV.

CDF and D0

The reduced χ^2/n distributions for CDF and D0 can be seen in Figures 5.6 and 5.7. These are shown together because they are both anomalous and they do not give a usable result.

For the CDF data, there is no observed minimum in the χ^2/n as a function of q_s. A detailed comparison of the predictions with the CDF data is provided in Appendix A.6, which presents the analysis across various q_s values. It is important to note that the CDF data is not adequately described using the PB TMD method. Consequently, evaluating the χ^2/n values appears to be of limited significance, given that the data is consistently not well-represented by the model.

For the D0 data there is no observed minimum either, however, this time it is due to a certain insensitivity to the q_s value. In Appendix A.7 all the calculations for the varying q_s predictions are shown. There are multiple q_s values that obtain the exact same χ^2/n value. The likely reason is that in this p_T range, the D0 data only has 4 data points. This is a very small amount, and the model will always fit these data points very well. This results in overall low χ^2/n values, so a large uncertainty, and most importantly, it leads to no clear minimum. Resulting in no usable result from the D0 data either.

This leaves a large energy gap in the central energy spectrum that is yet to be researched. This study tried to perform extra calculations using data from Tevatron with energy 1.8 TeV, but problems with the computer cluster were experienced. Therefore such computations could not be performed on time and determining the q_s value in this range is left as future research.

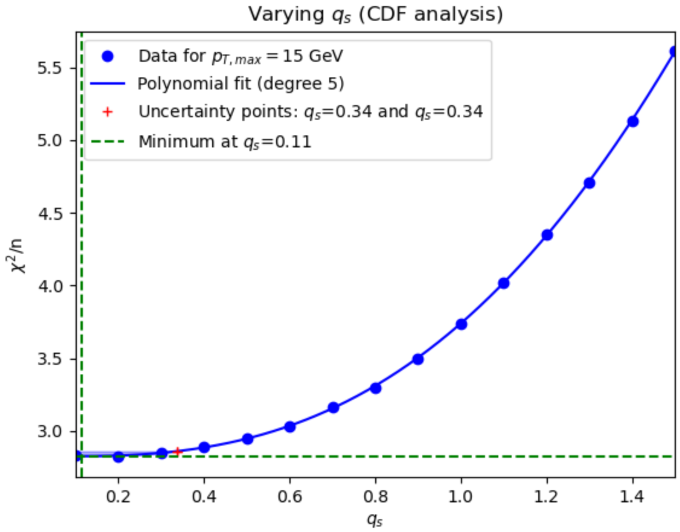

Figure 5.6: The reduced χ^2/n distribution as a function of q_s for the CDF experiment at $\sqrt{s} = 1.96$ TeV.

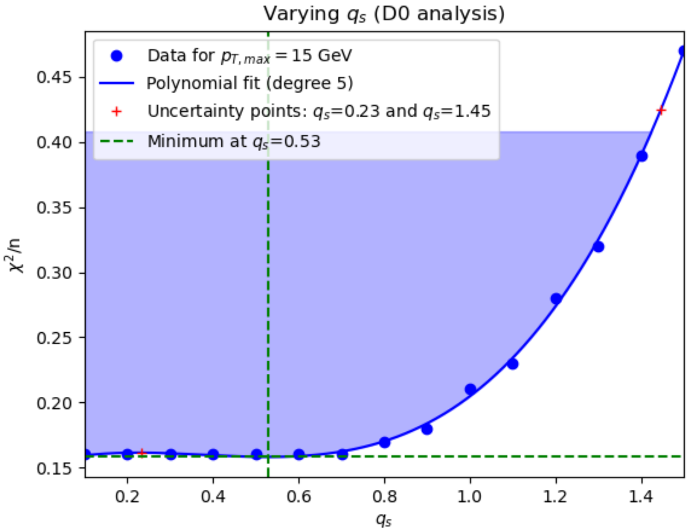

Figure 5.7: The reduced χ^2/n distribution as a function of q_s for the D0 experiment at $\sqrt{s} = 1.96$ TeV. The shaded area corresponds to the one-sigma confidence region around the local minimum of the distribution.

Phenix

As can be seen on Figure 5.3 (e), the Phenix data is also well described by the PB TMD method. Despite the presence of certain outlier data points, the overall fit appears to be reasonably accurate. The reduced χ^2/n distribution can be seen in Figure 5.8. Analogous to previous sections, a q_s value of 0.69 GeV is found with a one-sigma confidence interval ranging from 0.54 GeV to 0.84 GeV. In Appendix A.8 all the calculations for the varying q_s predictions are shown.

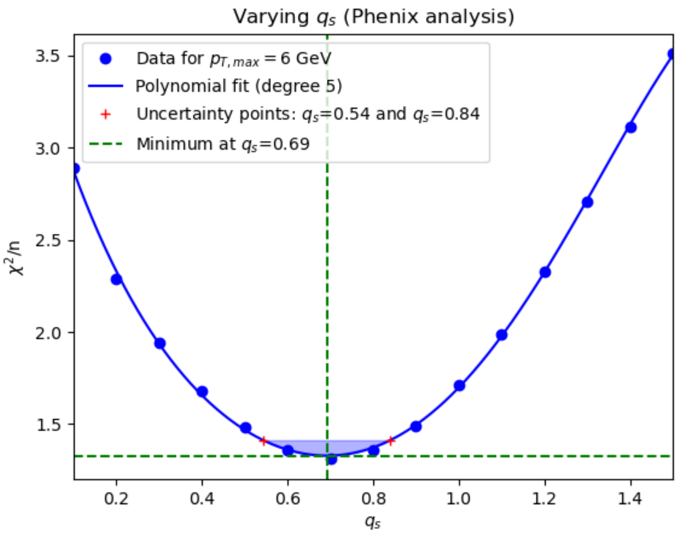

Figure 5.8: The reduced χ^2/n distribution as a function of q_s for the Phenix experiment at $\sqrt{s} = 200$ GeV. The shaded area corresponds to the one-sigma confidence region around the local minimum of the distribution, which is found to be $q_s = 0.69$ GeV.

R209

As can be seen on Figure 5.3 (f), the R209 data is well described by the PB TMD method. Again, despite the presence of certain outlier data points, the overall fit appears to be reasonably accurate. The reduced χ^2/n distribution can be seen in Figure 5.9. Analogous to previous sections, a q_s value of 0.53 GeV is found with a one-sigma confidence interval ranging from 0.46 GeV to 0.60 GeV. In Appendix A.9 all the calculations for the varying q_s predictions are shown.

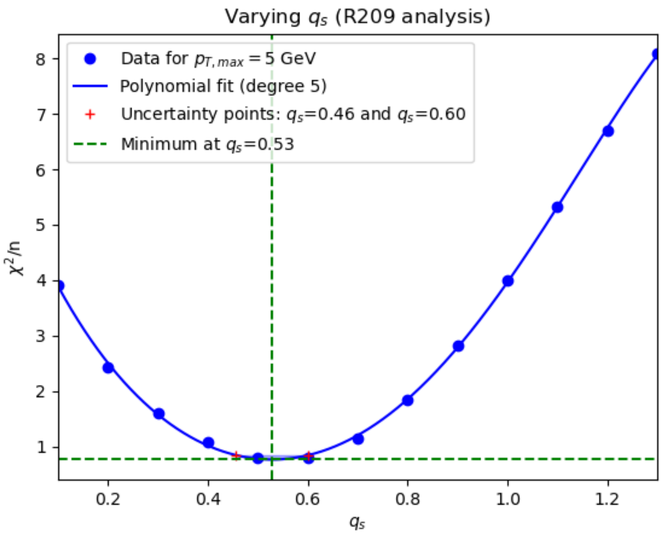

Figure 5.9: The reduced χ^2/n distribution as a function of q_s for the R209 experiment at $\sqrt{s} = 62$ GeV. The shaded area corresponds to the one-sigma confidence region around the local minimum of the distribution, which is found to be $q_s = 0.53$ GeV.

5.5 Summary and Discussion

These results can be summarised in one q_s vs COM energy plot, as can be seen in Figure 5.10. Here the value for the nonperturbative intrinsic-k_T parameter q_s remains, within uncertainty, a constant value. This means that there is no significant dependence of the q_s parameter on the COM energy when using the dynamical resolution scale, with $q_0 = 0.5$ GeV.

This result provides a new insight into the long-standing issue concerning the intrinsic-k_T parameter q_s and its dependence on COM energy. Previous studies using standard Monte Carlo (MC) event generators such as Herwig [7] and Pythia [6] had shown that q_s varies with COM energy, necessitating extensive parameter tuning to accurately describe inclusive Drell-Yan transverse momentum cross sections across different energies [56, 57]. However, Ref. [14] demonstrated that the PB TMD method, when employing the PB-NLO-2018 Set2, could achieve consistent results for varying COM energies without requiring any parameter tuning. This surprising outcome led to a detailed investigation of the intrinsic-k_T parameter q_s.

Studies have been conducted on Drell-Yan transverse momentum data using the PB TMD framework with both fixed and dynamical resolution scales z_M. In particular, Ref. [42] analysed the PB-NLO-2018 Set2 (which utilises a fixed z_M), finding that the dependence of q_s on $\sqrt{s}$ (COM energy) was insignificantly weak, indicating a stable q_s across different energy scales. On the other hand, Ref. [55] explored toy models with a dynamical z_M and large initial q_0 values (1.0 and 2.0 GeV), revealing a much stronger dependence of q_s on $\sqrt{s}$. Additionally, the references [40, 41] also provided collinear fits for $q_0 = 1.0$ GeV. For this case, a preliminary investigation of COM energy dependence of q_s was performed by an unpublished study [59] and

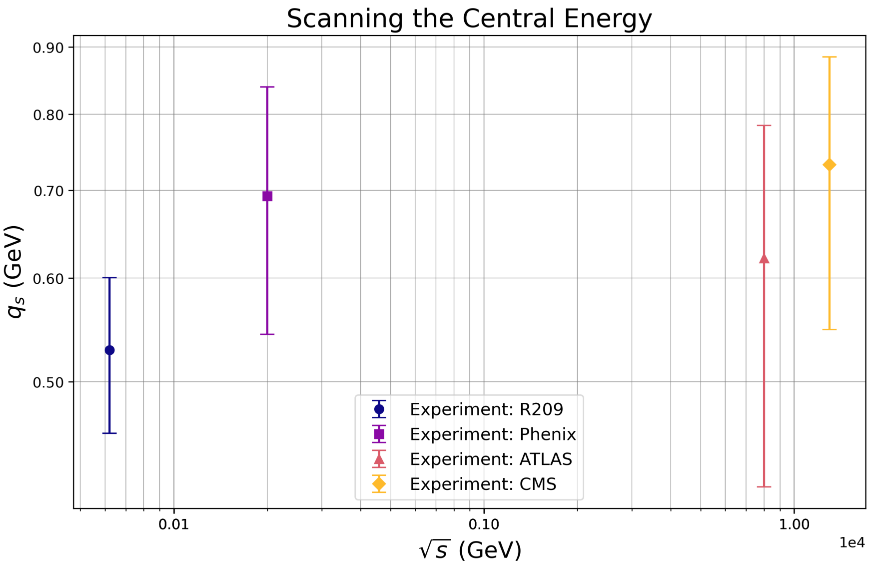

Figure 5.10: The q_s value in function of the central energy, for $q_0 = 0.5$ GeV. A gap exists for ~ 2 TeV, due to computational errors. The legend displays the corresponding experiment.

this study did observe a COM energy dependence. Their preliminary data points[1], without uncertainties, are plotted in Figure 5.11. The results of the COM dependence of the parameter q_s, presented on a log-log scale, displayed a linear relationship, with the slope increasing as q_0 increased.

The contrasting behaviour between the fixed and dynamical z_M cases was particularly noteworthy. When using dynamical z_M, the results closely matched the behaviour observed in standard MC generators, which also treat the soft gluons dynamically. This strong q_s versus $\sqrt{s}$ dependence was tracked down to the treatment of soft gluon emissions via the z_M parameter, underscoring the critical role of soft gluon treatment in the PB TMD method.

Interestingly, this investigation of the PB TMD method with a dynamical z_M and a smaller q_0 value of 0.5 GeV revealed no significant COM energy dependence for q_s, a result that contrasts with the stronger dependence observed in previous studies with larger q_0. Two possible conclusions can be drawn from this: either the correlation between q_0 and q_s is so strong that increasing q_0 from 0.5 GeV to 1.0 or 2.0 GeV drastically alters the q_s behaviour (which does not necessarily contradict previous results), or this finding for a dynamical resolution scale challenges prior results.

The first conclusion suggests that the observed COM energy dependence in q_s is sensitive to the initial q_0 setting and the resolution scale treatment. Which suggests that the result may act as an intermediary between the two resolution scale scenarios. If fixed z_M is viewed as a limiting

---

[1] The reader with an eye for detail might notice that the absolute values for the q_s parameter are quite different for different q_0. This behaviour is not yet understood. It is known to originate from the soft gluon treatment, because with increasing q_0 some soft emissions are cut away. Furthermore, q_0 and q_s are not independent parameters, but there is an interplay. Why does it manifest itself in $\sqrt{s}$ dependence? That's still a mystery. Some people link it with some saturation/black disc limit effects.

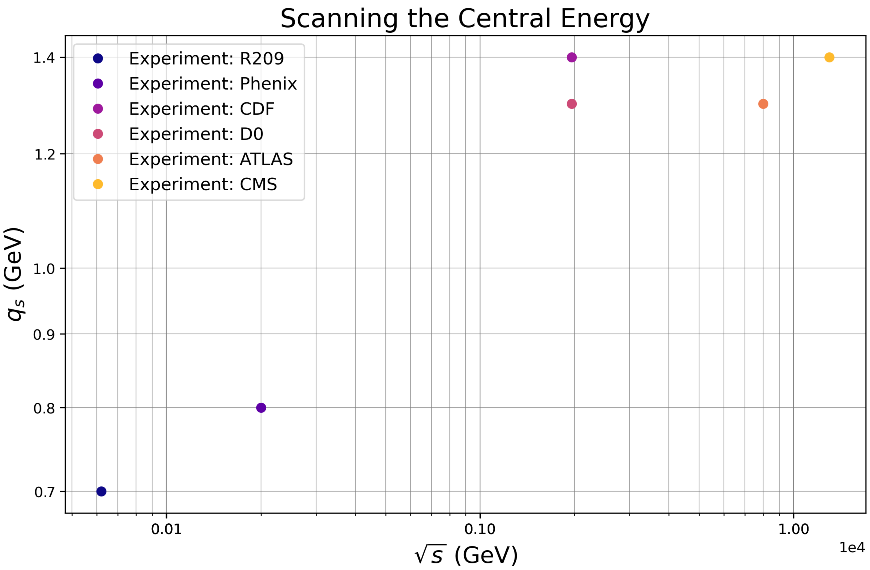

Figure 5.11: The preliminary results for $q_0 = 1.0$ GeV that showcase a COM energy dependence of the q_s parameter across a large COM spectrum. [59]

case of a dynamical z_M at very small q_0 values, smaller than Λ_{QCD}, then the approach effectively lowers q_0 from 1 or 2 GeV toward Λ_{QCD}. This suggests that it is possible to use a dynamical z_M while allowing sufficient soft emissions—similar to the fixed z_M case—and including enough of the infrared region, resulting in a flattening of q_s vs COM energy, rather than the rise observed when q_0 is fully within the perturbative region above 1 GeV.

The second conclusion remains also possible, particularly concerning the role of the strong running coupling. The interplay between α_s and the energy dependence requires deeper investigation. Notably, in previous PB TMD models, the coupling α_s is typically cut off at a scale of 1.0 GeV or higher. However, in the current study, the parameter $q_0 = 0.5$ GeV also serves as the cut-off scale for α_s.

The observed new behaviour in the study remains not fully understood. A potential avenue for further research would involve examining a model where the parameter z_M is also defined dynamically, with q_0 set to 0.5 GeV, but with an additional cut-off for α_s set at a higher value, such as 1.0 GeV. This would help determine whether the distribution of q_s versus $\sqrt{s}$ remains flat or if a slope emerges. In essence, this investigation could clarify whether the running coupling significantly impacts these results or if the observed COM energy dependence of q_s is primarily driven by the soft gluon resolution scale. If this alternative model were to exhibit different behaviour depending on the choice of q_0, it would indicate a non-negligible contribution from α_s to the q_s COM energy dependence, challenging previous assumptions that α_s had a minimal effect.

As mentioned at the end of Section 3.4, the current PB TMD calculations do not include any flavour dependence in the intrinsic transverse momentum (k_T) distribution. This choice was driven by the minimal sensitivity to flavour structure observed in precision DIS data, as discussed in Ref. [26]. However, recent studies using the CSS approach [5] have shown that

DY data and semi-inclusive DIS data can indeed provide sensitivity to flavour dependence, as highlighted in Refs. [60, 61]. Given these findings, it would be valuable to extend current PB TMD analyses of DY data to include flavour-dependent intrinsic-k_T distributions.

In addition, as noted in Section 5.4, the present analysis does not account for correlated systematic uncertainties. These uncertainties are available for certain data sets and have been shown to play a significant role in analyses based on the fixed resolution scale framework, as observed in Ref. [42]. Therefore, it would be beneficial to extend the current study to incorporate all available correlations, enhancing the robustness of the analysis.

Chapter 6

Conclusion

This thesis was driven by a deep fascination with elementary particle physics and the profound philosophical insights it offers into the nature of the universe. The research aimed to explore, for the first time, the behaviour of the q_s parameter in the intrinsic-k_T distribution (Eq. (3.4.8)) across various center-of-mass (COM) energies, employing the parton branching (PB) Transverse Momentum Dependent (TMD) methodology [11, 12] with a dynamical resolution scale (z_M) with $q_0 = 0.5$ GeV as introduced in Section 3.5. The PB TMD methodology stands out due to its comprehensive consideration of soft gluon radiations and transverse momentum recoils in parton branchings along the QCD cascade. This innovative approach effectively addresses the complexities associated with multiple energy scales in the inclusive DY transverse momentum distribution.

The PB TMD method was applied to experiments across a wide COM energy range (62 GeV – 13 TeV); using data from the experiments: CMS, ATLAS, CDF, D0, Phenix, and R209, demonstrating a consistent fit for most datasets, with a few exceptions due to systematic discrepancies (CDF) and limited data points (D0). The analysis revealed that the parameter q_s is independent, within uncertainty, of the COM energy. This presents a new behaviour in the energy dependence of q_s, that warrants further investigation. Notably, Ref. [42], using a fixed, non-dynamical z_M, found a nearly flat q_s behaviour with energy from fits to DY p_T data. In contrast, Ref. [55] reported a different trend, and Refs. [56, 57] observed a similar different trend in standard Monte Carlo generators. This thesis, however, reveals that when working with a dynamical z_M and a small transverse momentum scale of $q_0 = 0.5$ GeV, the behaviour of q_s with energy flattens, aligning more closely with the findings of Ref. [42] and mimicking nonperturbative Sudakov effects. The calculation in this thesis appears to be the first instance where a dynamical z_M approach, when compared with DY data, results in a nearly flat q_s, challenging earlier results reported in Ref. [55].

However, it is important to compare these findings with the fixed z_M calculation of Ref. [42], and closely examine the minimum transverse momentum scales used in this thesis versus those in previous dynamical z_M calculations. It was reported in Refs. [55–57] that the slope was decreasing with decreasing q_0. Which could suggest that the result of this study is the bridge between the two situations; the scenario with a fixed z_M can be seen as the limit of a dynamical z_M with q_0 very small—allowing significantly more soft emissions than calculations with q_0 values of 1 GeV or higher.

While the research has provided valuable insights, it is essential to acknowledge certain limitations. The primary limitation of this study is the incomplete and limited data from certain experiments. Specifically, the data points for the CDF and D0 experiments at 1960 GeV did not yield usable results. The limited number of data points and their systematic discrepancies impacted the robustness of the analysis. This underscores the need for more comprehensive and higher-quality datasets to validate the findings across all energy scales and experimental setups. Furthermore, this study does not take correlated uncertainties into account, which have shown to play a significant role in analyses with fixed resolution scale [42].

Building on the results of this thesis, several avenues for future research are recommended.

- The main question that is obtained from the result is the role of the strong running coupling $\alpha_s(\mu^2)$. Research into this can be done by varying the cut-off in α_s for $q_0 = 0.5$ GeV, and to see if the distribution of q_s vs $\sqrt{s}$ remains flat or if a slope appears. This would give insight in the contribution to the q_s COM energy dependence, whether it only comes from the soft gluon resolution scale or if it also comes from the treatment of the strong coupling.
- A potential research avenue could involve extending the current PB TMD analysis to incorporate flavour-dependent intrinsic-k_T distributions. While the existing calculations do not include this flavour dependence, recent studies [60, 61] have demonstrated that DY can be sensitive to flavour structure.
- Additionally, further investigations could focus on applying the PB TMD methodology to experimental data in the 1960 GeV region, to validate its applicability. Furthermore, the correlated uncertainties should be taken into account for the CMS experiment.

In conclusion, this thesis has significantly contributed to particle physics by enhancing the understanding of the dynamical resolution scale z_M. This was done by investigating the parameter q_s in the intrinsic-k_T distribution across varying COM energies using the PB TMD method with dynamical z_M. The application of the PB TMD methodology has demonstrated its robustness, providing a valuable tool for precise predictions in high-energy particle collisions. This research advances theoretical knowledge and paves the way for future studies to build upon these findings.

Acknowledgements

I would like to express my sincere gratitude to my supervisor, Prof. Dr. Francesco Hautmann, for his guidance and support throughout the research and writing of this thesis. The complexity of the topic made it challenging, and his assistance was essential in helping me gain a deeper understanding. I am also very thankful to Dr. Aleksandra Lelek for her significant help during the research phase. Her expertise was crucial in carrying out the simulations, which would have been out of reach for a master's student without her guidance. Additionally, her support during the writing process was greatly appreciated. Lastly, I extend my thanks to Thomas Van Laer for his thorough notes, which were extremely helpful in understanding the challenging theory of Quantum Chromodynamics.

A.1 Feynman Rules

The full QCD Lagrangian is

$$\begin{aligned}\mathcal{L}_{\text{QCD}} = {} & \sum_f \sum_{i,j} \sum_{\alpha,\beta} i\overline{\psi}_f^{i\alpha}(\gamma^\mu)_{\alpha\beta}\delta^{ij}\partial_\mu\psi_f^{j\beta} + \sum_f \sum_{i,j} \sum_{\alpha,\beta} g_s\overline{\psi}_f^{i\alpha}(\gamma^\mu)_{\alpha\beta}A^a_\mu T^a_{ij}\psi_f^{j\beta} \\ & - \frac{1}{2}\delta^{ab}\left(\partial_\mu A^b_\nu\partial^\mu A^{\nu a} - \partial_\nu A^b_\mu\partial^\mu A^{\nu a} + \frac{1}{\xi}\partial_\mu A^b_\mu\partial^\mu A^{\mu a}\right) - g_s\partial_\mu A^a_\nu f^{abc}A^{\mu b}A^{\nu c} \\ & - \frac{1}{4}g_s^2 f^{abc}f^{ade}A^b_\mu A^c_\nu A^{\mu d}A^{\nu e} - \bar{c}^a\partial^2 c^a + g_s f^{abc}(\partial_\mu\bar{c}^a)A^{\mu b}c^c - \sum_f m_f\overline{\psi}_f\psi_f. \end{aligned} \tag{A.1.1}$$

All QCD Feynman rules are summarised in Fig A.1 .

	Diagram	**Feynman Rule**
(1) Quark propagator	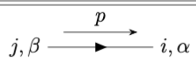	$\frac{i\delta^{ij}}{(\not{p}-m_f+i\varepsilon)_{\alpha\beta}}$
(2) Gluon propagator	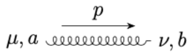	$\delta^{ab}\left(-g^{\mu\nu}+(1-\xi)\frac{p^\mu p^\nu}{p^2+i\varepsilon}\right)\frac{i}{p^2+i\varepsilon}$
(3) Ghost propagator	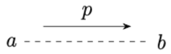	$\frac{i\delta^{ab}}{p^2+i\varepsilon}$
(4) Quark-gluon vertex	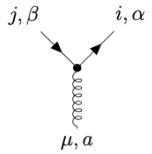	$-ig_s(\gamma^\mu)_{\alpha\beta}T^a_{ij}$
(5) Ghost-gluon vertex	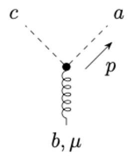	$g_s f^{abc}p^\mu$
(6) Cubic gluon vertex	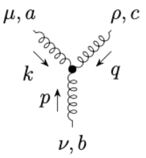	$-g_s f^{abc}g^{\mu\nu}(k-p)^\rho$ $-g_s f^{abc}g^{\nu\rho}(p-q)^\mu$ $-g_s f^{abc}g^{\rho\mu}(q-k)^\nu$
(7) Quartic gluon vertex	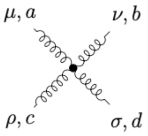	$-ig_s^2 f^{eac}f^{ebd}\left(g^{\mu\nu}g^{\rho\sigma}-g^{\mu\sigma}g^{\rho\nu}\right)$ $-ig_s^2 f^{ead}f^{ebc}\left(g^{\mu\nu}g^{\rho\sigma}-g^{\mu\rho}g^{\nu\sigma}\right)$ $-ig_s^2 f^{eab}f^{ecd}\left(g^{\mu\rho}g^{\nu\sigma}-g^{\mu\sigma}g^{\nu\rho}\right)$

Figure A.1: The QCD Feynman rules and the corresponding diagrams. The numbers in parentheses correspond to the term in the Lagrangian in (A.1.1). The (1)–(3) terms are kinetic terms.The interactions are displayed in (4)–(7). Quarks: full lines, gluons: curled lines, and ghosts: dashed lines. i and j are for the colours, a, b, c and d are for gluons, μ, ν, ρ, σ are Lorentz indices, and α and β are spinor polarisation indices.[62]

A.2 Splitting Functions

In this appendix, the nonzero, lowest order splitting functions are given in Fig. A.2, together with the vertex diagrams they represent. The indices i, j and k denote the flavour. When changing all quarks to antiquarks and vice versa, the splitting function remains the same. This is elucidated by writing those splitting functions on the same row.

Splitting Function	**Diagram**	**Equal Splitting Function**	**Diagram**
$P^{(0)}_{q_i q_j}(z)$	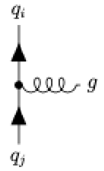	$P^{(0)}_{\bar{q}_i \bar{q}_j}(z)$	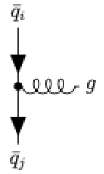
$P^{(0)}_{g q_j}(z)$	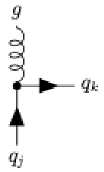	$P^{(0)}_{g \bar{q}_j}(z)$	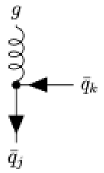
$P^{(0)}_{q_i g}(z)$	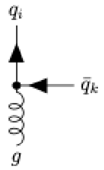	$P^{(0)}_{\bar{q}_i g}(z)$	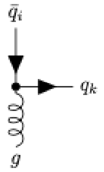
$P^{(0)}_{gg}(z)$	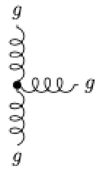		

Figure A.2: The lowest order splitting functions and their corresponding diagrams for the vertices they represent.[62]

A.3 The Two-Loop R-Coefficients

In this appendix, the two-loop coefficients of the perturbative expansion for the functions R_{ab} are given. As in Section 3.1, the coefficients can be read from the two-loop results in [21, 22]. Introducing the functions

$$p_{qq}(z) = \frac{2}{1-z} - 1 - z, \tag{A.3.1}$$

$$p_{qg}(z) = z^2 + (1-z)^2, \;\; p_{gq}(z) = \frac{1+(1-z)^2}{z}, \tag{A.3.2}$$

$$p_{gg}(z) = \frac{1}{1-z} + \frac{1}{z} - 2 + z(1-z), \tag{A.3.3}$$

$$S_2(z) = -2\mathrm{Li}_2(-z) + \frac{1}{2}\ln^2 z - 2\ln z \ln(1+z) - \frac{\pi^2}{6}, \tag{A.3.4}$$

where the dilogarithm function is defined by

$$\mathrm{Li}_2(y) = -\int_0^y \frac{dt}{t}\ln(1-t). \tag{A.3.5}$$

The two-loop contributions $R^{(1)}_{ab}$ for quark-gluon and gluon-gluon cases are given by

$$\begin{aligned}
R^{(1)}_{gq}(z) =& C_F^2\Bigg[-\frac{5}{2} - \frac{7}{2}z + \left(2 + \frac{7}{2}z\right)\ln z + \left(\frac{1}{2}z - 1\right)\ln^2 z - 2z\ln(1-z) \\
&-\Big(3\ln(1-z) + \ln^2(1-z)\Big)p_{gq}(z)\Bigg] + C_F C_A\Bigg[\frac{28}{9} + \frac{65}{18}z + \frac{44}{9}z^2 \\
&+\left(-12 - 5z - \frac{8}{3}z^2\right)\ln z + (4+z)\ln^2 z + 2z\ln(1-z) \\
&+p_{gq}(z)\left(-2\ln z\ln(1-z) + \frac{1}{2}\ln^2 z + \frac{11}{3}\ln(1-z) + \ln^2(1-z) - \frac{\pi^2}{6} + \frac{1}{2}\right) \\
&+p_{gq}(-z)S_2(z)\Bigg] + C_F T_R N_f\left[-\frac{4}{3}z - \left(\frac{20}{9} + \frac{4}{3}\ln(1-z)\right)p_{gq}(z)\right],
\end{aligned} \tag{A.3.6}$$

$$\begin{aligned}
R^{(1)}_{qg}(z) = \frac{1}{2}C_F T_R\Bigg[&4 - 9z + (-1+4z)\ln z + (-1+2z)\ln^2 z + 4\ln(1-z) \\
&+\Big(-4\ln z\ln(1-z) + 4\ln z + 2\ln^2 z - 4\ln(1-z) + 2\ln^2(1-z) \\
&-\frac{2}{3}\pi^2 + 10\Big)p_{qg}(z)\Bigg] + \frac{1}{2}C_A T_R\left[\frac{182}{9} + \frac{14}{9}z + \frac{40}{9}z^2 + \left(\frac{136}{3}z - \frac{38}{3}\right)\ln z\right. \\
&- 4\ln(1-z) - (2+8z)\ln^2 z + \Bigg(-\ln^2 z + \frac{44}{3}\ln z - 2\ln^2(1-z) \\
&\left.+4\ln(1-z) + \frac{\pi^2}{3} - \frac{218}{9}\Bigg)p_{qg}(z) + 2p_{qg}(-z)S_2(z)\right].
\end{aligned} \tag{A.3.7}$$

And

$$\begin{aligned} R_{gg}^{(1)}(z) = {} & C_F T_R N_f \Big[-16 + 8z + \frac{20}{3}z^2 + \frac{4}{3z} + (-6-10z)\ln z + (-2-2z)\ln^2 z \Big] \\ & + C_A T_R N_f \Big[2 - 2z + \frac{26}{9}z^2 - \frac{26}{9z} - \frac{4}{3}(1+z)\ln z - \frac{20}{9}\Big(\frac{1}{z} - 2 + z - z^2\Big) \Big] \\ & + C_A^2 \Big[\frac{27}{2}(1-z) + \frac{67}{9}\Big(z^2 - \frac{1}{z}\Big) + \Big(-\frac{25}{3} + \frac{11}{3}z - \frac{44}{3}z^2\Big)\ln z \\ & + 4(1+z)\ln^2 z + 2p_{gg}(-z)S_2(z) + \big(-4\ln z \ln(1-z) + \ln^2 z\big)\, p_{gg}(z) \\ & + \Big(\frac{67}{9} - \frac{\pi^2}{3}\Big)\Big(\frac{1}{z} - 2 + z - z^2\Big) \Big]. \end{aligned} \tag{A.3.8}$$

The two-loop contributions $R_{ab}^{(1)}$ for the non-singlet case, given the definitions in Eq. (3.1.9), are given by

$$R_{q\bar{q}}^{NS(1)}(z) = C_F\Big(C_F - \frac{C_A}{2}\Big)\Big[2p_{qq}(-z)S_2(z) + 2(1+z)\ln z + 4(1-z)\Big], \tag{A.3.9}$$

$$\begin{aligned} R_{qq}^{NS(1)}(z) = {} & C_F^2 \Big[-\Big(2\ln z \ln(1-z) + \frac{3}{2}\ln z\Big) p_{qq}(z) - \Big(\frac{3}{2} + \frac{7}{2}z\Big)\ln z \\ & - \frac{1}{2}(1+z)\ln^2 z - 5(1-z)\Big] + C_F C_A \Big[\Big(\frac{1}{2}\ln^2 z + \frac{11}{6}\ln z\Big) p_{qq}(z) \\ & - (1+z)\Big(\frac{67}{18} - \frac{\pi^2}{6}\Big) + (1+z)\ln z + \frac{20}{3}(1-z)\Big] \\ & + C_F T_R N_f \Big[-\frac{2}{3}\ln z p_{qq}(z) + \frac{10}{9}(1+z) - \frac{4}{3}(1-z)\Big]. \end{aligned} \tag{A.3.10}$$

The evolution of the singlet quark distribution coupled to gluons is controlled by the linear combination of the splitting functions in Eq. (3.1.9), which is defined as:

$$P_{qq} = P_{qq}^{NS} + P_{q\bar{q}}^{NS} + N_f(P_{qq}^{S} + P_{q\bar{q}}^{S}). \tag{A.3.11}$$

The corresponding two-loop contribution to R_{ab} in Eq. (3.1.7) is given by

$$\begin{aligned} R_{qq}^{(1)}(z) = {} & C_F^2 \Big[-1 + z + \Big(\frac{1}{2} - \frac{3}{2}z\Big)\ln z - \frac{1}{2}(1+z)\ln^2 z + 2p_{qq}(-z)S_2(z) \\ & - \Big(\frac{3}{2}\ln z + 2\ln z \ln(1-z)\Big) p_{qq}(z)\Big] \\ & + C_F C_A \Big[\frac{14}{3}(1-z) - p_{qq}(-z)S_2(z) + \Big(\frac{11}{6}\ln z + \frac{1}{2}\ln^2 z\Big) p_{qq}(z) \qquad \text{(A.3.12)} \\ & - (z+1)\Big(\frac{67}{18} - \frac{\pi^2}{6}\Big)\Big] + C_F T_R N_f \Big[-\frac{16}{3} + \frac{40}{3}z + \Big(10z + \frac{16}{3}z^2 + 2\Big)\ln z \qquad \text{(A.3.13)} \\ & - \frac{112}{9}z^2 + \frac{40}{9z} - 2(1+z)\ln^2 z - \frac{2}{3}\ln z p_{qq}(z) + \frac{10}{9}(z+1)\Big]. \qquad \text{(A.3.14)} \end{aligned}$$

A.4 CMS Calculations

In this appendix, the calculations for CMS (for $q_s \in [0.1, 1.5]$ GeV) are shown in Figs. A.3 and A.4. The calculations are done with the PB TMD method using a dynamical resolution scale with $q_0 = 0.5$ GeV.

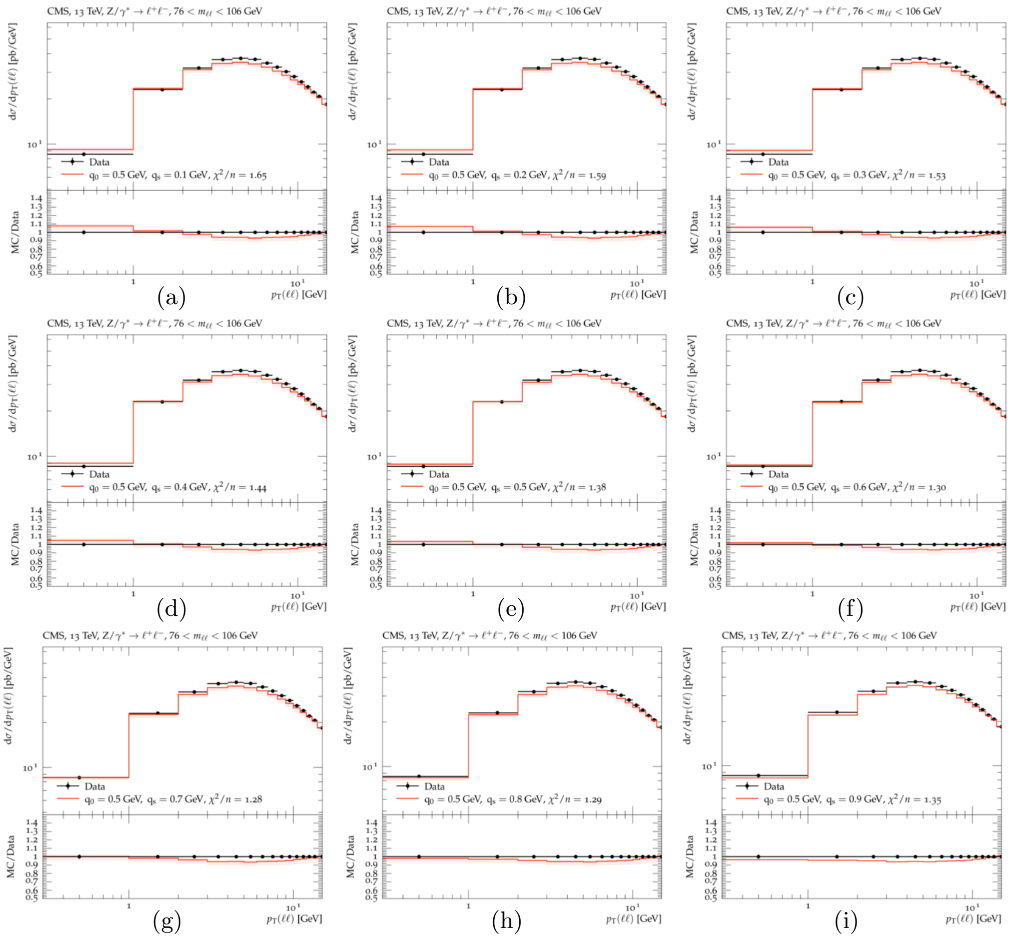

(a) (b) (c)

(d) (e) (f)

(g) (h) (i)

Figure A.3: Calculation of DY p_T spectrum of CMS data: (a) $q_s = 0.1$ GeV, (b) $q_s = 0.2$ GeV, (c) $q_s = 0.3$ GeV, (d) $q_s = 0.4$ GeV (e) $q_s = 0.5$ GeV, (f) $q_s = 0.6$ GeV, (g) $q_s = 0.7$ GeV, (h) $q_s = 0.8$ GeV (i) $q_s = 0.9$ GeV.

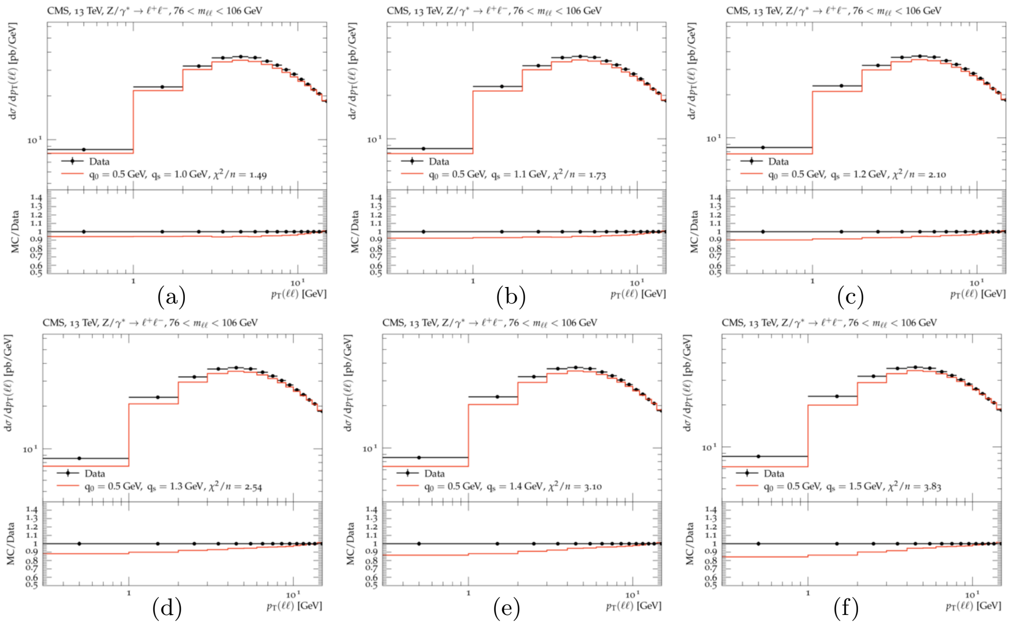

(a) (b) (c)

(d) (e) (f)

Figure A.4: Calculation of DY p_T spectrum of CMS data: (a) $q_s = 1.0$ GeV, (b) $q_s = 1.1$ GeV, (c) $q_s = 1.2$ GeV, (d) $q_s = 1.3$ GeV (e) $q_s = 1.4$ GeV, (f) $q_s = 1.5$ GeV.

A.5 ATLAS Calculations

In this appendix, the calculations for ATLAS (for $q_s \in [0.1, 1.5]$ GeV) are shown in Figs. A.5 and A.6. The calculations are done with the PB TMD method using a dynamical resolution scale with $q_0 = 0.5$ GeV.

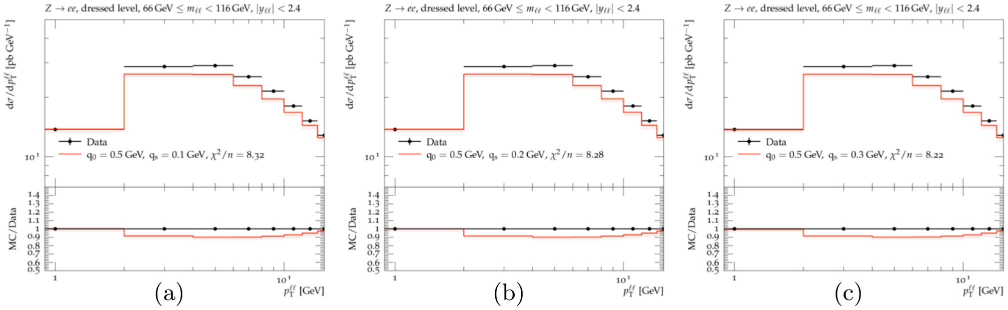

(a) (b) (c)

Figure A.5: Calculation of DY p_T spectrum of ATLAS data: (a) $q_s = 0.1$ GeV, (b) $q_s = 0.2$ GeV, (c) $q_s = 0.3$ GeV.

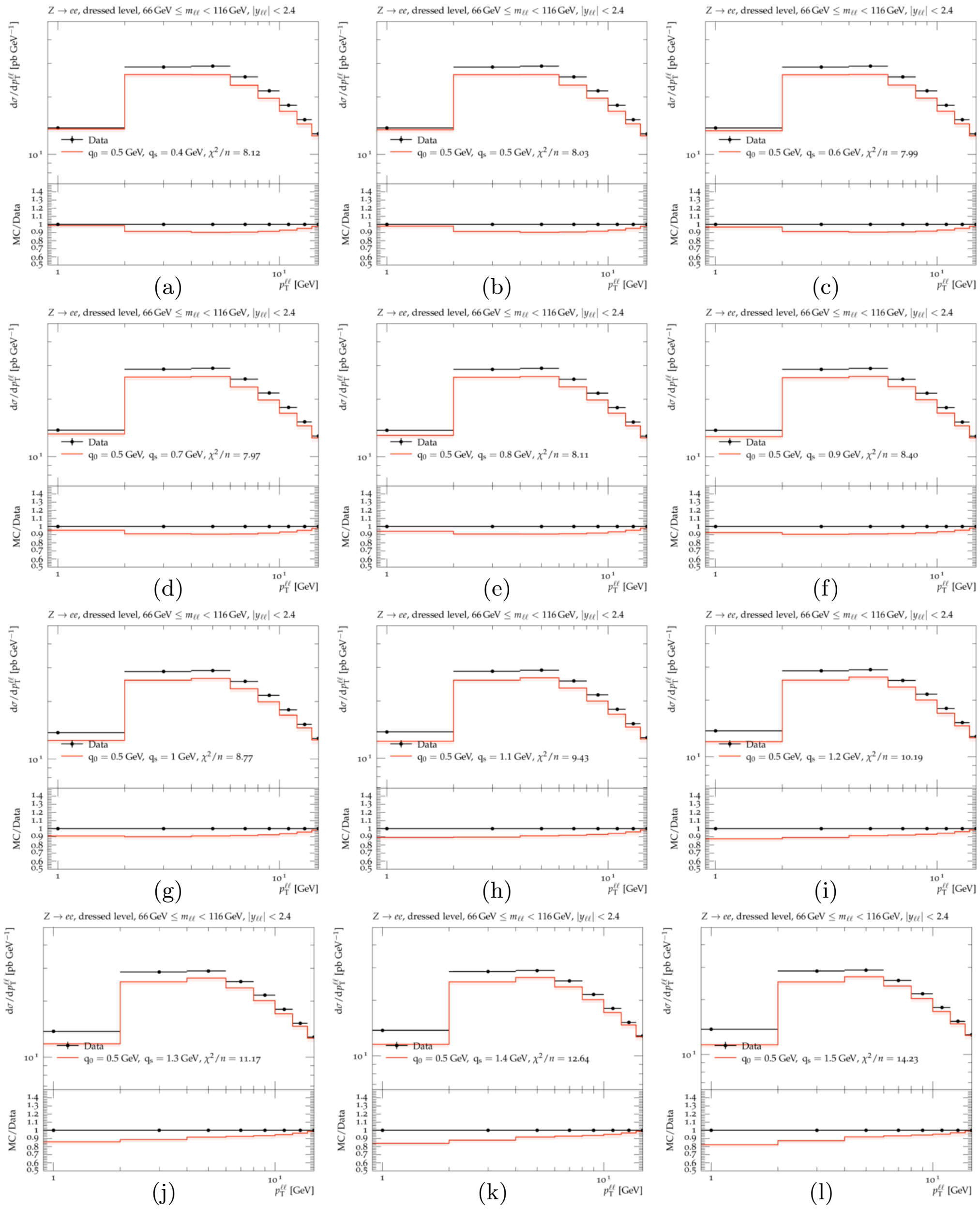

(a) (b) (c) (d) (e) (f) (g) (h) (i) (j) (k) (l)

Figure A.6: Calculation of DY p_T spectrum of ATLAS data: (a) $q_s = 0.4$ GeV, (b) $q_s = 0.5$ GeV, (c) $q_s = 0.6$ GeV, (d) $q_s = 0.7$ GeV (e) $q_s = 0.8$ GeV, (f) $q_s = 0.9$ GeV, (g) $q_s = 1.0$ GeV, (h) $q_s = 1.1$ GeV, (i) $q_s = 1.3$ GeV (j) $q_s = 1.4$ GeV, (k) $q_s = 1.5$ GeV.

A.6 CDF Calculations

Listing CDF calculations of the differential cross sections for TMDs with $q_s = [0.1, 1.5]$ GeV. These can be seen in Figures A.7 and A.8. They are provided to showcase the unsatisfactory description the PB TMD method provides for the CDF data at COM energy $\sqrt{s} = 1.96$ TeV. It can be clearly seen on all plots that the predictions do not effectively match the CDF data, resulting in the conclusion that this part of the research cannot be used.

Further research is recommended to analyse another CDF run at a different energy, to see if this data is accurately described with the PB TMD method using the dynamical resolution scale.

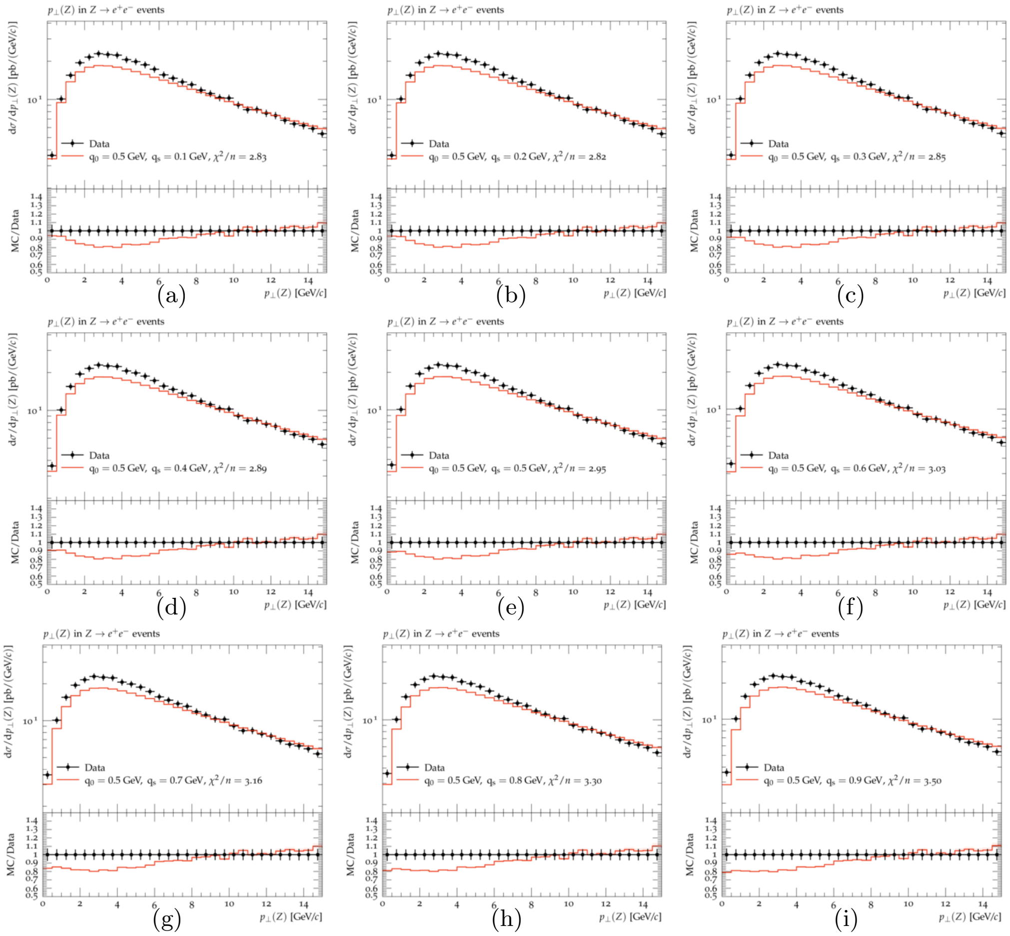

Figure A.7: Calculation of DY p_T spectrum of CDF data: (a) $q_s = 0.1$ GeV, (b) $q_s = 0.2$ GeV, (c) $q_s = 0.3$ GeV, (d) $q_s = 0.4$ GeV (e) $q_s = 0.5$ GeV, (f) $q_s = 0.6$ GeV, (g) $q_s = 0.7$ GeV, (h) $q_s = 0.8$ GeV (i) $q_s = 0.9$ GeV.

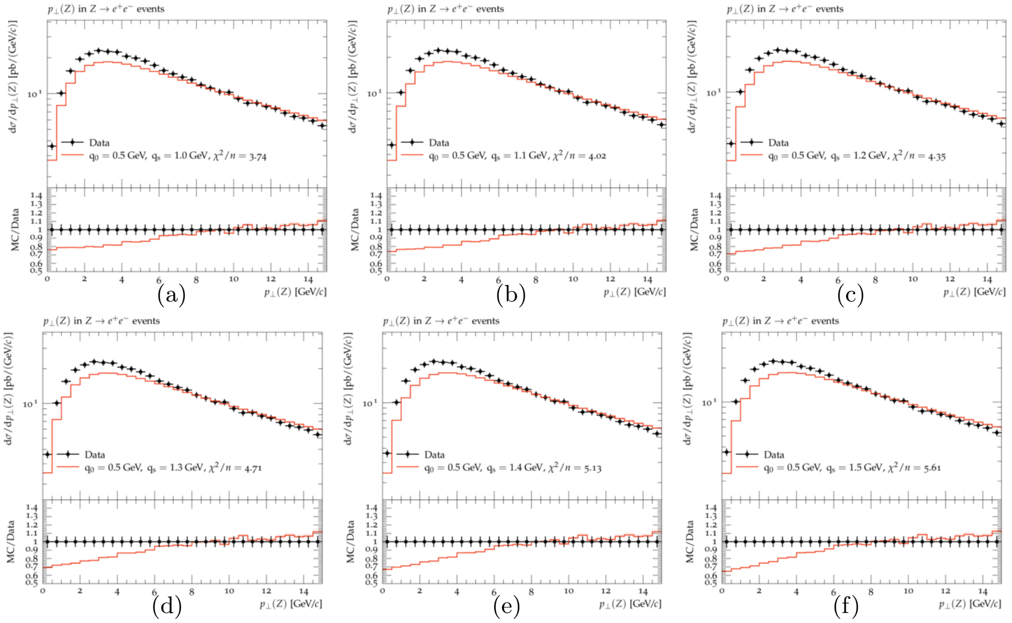

(a) (b) (c)

(d) (e) (f)

Figure A.8: Calculation of DY p_T spectrum of CDF data: (a) $q_s = 1.0$ GeV, (b) $q_s = 1.1$ GeV, (c) $q_s = 1.2$ GeV, (d) $q_s = 1.3$ GeV (e) $q_s = 1.4$ GeV, (f) $q_s = 1.5$ GeV.

A.7 D0 Calculations

In this appendix, the calculations for D0 (for $q_s \in [0.1, 1.5]$ GeV) are shown in Figs. A.9 and A.10. The calculations are done with the PB TMD method using a dynamical resolution scale with $q_0 = 0.5$ GeV.

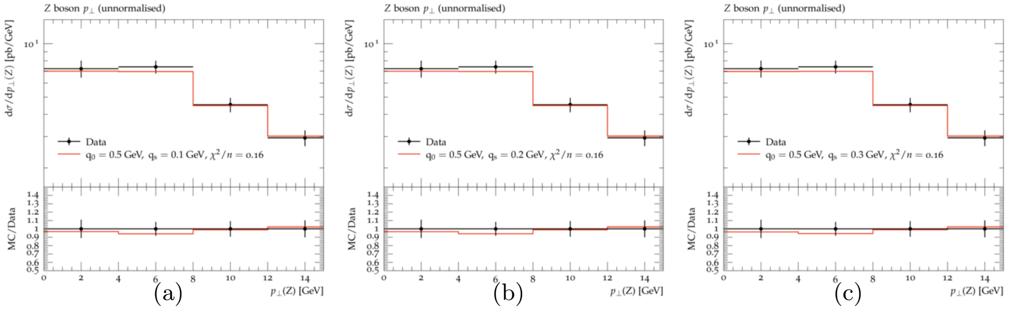

(a) (b) (c)

Figure A.9: Calculation of DY p_T spectrum of D0 data: (a) $q_s = 0.1$ GeV, (b) $q_s = 0.2$ GeV, (c) $q_s = 0.3$ GeV.

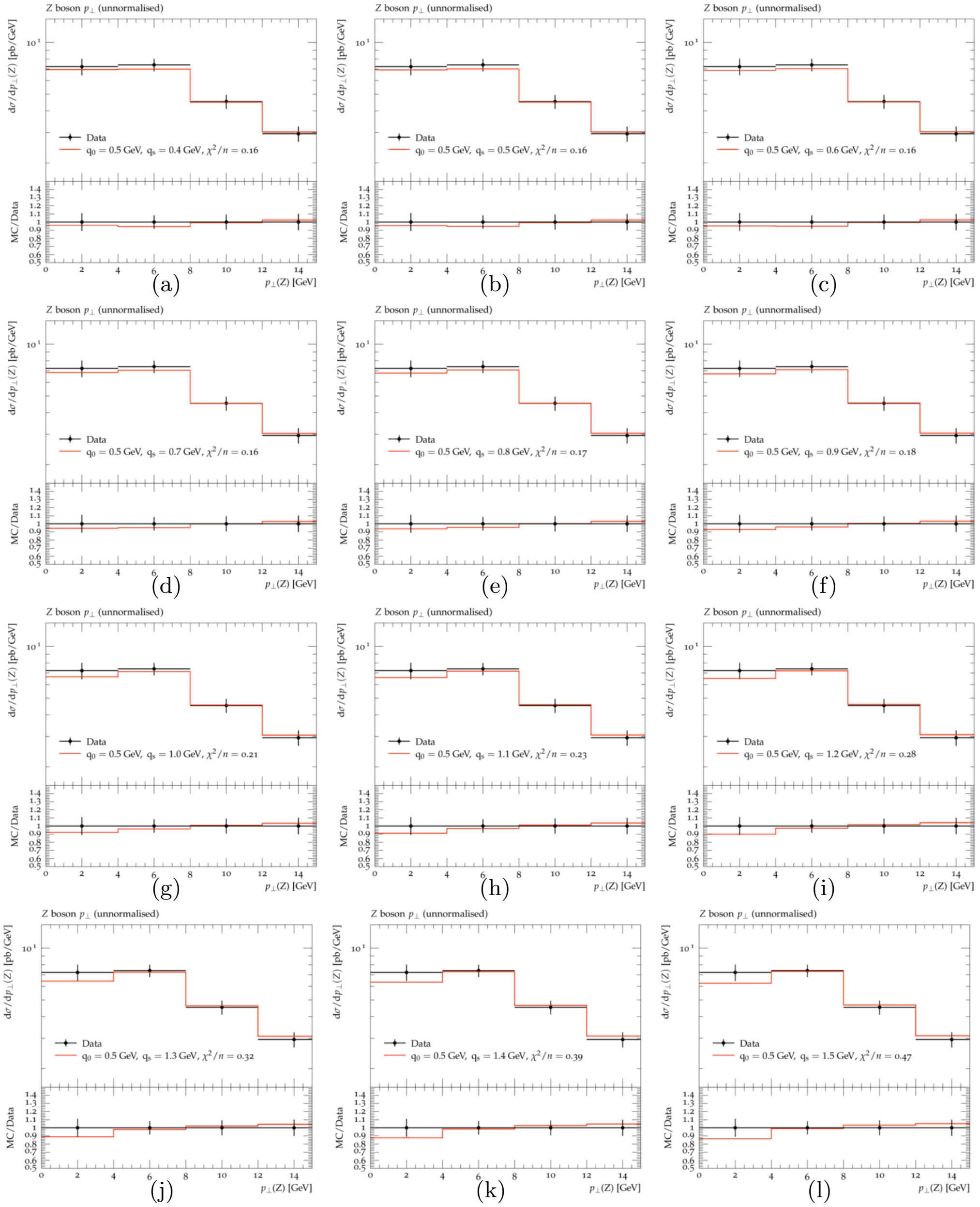

(a) (b) (c) (d) (e) (f) (g) (h) (i) (j) (k) (l)

Figure A.10: Calculation of DY p_T spectrum of D0 data: (a) $q_s = 0.4$ GeV, (b) $q_s = 0.5$ GeV, (c) $q_s = 0.6$ GeV, (d) $q_s = 0.7$ GeV (e) $q_s = 0.8$ GeV, (f) $q_s = 0.9$ GeV, (g) $q_s = 1.0$ GeV, (h) $q_s = 1.1$ GeV, (i) $q_s = 1.3$ GeV (j) $q_s = 1.4$ GeV, (k) $q_s = 1.5$ GeV.

A.8 Phenix Calculations

In this appendix, the calculations for Phenix (for $q_s \in [0.1, 1.5]$ GeV) are shown in Figs. A.11 and A.12. The calculations are done with the PB TMD method using a dynamical resolution scale with $q_0 = 0.5$ GeV.

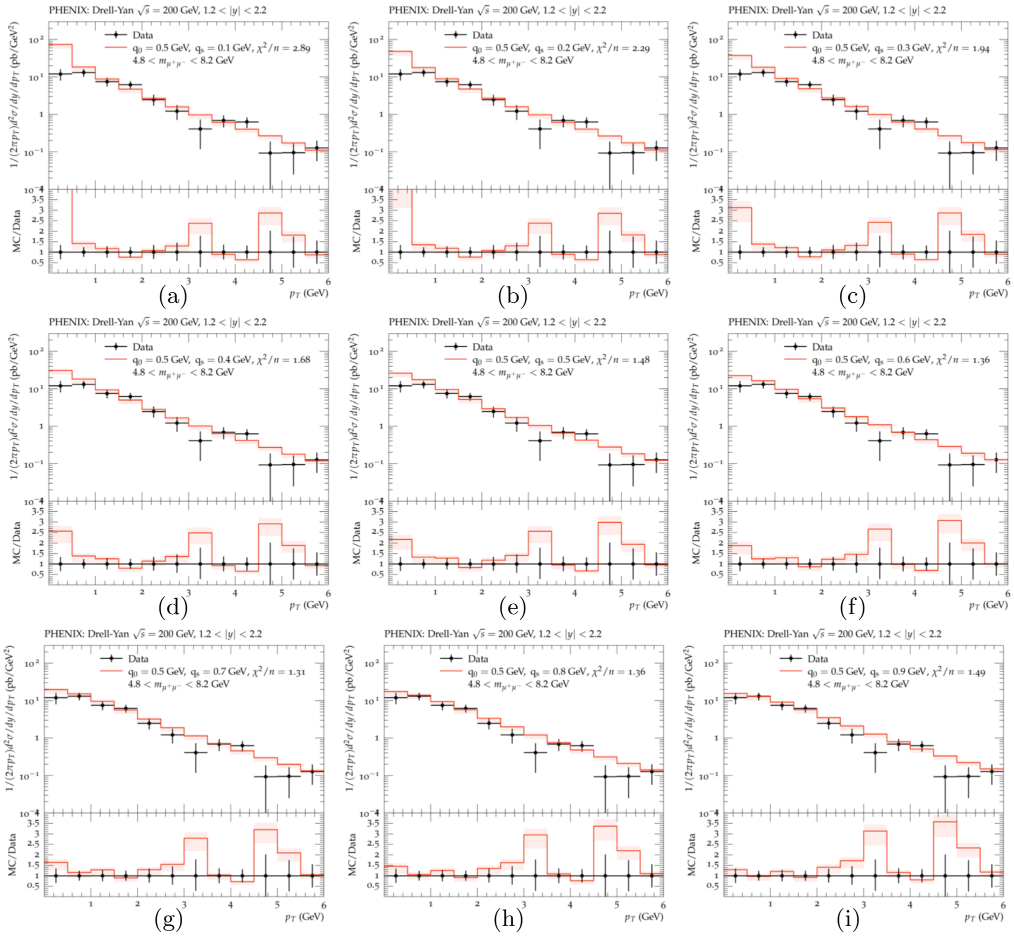

(a) (b) (c)

(d) (e) (f)

(g) (h) (i)

Figure A.11: Calculation of DY p_T spectrum of Phenix data: (a) $q_s = 0.1$ GeV, (b) $q_s = 0.2$ GeV, (c) $q_s = 0.3$ GeV, (d) $q_s = 0.4$ GeV (e) $q_s = 0.5$ GeV, (f) $q_s = 0.6$ GeV, (g) $q_s = 0.7$ GeV, (h) $q_s = 0.8$ GeV (i) $q_s = 0.9$ GeV.

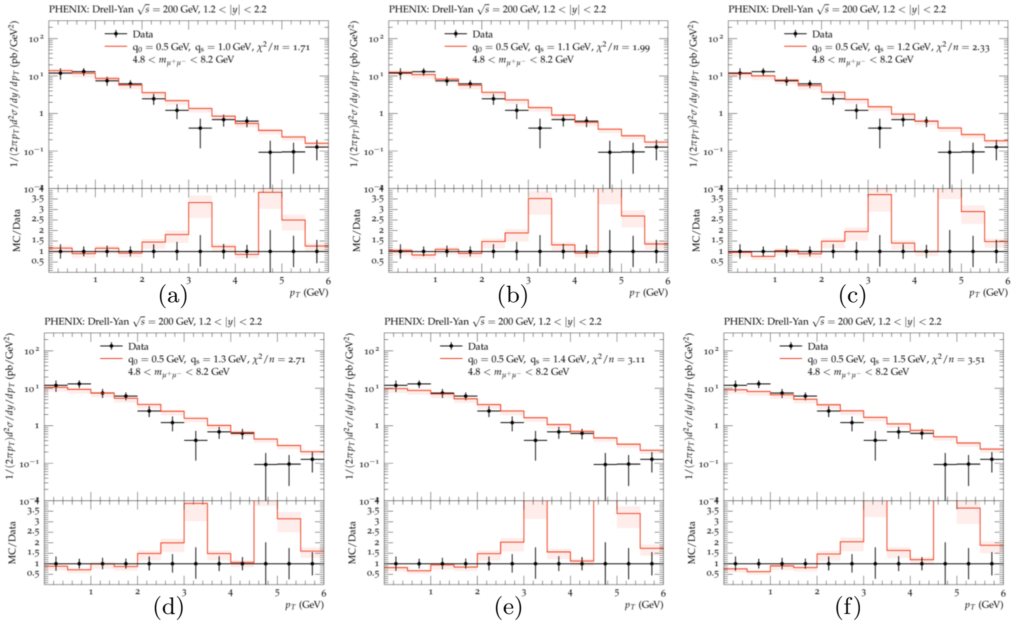

(a) (b) (c)

(d) (e) (f)

Figure A.12: Calculation of DY p_T spectrum of Phenix data: (a) $q_s = 1.0$ GeV, (b) $q_s = 1.1$ GeV, (c) $q_s = 1.2$ GeV, (d) $q_s = 1.3$ GeV (e) $q_s = 1.4$ GeV, (f) $q_s = 1.5$ GeV.

A.9 R209 Calculations

In this appendix, the calculations for R209 (for $q_s \in [0.1, 1.5]$ GeV) are shown in Figs. A.13 and A.14. The calculations are done with the PB TMD method using a dynamical resolution scale with $q_0 = 0.5$ GeV.

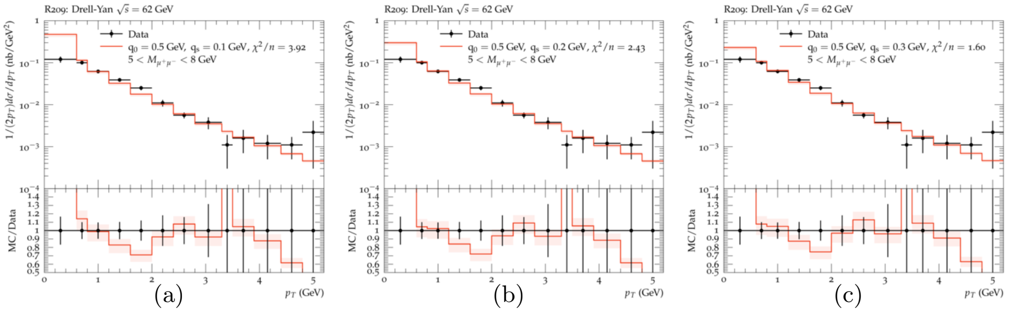

(a) (b) (c)

Figure A.13: Calculation of DY p_T spectrum of R209 data: (a) $q_s = 0.1$ GeV, (b) $q_s = 0.2$ GeV, (c) $q_s = 0.3$ GeV.

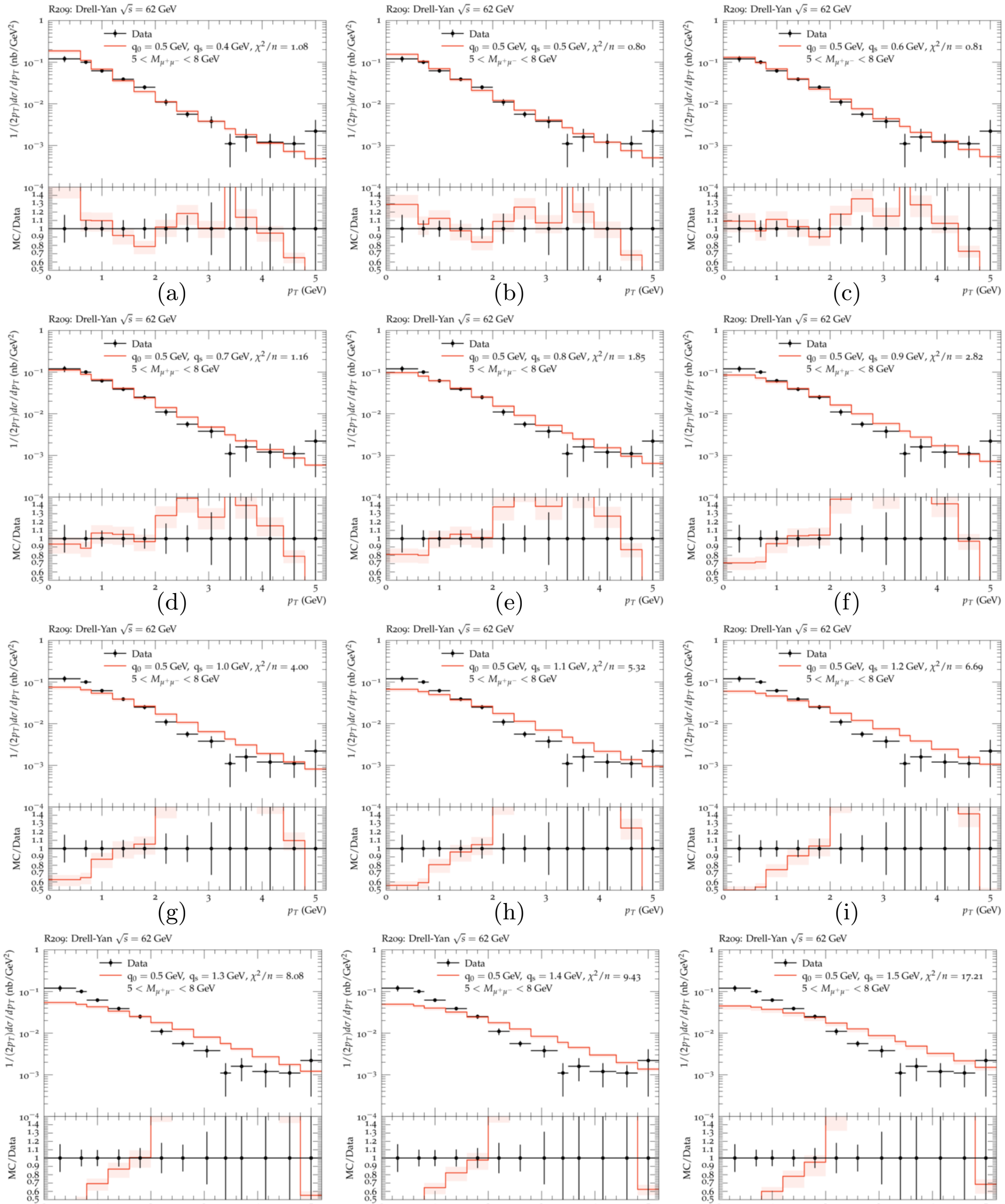

(a) (b) (c) (d) (e) (f) (g) (h) (i) (j) (k) (l)

Figure A.14: Calculation of DY p_T spectrum of R209 data: (a) $q_s = 0.4$ GeV, (b) $q_s = 0.5$ GeV, (c) $q_s = 0.6$ GeV, (d) $q_s = 0.7$ GeV (e) $q_s = 0.8$ GeV, (f) $q_s = 0.9$ GeV, (g) $q_s = 1.0$ GeV, (h) $q_s = 1.1$ GeV, (i) $q_s = 1.3$ GeV (j) $q_s = 1.4$ GeV, (k) $q_s = 1.5$ GeV.

Bibliography

[1]T. V. Laer, *Notes on quantum chromodynamics, a course taught by francesco hautmann*, Presented at the Quantum Chromodynamics course, Univ. of Antwerp, Belgium, Mar. 2023.

[2]S. D. Drell and T.-M. Yan, "Massive Lepton Pair Production in Hadron-Hadron Collisions at High-Energies", Phys. Rev. Lett. **25**, [Erratum: Phys.Rev.Lett. 25, 902 (1970)], 316–320 (1970).

[3]CMS Collaboration, "Measurements of differential Z boson production cross sections in proton-proton collisions at $\sqrt{s} = 13$ TeV", Journal of High Energy Physics **2019**, 61 (2019).

[4]Y. L. Dokshitzer, D. Diakonov, and S. I. Troian, "On the Transverse Momentum Distribution of Massive Lepton Pairs", Phys. Lett. B **79**, 269–272 (1978).

[5]J. C. Collins, D. E. Soper, and G. F. Sterman, "Transverse Momentum Distribution in Drell-Yan Pair and W and Z Boson Production", Nucl. Phys. B **250**, 199–224 (1985).

[6]T. Sjöstrand and others., "An introduction to PYTHIA 8.2", Computer Physics Communications **191**, 159–177 (2015).

[7]J. Bellm et al., "Herwig 7.0/Herwig++ 3.0 release note", European Physical Journal C **76**, 196 (2016).

[8]S. Frixione, P. Nason, and B. R. Webber, "Matching NLO QCD and parton showers in heavy flavour production", Journal of High Energy Physics **2003**, 007 (2003).

[9]S. Frixione and B. R. Webber, "Matching NLO QCD computations and parton shower simulations", Journal of High Energy Physics **2002**, 029 (2002).

[10]S. Frixione, P. Nason, and C. Oleari, "Matching NLO QCD computations with parton shower simulations: the POWHEG method", Journal of High Energy Physics **2007**, 070 (2007).

[11]F. Hautmann et al., "Collinear and tmd quark and gluon densities from parton branching solution of qcd evolution equations", JHEP **01**, 070 (2018).

[12]F. Hautmann and others., "Soft-gluon resolution scale in QCD evolution equations", Phys. Lett. B **772**, 446–451 (2017).

[13]A. Bermudez Martinez and others., "Production of Z bosons in the parton branching method", Physical Review D **100**, 074027 (2019).

[14]A. Bermudez Martinez et al., "The transverse momentum spectrum of low mass Drell-Yan production at next-to-leading order in the parton branching method", arXiv e-prints, arXiv:2001.06488 (2020).

[15]R. Angeles-Martinez and others., "Transverse Momentum Dependent (TMD) Parton Distribution Functions: Status and Prospects", Acta Physica Polonica B **46**, 2501 (2015).

[16] H. Fritzsch, *The history of qcd*, `https://cerncourier.com/a/the-history-of-qcd/`, 2020.

[17] M. E. Peskin and D. V. Schroeder, *An introduction to quantum field theory* (Addison-Wesley, 1995).

[18] V. N. Gribov and L. N. Lipatov, "Deep inelastic ep scattering in perturbation theory", Sov. J. Nucl. Phys. **15**, IPTI-381-71, 438–450 (1972).

[19] G. Altarelli and G. Parisi, "Asymptotic freedom in parton language", Nucl. Phys. B **126**, 298–318 (1977).

[20] Y. L. Dokshitzer, "Calculation of the structure functions for deep inelastic scattering and e+e- annihilation by perturbation theory in quantum chromodynamics", Sov. Phys. JETP **46**, Also in Zh. Eksp. Teor. Fiz. **73**, (1977), 1216, 641–653 (1977).

[21] G. Curci, W. Furmanski, and R. Petronzio, "Evolution of parton densities beyond leading order: the nonsinglet case", Nucl. Phys. B **175**, 27–92 (1980).

[22] W. Furmanski and R. Petronzio, "Lepton - Hadron Processes Beyond Leading Order in Quantum Chromodynamics", Z. Phys. C **11**, 293 (1982).

[23] R. K. Ellis, W. J. Stirling, and B. R. Webber, *Qcd and collider physics*, Vol. 8 (Cambridge University Press, 1996), pp. 1–435.

[24] F. Hautmann, L. Keersmaekers, A. Lelek, and A. M. Van Kampen, "Dynamical resolution scale in transverse momentum distributions at the LHC", Nucl. Phys. B **949**, 114795 (2019).

[25] B. R. Webber, "Monte Carlo Simulation of Hard Hadronic Processes", Ann. Rev. Nucl. Part. Sci. **36**, 253–286 (1986).

[26] A. Bermudez Martinez et al., "Collinear and TMD parton densities from fits to precision DIS measurements in the parton branching method", arXiv e-prints, arXiv:1804.11152 (2018).

[27] F. Hautmann, "Endpoint singularities in unintegrated parton distributions", Phys. Lett. B **655**, 26–31 (2007).

[28] J. Alwall et al., "The automated computation of tree-level and next-to-leading order differential cross sections, and their matching to parton shower simulations", Journal of High Energy Physics **2014**, 79 (2014).

[29] S. Baranov et al., "CASCADE3 A Monte Carlo event generator based on TMDs", European Physical Journal C **81**, 425 (2021).

[30] H. Jung et al., "The CCFM Monte Carlo generator CASCADE Version 2.2.03", European Physical Journal C **70**, 1237–1249 (2010).

[31] The xFitter Developers' Team., "xFitter: An Open Source QCD Analysis Framework. A resource and reference document for the Snowmass study", arXiv e-prints, arXiv:2206.12465 (2022).

[32] S. Alekhin et al., "HERAFitter. Open source QCD fit project", European Physical Journal C **75**, 304 (2015).

[33] H1 and ZEUS Collaborations, "Combination of Measurements of Inclusive Deep Inelastic $e^{\pm}p$ Scattering Cross Sections and QCD Analysis of HERA Data", arXiv e-prints, arXiv:1506.06042 (2015).

[34] S. Catani, B. R. Webber, and G. Marchesini, "QCD coherent branching and semiinclusive processes at large x", Nucl. Phys. B **349**, 635–654 (1991).

[35] F. Hautmann et al., "TMDlib and TMDplotter: library and plotting tools for transverse-momentum-dependent parton distributions", European Physical Journal C **74**, 3220 (2014).

[36] N. A. Abdulov et al., "TMDlib2 and TMDplotter: a platform for 3D hadron structure studies", European Physical Journal C **81**, 752 (2021).

[37] M. I. Abdulhamid et al., "Azimuthal correlations of high transverse momentum jets at next-to-leading order in the parton branching method", European Physical Journal C **82**, 36 (2022).

[38] A. Bermudez Martinez and F. Hautmann, "Azimuthal di-jet correlations with parton branching TMD distributions", arXiv e-prints, arXiv:2208.08446 (2022).

[39] CMS Collaboration, "Azimuthal separation in nearly back-to-back jet topologies in inclusive 2- and 3-jet events in pp collisions at $\sqrt{s} = 13$ TeV", arXiv e-prints, arXiv:1902.04374 (2019).

[40] S. Sadeghi Barzani, "Phd thesis", PhD thesis (UAntwerpen & SBU, 2024).

[41] S. Sadeghi Barzani, "PB TMD fits at NLO with dynamical resolution scale", arXiv e-prints, arXiv:2207.13519 (2022).

[42] I. Bubanja et al., "The small k$_T$-region in Drell-Yan production at next-to-leading order with the parton branching method", European Physical Journal C **84**, 154 (2024).

[43] A. M. van Kampen, "Drell-Yan transverse spectra at the LHC: a comparison of parton branching and analytical resummation approaches", SciPost Phys. Proc. **8**, 151 (2022).

[44] H. Yang and others., "Back-to-back azimuthal correlations in Z + jet events at high transverse momentum in the TMD parton branching method at next-to-leading order", European Physical Journal C **82**, 755 (2022).

[45] J. Alwall et al., "A standard format for Les Houches Event Files", Computer Physics Communications **176**, 300–304 (2007).

[46] A. Buckley et al., "Rivet user manual", Computer Physics Communications **184**, 2803–2819 (2013).

[47] A. Bermudez Martinez, F. Hautmann, and M. L. Mangano, "TMD evolution and multi-jet merging", Physics Letters B **822**, 136700 (2021).

[48] A. Bermudez Martinez, F. Hautmann, and M. L. Mangano, "Multi-jet physics at high-energy colliders and TMD parton evolution", arXiv e-prints, arXiv:2109.08173 (2021).

[49] A. Bermudez Martinez, F. Hautmann, and M. L. Mangano, "Multi-jet merging with TMD parton branching", Journal of High Energy Physics **2022**, 60 (2022).

[50] A. Bacchetta et al., "Difficulties in the description of drell-yan processes at moderate invariant mass and high transverse momentum", Phys. Rev. D **100**, 014018 (2019).

[51] S. Frixione and B. R. Webber, "Correcting for cutoff dependence in backward evolution of QCD parton showers", Journal of High Energy Physics **2024**, 150 (2024).

[52] M. Mendizabal, F. Guzman, H. Jung, and S. Taheri Monfared, "On the role of soft gluons in collinear parton densities and parton shower event generators", Unpublished (2023).

[53] S. Dooling, P. Gunnellini, F. Hautmann, and H. Jung, "Longitudinal momentum shifts, showering, and nonperturbative corrections in matched next-to-leading-order shower event generators", Physical Review D **87**, 094009 (2013).

[54] F. Hautmann and H. Jung, "Collinearity approximations and kinematic shifts in partonic shower algorithms", European Physical Journal C **72**, 2254 (2012).

[55] I. Bubanja et al., “Center-of-mass energy dependence of intrinsic-k_T distributions obtained from Drell-Yan production”, arXiv e-prints, arXiv:2404.04088 (2024).

[56] T. Sjöstrand and P. Skands, “Multiple Interactions and the Structure of Beam Remnants”, Journal of High Energy Physics **2004**, 053 (2004).

[57] S. Gieseke, M. H. Seymour, and A. Siódmok, “A model of non-perturbative gluon emission in an initial state parton shower”, Journal of High Energy Physics **2008**, 001 (2008).

[58] F. Hautmann, I. Scimemi, and A. Vladimirov, “Non-perturbative contributions to vector-boson transverse momentum spectra in hadronic collisions”, Physics Letters B **806**, 135478 (2020).

[59] A. Lelek et al., *To be published*, 2024.

[60] M. Bury, F. Hautmann, S. Leal-Gomez, I. Scimemi, A. Vladimirov, and P. Zurita, “PDF bias and flavor dependence in TMD distributions”, JHEP **10**, 118 (2022).

[61] A. Bacchetta et al., “Flavor dependence of unpolarized quark Transverse Momentum Distributions from a global fit”, (2024).

[62] T. V. Laer, “Multi-jet physics in high-energy hadron collisions”, Available: `https://anet.be/record/opacuantwerpen/c:lvd:15392306/N`, MA thesis (Univ. of Antwerp, Antwerp, Belgium, 2023).